

# Motor Control For Human Jumping To A Target

by

Kevin Westermann

A thesis  
presented to the University of Waterloo  
in fulfillment of the  
thesis requirement for the degree of  
Master of Applied Science  
in  
Electrical and Computer Engineering

Waterloo, Ontario, Canada, 2019

© Kevin Westermann 2019

I hereby declare that I am the sole author of this thesis. This is a true copy of the thesis, including any required final revisions, as accepted by my examiners.

I understand that my thesis may be made electronically available to the public.

## Abstract

Investigating how humans perform dynamic movements is important for applications such as movement rehabilitation, sports training, humanoid robot design and control, and human-robot interaction. There are several hypotheses as to how humans perform dynamic movements based on movement variability, task optimization, and motor learning concepts. This thesis develops a methodology for analyzing dynamic movements, determining what factors are crucial to task success, and understanding the motor learning process.

The jumping to a target movement was chosen as the exemplar motion for investigating human dynamic motor control because of the following reasons: the movement difficulty can be scaled to a person's physical characteristics and ability; jumping to a target is a movement that many people can perform but few have practiced, making it a good candidate for investigating motor learning; jumping to target has a clear metric for success, enabling novice-expert classification of participants based on objective task performance. Additionally, existing human jumping research has focused primarily on maximum height vertical jumping or maximum distance long jumping. This thesis is the first known work to investigate the kinematics and motor control of the standing broad jump to a target.

An experiment was conducted to collect motion capture data of 22 participants (ages 19-34 years, 9 females and 13 males), each performing 12 jumps to three specified targets of various distances. These motion capture data were used with Extended Kalman Filter pose estimation to extract the kinematic joint trajectories of each jump, and the center of mass (CoM) trajectories were then computed. Analysis of these trajectories then proceeded in two stages. A kinematic trajectory analysis was performed to identify trends between the jumping trajectories and jump success. The identified trends, and other information found in the literature, were used to generate hypotheses for using a sliding window Inverse Optimal Control (IOC) approach for identifying optimized motor control tasks.

The findings from the kinematic trajectory analysis of jumping motion trajectories suggest a strong relation between the jumper controlling the velocity of their CoM at takeoff and the success of the jump. The angle and magnitude of the takeoff velocity must be matched to generate an appropriate ballistic trajectory to reach the desired target. At landing, the jumper can use their foot placement pose to correct for inaccuracy in their takeoff velocity and CoM trajectory to still land on the target. Novice jumpers demonstrated more consistent CoM takeoff velocities as they performed more jumps, however it was less likely that their foot placement control improved noticeably during the study. Expert jumpers were observed to control their foot placement pose more effectively, therefore making higher jumping success rates possible even when the variability of their CoM takeoff velocity was greater than some novice jumpers.

A sliding window IOC approach was used to estimate what motor control tasks jumpers optimize throughout the movement. The cost terms of the objective function were designed based on jumping-specific control tasks and criteria relevant to general human motion. The recovered IOC cost term weights were averaged over different sets of jump features. Changes in average cost term weights were observed relative to jump grade, target distance, and jump performance. Experts were observed to optimize CoM forward velocity before takeoff more than novice jumpers, who optimized CoM height more. As novice jumpers improved their success rate during the experiment, their motor control behavior more closely resembled that of experts. The IOC approach demonstrates evidence for a repeatable, general optimal motor control method for jumping to a target.

Parallels were also drawn between the kinematic trajectory results and IOC motor control task results. Optimizing for the CoM velocity control task before takeoff and toe velocity control task prior to landing, as identified in the IOC results, can be related to controlling takeoff velocity and foot placement pose respectively, as observed in the kinematic analysis.

Finally, the IOC sliding window approach was used alongside unsupervised clustering techniques to identify four jump styles into which experiment participants could be categorized into. All style groups included novice and expert jumpers, and were independent of jump success or motor learning, suggesting there are multiple general motor control patterns that can be used for successfully jumping to a target.

This analysis framework can be extended to analyzing jumping motions in varied environment conditions, or be used to define the motor control methods of other dynamic human motions.

**KEY WORDS:** dynamic human movement, human jumping, motor control, motion variability, inverse optimal control

## Acknowledgements

All academic achievements are part of a larger open system, and I would not have been able to complete this thesis without the many people who have helped me, directly and indirectly. I would like to specifically thank...

My masters supervisor, Dana Kulić, for your constant support and guidance. Your expert feedback has benefited and elevated all my ideas and projects throughout my graduate career. I could not ask for a more knowledgeable, fair and enthusiastic academic mentor.

My thesis manuscript readers, David Wang and John McPhee, for your time in reviewing my thesis. I have had the pleasure of having you both as professors, and your enthusiasm and expertise have always inspired enthusiasm and interest for my own research.

My colleagues and collaborators, Jonathan Lin, Vladimir Joukov, and Brandon DeHart, for the creative and productive brainstorming throughout all my graduate research projects. You made the inevitable tedious portions of graduate research markedly more tolerable, and even enjoyable.

My colleagues in the Adaptive System Laboratory, and other research labs, at the University of Waterloo, for creating a supportive, accepting and energizing working environment. I am grateful to have met each of you and wish you all the best in your future endeavors, academic and otherwise.

My family and friends, for the intellectual and emotional support you have always given me, even when I did not know I needed it. Throughout my university career, and especially during my graduate degree, I have realized the importance of my closest relationships that I may have previously taken for granted. I hope I can contribute to your health and growth as much as you have fostered mine.

## **Dedication**

This work is dedicated to my parents Monika and Gerold for imbuing me with their knowledge and passions, and to Deborah for her constant support and light. I could not be the person I am without you.

# Table of Contents

List of Tables	xi
List of Figures	xii
<b>1 Introduction</b>	<b>1</b>
1.1 Thesis Contributions . . . . .	3
1.1.1 Human Jumping to a Target Dataset . . . . .	3
1.1.2 Kinematic Analysis of Human Jumping to a Target . . . . .	4
1.1.3 Sliding Window Inverse Optimal Control for Human Movement Motor Control . . . . .	4
1.2 Thesis Outline . . . . .	5
<b>2 Background</b>	<b>6</b>
2.1 Human Jumping Motor Control . . . . .	6
2.1.1 Experimental Jumping Data Analysis . . . . .	6
2.1.2 Jumping Simulation and Optimization . . . . .	7
2.1.3 Planar Jumping Model Assumption . . . . .	8
2.2 Extended Kalman Filter . . . . .	8
2.3 Inverse Optimal Control . . . . .	10
2.3.1 System Trajectory . . . . .	11
2.3.2 Direct Optimal Control . . . . .	12

2.3.3	Inverse Optimal Control . . . . .	12
2.3.4	Sliding Window Approach . . . . .	14
2.4	Unsupervised Clustering . . . . .	15
<b>3</b>	<b>Data Collection and Processing</b>	<b>16</b>
3.1	Jumping to a Target Experiment . . . . .	16
3.1.1	Warm-Up . . . . .	18
3.1.2	Distance Calibration . . . . .	18
3.1.3	Jumps to the Target . . . . .	19
3.1.4	Jump Evaluation . . . . .	19
3.1.5	Motion Capture System . . . . .	20
3.1.6	Participant Recruitment . . . . .	21
3.2	Reasoning for Experiment Design . . . . .	21
3.3	Data Post Processing . . . . .	22
3.3.1	Kinematic Model . . . . .	23
3.3.2	Extended Kalman Filter Pose Estimation . . . . .	26
3.3.3	EKF Parameter Optimization . . . . .	27
3.3.4	Temporal Data Alignment . . . . .	27
3.4	Marker Mean Absolute Error Analysis . . . . .	30
3.4.1	Full Body MAE for a Jump . . . . .	30
3.4.2	Overall Average MAE for each Participant . . . . .	31
3.4.3	Average Peak MAE for each Participant . . . . .	32
<b>4</b>	<b>Kinematic Trajectory Analysis</b>	<b>33</b>
4.1	Human Jumping Experiment Observations . . . . .	33
4.2	Joint Trajectories . . . . .	34
4.3	Center of Mass Trajectories . . . . .	38
4.3.1	CoM Takeoff Velocity . . . . .	39



4.3.2	Foot Placement Pose and Leg Stiffness . . . . .	42
4.4	Motor Learning . . . . .	48
4.5	Novice versus Expert Technique . . . . .	52
4.6	Kinematic Trajectory Analysis Conclusion . . . . .	54
<b>5</b>	<b>Inverse Optimal Control Analysis</b>	<b>55</b>
5.1	IOC Parameter Selection . . . . .	56
5.1.1	IOC Cost Function Design . . . . .	57
5.1.2	Trajectory Knot Setting . . . . .	60
5.1.3	Sliding Window Settings . . . . .	60
5.1.4	Normalization of Cost Terms . . . . .	61
5.1.5	IOC and DOC Tolerances . . . . .	62
5.2	IOC Cost Term Weight Trajectory . . . . .	63
5.3	IOC Weight Trajectory Clustering . . . . .	71
5.3.1	Jump Style Analysis . . . . .	71
5.3.2	PCA Clustering Visualization . . . . .	75
5.4	IOC Conclusion . . . . .	78
<b>6</b>	<b>Conclusion</b>	<b>79</b>
6.1	Conclusions . . . . .	79
6.1.1	Human Jumping to a Target Dataset . . . . .	80
6.1.2	Kinematic Analysis of Human Jumping to a Target . . . . .	80
6.1.3	Sliding Window Inverse Optimal Control for Human Movement Motor Control . . . . .	81
6.2	Future Work . . . . .	82
6.2.1	Different Jumping Conditions . . . . .	82
6.2.2	Data Collection and Analysis . . . . .	82
	<b>References</b>	<b>84</b>

<b>APPENDICES</b>	<b>90</b>
<b>A Additional Tables</b>	<b>91</b>
<b>B Additional Figures</b>	<b>98</b>

# List of Tables

4.1	Experiment jump grading statistics . . . . .	34
4.2	Jumping experiment participant statistics . . . . .	53
5.1	List of IOC parameters . . . . .	56
5.2	Final IOC cost term set . . . . .	59
5.3	IOC and DOC computation time . . . . .	63
A.1	Motion capture marker information . . . . .	92
A.2	Kinematic model joint names and locations . . . . .	93
A.3	Marker MAE - average . . . . .	94
A.4	Marker MAE - peak . . . . .	95
A.5	Number of perfect jumps in experiment . . . . .	96
A.6	All hypothesized IOC cost terms . . . . .	97

# List of Figures

2.1	IOC sliding window approach . . . . .	15
3.1	Phases of the standing broad jump . . . . .	17
3.2	Experiment protocol flow chart . . . . .	18
3.3	Motion capture marker placement . . . . .	21
3.4	Kinematic jumping model . . . . .	24
3.5	Temporal alignment of sample joint trajectories . . . . .	29
3.6	Full body marker mean absolute error . . . . .	31
4.1	Example joint trajectories . . . . .	36
4.2	Jump colour coding legend . . . . .	37
4.3	Example CoM trajectories . . . . .	39
4.4	Projectile motion - constant distance . . . . .	40
4.5	Example CoM takeoff velocities . . . . .	41
4.6	Projectile motion - changing elevation . . . . .	43
4.7	Example trajectories - foot placement . . . . .	46
4.8	Example trajectories - leg stiffness . . . . .	47
4.8	Example trajectories - motor learning . . . . .	50
4.9	Example trajectories - motor learning for foot placement . . . . .	51
5.1	IOC cost term weight trajectories . . . . .	64
5.2	IOC mean weights - all jumps . . . . .	65

5.3	IOC mean weights - target distance . . . . .	68
5.4	IOC mean weights - jump grade . . . . .	69
5.5	IOC mean weights - expert vs. novice . . . . .	70
5.6	IOC weight clustering - group A . . . . .	72
5.7	IOC weight clustering - group B . . . . .	73
5.8	IOC weight clustering - group C . . . . .	74
5.9	IOC weight clustering - group D . . . . .	75
5.10	IOC clustering PCA visualization . . . . .	76
5.11	IOC clustering PCA visualization - individual jumpers . . . . .	77
B.1	Additional joint trajectory examples . . . . .	100

# Chapter 1

## Introduction

Investigating how humans perform dynamic movements is important for many applications. Analysis of motor control behavior can be useful for movement rehabilitation and sports training, in order to help those who are injured or otherwise limited in their mobility to (re)attain efficient and effective movement [63] [62] [8]. Human motor control strategies can also be used to replicate human-like movement on humanoid and other robot platforms [45] [14], and machines that interact with humans in social environments benefit from a model of human behavior to predict their future actions [7] [55] [31].

There are several hypotheses as to how humans perform and learn dynamic movements. The theory of task optimization recognizes that humans typically optimize a set of criteria when moving, and the central nervous system translates these high-level goals into low-level motor control behavior [51] [57]. Movement variability analysis investigates variations in kinematic behavior and motor performance that occur when performing a movement task [38] [13] [6]. Research on motor learning investigates changes in motor control that result from repeated movement practice, usually leading to an increase in task success [1] [51] [52]. The focus of this thesis is to develop a methodology for analyzing dynamic human movement by identifying what features or characteristics are crucial to task success, and understanding optimal motor control behavior required to complete the movement.

To study the aforementioned motor control concepts, jumping to a target was selected as an example dynamic movement. Jumping motions are highly dynamic and require full-body coordination to complete successfully. Jumping has a clear task objective and metric of success (such as jumping as high/far as possible, jumping to a specific location, or landing with minimum impact force), which facilitates investigating task optimization. Jumping is also a suitable candidate for movement variability analysis; the task objective

is low dimensional yet the human body is an articulated kinematic system with redundant degrees of freedom (for complete jumping movements), affording for variability in joint trajectories [38] [57].

The movement of jumping to a target (aiming to land in a pre-determined location) was specifically chosen for this project for the following reasons: first, the movement can be easily scaled to a person’s physical characteristics and ability by adjusting the distance to the landing target. Second, jumping to a target is a movement that many people can perform but few have practiced. This makes the movement a good candidate for investigating motor learning, as participants’ first experience with jumping to a target can be captured in a lab experiment setting, and their motor control behavior relative to their jump success can be observed as they gain more experience with jumping to a target. The technique of jumpers who are adept at the movement can be compared to unpracticed jumpers to observe differences in kinematic trajectories and motor control.

Third, jumping to target can be easily rated for success, enabling novice-expert classification of participants based on task performance rather than physical ability/experience assessed before data collection.

Finally, existing human jumping research has focused primarily on maximum height vertical jumping or maximum distance long jumping (described in detail in Section 2.1). This thesis is the first known work to investigate the kinematics and motor control of the standing broad jump to a target, as further explained in Section 1.1. Analyzing trajectory data for jumping to a target could yield information about kinematic features and muscle coordination strategies that differ from those used when jumping for maximum distance/height.

To provide a dataset for analysing motor control performance, an experiment was designed around the jumping to a target movement. 22 participants (ages 19-34 years, 9 females and 13 males) performed 36 jumps to three different target distances, scaled to each participant to approximately provide an easy, medium, and difficult jumping distance. Each jump was assigned a jump grade based on how close the jumper landed to the target, forming the metric of task success. Jumps to different targets were ordered into sets to observe changes in jumping behavior due to motor learning throughout the experiment. Participants with and without previous experience in jumping to a target were recruited. A motion capture system was used to record the jumping kinematic data.

A full body kinematic model was formed for each participant based on experimental measurements and anthropometric data [25] [15]. Pose estimation filtering was used to transform the motion capture data into joint trajectories for the kinematic model [30], and these trajectories were then temporally aligned to one another for direct comparison of

jump trajectories.

The aligned trajectory data were used to perform two types of analysis. The first was a direct analysis of the kinematic trajectories and features calculated from the trajectory data, specifically, center of mass (CoM) trajectories and the timing of jump phases. Momentum generation and the CoM are crucial for investigating jumping motions, as projectile physics principles govern the trajectory of the CoM during the flight phase of a jump. The trajectories and features were compared to jump grading, jumper performance and motor learning. The velocity of the CoM at takeoff and the foot placement pose of the body (position of the CoM relative to the foot) at landing were found to be the most influential kinematic features for successfully jumping to a target.

A primary goal of this thesis was to create and test a framework for identifying the motor control tasks humans optimize when executing dynamic movements. These identified control patterns could then be used towards controlling a humanoid robot to replicate these dynamic movements. Inverse optimal control (IOC) was employed for the identification of motor control tasks based on input kinematic trajectories. The optimization function was composed of a weighted sum of cost terms, representing hypothesized motor control tasks the human may use to execute the input jump trajectory. An IOC solver was used to recover the relative weights of the cost terms, which represent the set of motor control tasks used to complete the motion.

A sliding window approach was used in conjunction with IOC to observe how motor control task priority changes throughout the jumping motion, removing the common IOC assumption (and restriction) of having constant cost term weights over the entire input trajectory [16]. The sliding window approach has previously been used for motion segmentation [39]. The cost term weight trajectories of all jumps from the experiment were compared to see how motor control patterns changed with respect to jump success, target distance, jumper expertise and motor learning.

## 1.1 Thesis Contributions

The novel contributions of this thesis are:

### 1.1.1 Human Jumping to a Target Dataset

The great majority of existing human jumping research has focused on maximum vertical jumping [9] [12] [48] [17], maximum (forward) distance jumping [50] [59] [5] [27], or the basic



muscle coordination and dynamics required to perform a jump of any kind (i.e. leaving the ground to enter the flight phase) [42] [47].

Recently, Maldonado *et al.* reported on the precision jump in parkour [41], which is the only literature known to this author that has investigated human jumping to a specified landing location. Maldonado analyzed depth jumping for seven male expert participants, and focused on identifying motor control tasks for a safe and stable landing. This thesis contributes a new dataset of human jumping to a target. The dataset includes 22 participants, both novices and experts, male and female, and includes kinematic data and success ratings for multiple repetitions of jumps to 3 targets of varying difficulty. The dataset enables study of dynamic movement, movement variability and motor learning.

### 1.1.2 Kinematic Analysis of Human Jumping to a Target

This thesis is the first to analyze the motion of the standing broad jump to a target from a kinematics and motor control standpoint, with the goal of identifying the differences in kinematic and motor control data that contribute to jumping task success (landing on the specified target) or failure.

Analysis of the experimental data revealed CoM takeoff velocity and the pose of the body at landing (i.e. the position of the CoM relative to the feet) to be the most influential kinematic features to jump success. The takeoff velocity of the CoM must be controlled for the jumper to have an appropriate projectile trajectory during the flight phase of the jump to reach the desired target. When landing, the jumper can control their pose to make sure their feet land on the target location, and to correct for minor inaccuracies in their takeoff velocity and flight phase trajectory.

The kinematic data were also analyzed relative to jumper performance (overall success rate) and motor learning observations. Novice jumpers were found to exhibit more motor learning than experts during the experiment, and saw improvement in the consistency of their takeoff velocity. Expert jumpers by definition had higher jump success rates, and were observed to have more control over their foot placement pose, and therefore more adaptability to takeoff velocity inaccuracies.

### 1.1.3 Sliding Window Inverse Optimal Control for Human Movement Motor Control

Inverse Optimal Control (IOC) for human movement analysis has previously been applied for investigating optimal human movement patterns [8] [40] [49], human motion segmen-

tation [39], and imitation learning for humanoid robot control motion primitives [45] [14]. In this thesis an IOC sliding window approach was used for the first time to test motor control hypotheses of jumping data. This sliding window approach has previously been applied to human motion data for the purposes of motion segmentation, however, using this approach for identifying motor control tasks and how they change throughout human motion trajectories is a novel application of the method.

## 1.2 Thesis Outline

Chapter 2 provides background information on human jumping movement and methodologies used for analysis throughout the thesis. An overview of human jumping control, pose estimation methods, inverse optimal control and unsupervised clustering is provided.

Chapter 3 outlines the design of the experiment used to collect the human motion dataset, and details data post-processing techniques for pose estimation and temporal data alignment.

Chapter 4 investigates the joint and center of mass (CoM) trajectories and calculated features. Changes in trajectory features are related to jump success, trajectory variability within jump sets, jumper performance and motor learning. The CoM takeoff velocity and the body pose at landing are discussed based on their influence on jump success.

Chapter 5 outlines the use of an IOC approach to determine which hypothesized motor control tasks are optimized throughout each jump trajectory, and how these control tasks change during different jumping phases. The recovered cost term weights are investigated and compared between different sets of jumping data to identify motor control changes with respect to jump success, target distance, jumper performance and motor learning. Unsupervised clustering is used to categorize participants based on their jumping style.

Chapter 6 reviews the novel contributions and results of the thesis, and concludes with the findings about motor control that are required for successfully jumping to a target. Directions of future work to expand and validate the motion analysis framework presented in this thesis are discussed.

# Chapter 2

## Background

This chapter reviews the existing methodologies for human motion analysis and human motor control used in this thesis.

### 2.1 Human Jumping Motor Control

While humans can perform a broad range of movements, most analysis to date has focused on a small subset of movements. Human balancing and walking patterns have been studied extensively [35] [60] [43], and the development of humanoid and other legged robots have encouraged further research into human control patterns for their application to humanoid robot control [23] [61] [14].

Human jumping is a dynamic and full-body movement, where the jumper temporarily breaks contact with the ground. Enough momentum is generated by the legs to leave the ground (entering the “flight phase”), and then absorb the impact of their body against the ground when they land. Existing human jumping research typically focuses on analyzing data from human participants, or uses a model of the body to simulate the kinematics and dynamics of jumping motions. Additionally, the majority of jumping research has investigated maximum height vertical jumping or maximum distance long jumping.

#### 2.1.1 Experimental Jumping Data Analysis

Early human jumping research typically aimed to determine the joint torque contributions and muscle coordination patterns in the leg required for optimal (i.e. maximum distance

or height) jumping, usually employing image and force plate data for human motion analysis. Robertson and Flemming [50] determined that hip, knee and ankle extension during the takeoff phase of jumping contribute different percentages of propulsion for vertical and standing broad jumping, and that extensor muscle groups at these joints contract simultaneously to produce the leg extension. Bosco *et al.* [9] observed greater mechanical efficiency of vertical jumping when incorporating pre-stretching of the extensor muscles at the knee during the takeoff phase, as well as increased efficiency when the knee started from a more extended position. Özgüven and Berme [47] used force plates to measure impact forces during vertical and depth jump landings, and predicted spring, damper and inertial parameters of a 2 degree of freedom model based on experimental and anthropological data.

Studies have also investigated optimal human jumping behavior based on experimental data. Wakai and Linthorne [59] analyzed the standing broad jump performed at various takeoff angles and determined that an angle between 19 and 27 degrees to the horizontal was the optimum takeoff angle to achieve maximum distance. Ashby [5] compared motion trajectories of jumpers using their arms normally and constraining their arms to the torso. Jumpers travelled 21% farther when able to use their arms, and were observed to swing their arms to counter the forward angular momentum produced by the legs and torso, enabling greater overall linear momentum to be generated at takeoff. Without the influence of the arms, a jumper must eliminate excessive forward body rotation before entering the flight phase.

### 2.1.2 Jumping Simulation and Optimization

As computing resources became more powerful and widely available, dynamic model simulations have been utilized more often for human jumping research. Pandy *et al.* [48] developed a simple four link planar model and used a dynamic optimization algorithm to control the model to perform a maximum height jump. Guihard and Gorce [22] expanded on the work of Pandy by developing a controller for vertical jumping for use with biped control of planar, three link rigid body legs. Cheng *et al.* [12] investigated the role of arm motion in vertical jumping with a dynamic four or five link model (with and without arms), finding the optimal joint activation timing to result in the greatest jump height. The results were used to explain the validity of multiple human movement energy generation theories.

### 2.1.3 Planar Jumping Model Assumption

The majority of simulated human jumping works use 2D dynamic models constrained to the sagittal plane. Meghdari and Aryanpour [42] developed a full body, sagittal plane dynamic jumping model framework that could calculate and reproduce the kinematics and dynamics of real jump trajectories recorded through image data. However, Hickox *et al.* [27] simulated recorded experiment data with both 2D and 3D models and determined that a 2D planar assumption was not appropriate for a full body jumping model, as shoulder abduction/adduction and elbow flexion produce significant power that cannot be properly examined without a 3D model.

## 2.2 Extended Kalman Filter

The Extended Kalman filter (EKF) is a data filtering method used for state estimation of nonlinear systems [21]. Discrete time EKF uses a state update step to predict the system state  $\mathbf{x}_{k+1}$  based on the current state  $\mathbf{x}_k$ , control input  $\mathbf{u}_k$  and state uncertainty  $\mathbf{w}_k$ :

$$\mathbf{x}_{k+1} = f(\mathbf{x}_k, \mathbf{u}_k) + \mathbf{w}_k \quad (2.1)$$

A measurement update step uses the current system measurement  $\mathbf{z}_k$  and measurement noise  $\mathbf{v}_k$  to update the state prediction. The state prediction and measurement updates are combined based on the relative process and observation noise and covariance. The state update equations are:

$$\mathbf{x}_{k|k} = f(\mathbf{x}_{k-1|k-1}, \mathbf{u}_k) \quad (2.2)$$

$$P_{k|k-1} = F_k P_{k-1|k-1} F_k^T + Q_k \quad (2.3)$$

where  $P$  is the covariance estimate, and  $Q$  is the process noise. The measurement update equations are:

$$\mathbf{y}_k = \mathbf{z}_k - h(\mathbf{x}_{k|k-1}) \quad (2.4)$$

$$S_k = H_k P_{k|k-1} H_k^T + R_k \quad (2.5)$$

$$K_k = P_{k|k-1} H_k^T S_k^{-1} \quad (2.6)$$

$$\mathbf{x}_{k|k} = \mathbf{x}_{k|k-1} + K_k \mathbf{y}_k \quad (2.7)$$

$$P_{k|k} = (I - K_k H_k) P_{k|k-1} \quad (2.8)$$

where  $h$  is the objective function that relates the measurement to the state,  $R$  is the observation noise,  $S$  is the residual covariance, and  $K$  is the Kalman gain. The state transition matrix  $F$  and observation matrix  $H$  are defined as:

$$F_k = \frac{\partial f}{\partial x} \Big|_{\mathbf{x}_{k-1|k-1}, \mathbf{u}_k} \quad (2.9)$$

$$H_k = \frac{\partial h}{\partial x} \Big|_{\mathbf{x}_{k|k-1}} \quad (2.10)$$

The EKF formulation can be used for human pose estimation with a human kinematic model (typically formed with rigid links connected with revolute and prismatic joints [2]) and a variety of motion measurement techniques, including motion capture markers [3] and inertial measurement units [53]. The state is formed by vectorizing the positions, velocities, and accelerations of the model joints,  $\mathbf{x} = [\mathbf{q}, \dot{\mathbf{q}}, \ddot{\mathbf{q}}]^T$ . A constant acceleration model can be used to update the state [30]:

$$\mathbf{x}_{k+1} = \begin{bmatrix} 1 & dt & dt^2/2 \\ 0 & 1 & dt \\ 0 & 0 & 1 \end{bmatrix} \mathbf{x}_k + \mathbf{w}_k \quad (2.11)$$

where  $dt$  is sampling rate. If a motion capture measurement system is used,  $M$  markers placed on the body generate Cartesian trajectories  $\mathbf{s}$  of the markers, forming the measurement:

$$\mathbf{z}_k = [\mathbf{s}_{M,k}] \quad (2.12)$$

Forward kinematics are used to relate the measurements to the current state (joint rotations/translations). Homogeneous transforms  $A_i(q_i)$  define the relative translations and orientations of each link along each serial chain between the base frame (typically at the pelvis) and each end effector (hands, feet, head) [56]:

$$A_i(q_i) = \begin{bmatrix} R_i^{i-1}(q_i) & \mathbf{p}_i^{i-1}(q_i) \\ 0 & 1 \end{bmatrix} \quad (2.13)$$

where  $q_i$  is the  $i^{\text{th}}$  joint,  $R_i^{i-1}$  is the rotation matrix, and  $p_i^{i-1}$  is the translation vector from link  $i - 1$  and link  $i$ . The forward kinematics from the model base to frame  $j$  can be computed by multiplying successive homogeneous transformation matrices along the corresponding serial chain:

$$T_j^0 = A_0(q_0)A_1(q_1) \dots A_j(q_j) \quad (2.14)$$

The Jacobian  $J$  for the rigid body model is calculated by taking the partial derivative of the  $M$  measurement variables  $s$  with respect to the  $N$  degrees of freedom of the model joints  $q$ :

$$J = \begin{bmatrix} \frac{\partial x_1}{\partial q_1} & \dots & \frac{\partial x_1}{\partial q_N} \\ \vdots & \ddots & \vdots \\ \frac{\partial x_M}{\partial q_1} & \dots & \frac{\partial x_M}{\partial q_N} \end{bmatrix} \quad (2.15)$$

The Jacobian corresponds to the observation matrix  $H$  in Equation 2.10.

## 2.3 Inverse Optimal Control

Optimal control theory is used to determine the control inputs that will enable a dynamic system to optimize some performance criterion [36]. A dynamic system can be modelled with the following set of equations describing the relationship between the state variables  $\mathbf{x}$ , control variables  $\mathbf{u}$ , and plant outputs  $\mathbf{y}$ :

$$\dot{\mathbf{x}}(t) = f_x(\mathbf{x}(t), \mathbf{u}(t)) \quad (2.16)$$

$$\mathbf{y}(t) = f_y(\mathbf{x}(t), \mathbf{u}(t)) \quad (2.17)$$

The objective during optimal trajectory generation is to produce a trajectory of state  $\mathbf{x}^*$  and control input  $\mathbf{u}^*$  such that a given performance criterion is optimized.

The performance criterion is usually in the form of a cost function, and an optimal control solver minimizes the cost function based on the system model and its constraints. The cost function can be defined as a sum of cost terms  $J_{ct}$  with relative weighting coefficients  $w$ :

$$J(\mathbf{x}) = \sum_{i=0}^{n_{ct}} w_i J_{ct,i}(\mathbf{x}) \quad (2.18)$$

where  $n_{ct}$  is the number of cost terms.

Direct optimal control (DOC) requires  $J_{ct}$  and  $w$  to be defined, and then the optimal system trajectory  $\mathbf{x}^*$  and  $\mathbf{u}^*$  can be generated based on the cost function. For human motion analysis, the system state corresponds to:

$$Q^* = [\mathbf{q}^*, \dot{\mathbf{q}}^*, \ddot{\mathbf{q}}^*] \quad (2.19)$$

where  $\mathbf{q}^*$ ,  $\dot{\mathbf{q}}^*$  and  $\ddot{\mathbf{q}}^*$  are the optimal position, velocity and acceleration of the states, respectively.

Inverse optimal control (IOC) is used to solve the reciprocal problem: from an observed system trajectory,  $Q_{obs}$ , estimate the optimal cost term weights  $\hat{w}$ . DOC can then be used to simulate  $\hat{Q}_{obs}$  based on  $\hat{w}$ , and determine the goodness-of-fit by comparing  $Q_{obs}$  and  $\hat{Q}_{obs}$ . The remainder of this background section is based on Lin's IOC approach described in [39].

### 2.3.1 System Trajectory

System state trajectories are represented as piecewise quintic polynomial splines to reduce the dimensionality of  $Q_{obs}$ , modelling the trajectory along spline control knots (rather than defining the entire trajectory). Polynomial splines also allow trajectory derivatives to be computed analytically.

Spline control knots are evenly distributed at time locations  $t_{ck}$ . The full trajectory set is formed by joint position  $\mathbf{q}_{ck} = \mathbf{q}(t_{ck})$ , velocity  $\dot{\mathbf{q}}_{ck} = \dot{\mathbf{q}}(t_{ck})$ , and acceleration  $\ddot{\mathbf{q}}_{ck} = \ddot{\mathbf{q}}(t_{ck})$  trajectories.



### 2.3.2 Direct Optimal Control

Given  $w$  and  $t_{ck}$ , DOC generates the  $\mathbf{q}_{ck}$ ,  $\dot{\mathbf{q}}_{ck}$ , and  $\ddot{\mathbf{q}}_{ck}$  that minimize  $J(\mathbf{x})$ . The optimized control knots (denoted as  $\mathbf{q}_{ck}^*$ ) generate a spline that defines the optimal trajectory  $Q_{obs} = [\mathbf{q}_{ck}^*; \dot{\mathbf{q}}_{ck}^*; \ddot{\mathbf{q}}_{ck}^*]$ . The constrained optimization problem is defined as:

$$\min_{\mathbf{x}} J(\mathbf{x}) \quad s.t. \quad h(\mathbf{x}) = 0, g(\mathbf{x}) \leq 0 \quad (2.20)$$

where  $h(\mathbf{x})$  are the equality constraints and  $g(\mathbf{x})$  are the inequality constraints. Equation 2.20 is modified into:

$$\min_{\mathbf{x}=\mathbf{q}_{ck}, \dot{\mathbf{q}}_{ck}, \ddot{\mathbf{q}}_{ck}} J(x) = \sum_{i=0}^{n_{ct}} c_i J_{ct,i}(Q_{obs}) \quad (2.21)$$

$$s.t. \quad h(\mathbf{x}) = \begin{cases} \mathbf{q}(t_{const,q}) - \mathbf{q}_{const} = 0 \\ \dot{\mathbf{q}}(t_{const,dq}) - \dot{\mathbf{q}}_{const} = 0 \\ \ddot{\mathbf{q}}(t_{const,ddq}) - \ddot{\mathbf{q}}_{const} = 0 \end{cases}$$

where  $\mathbf{q}_{const}$ ,  $\dot{\mathbf{q}}_{const}$ , and  $\ddot{\mathbf{q}}_{const}$  denote the joint position, velocity, and acceleration constraints, respectively, and  $t_{const,q}$ ,  $t_{const,dq}$ ,  $t_{const,ddq}$  refer to their corresponding time points. These constraints form the equality constraints  $h(\mathbf{x})$  of the system. This thesis does not include any inequality constraints  $g(\mathbf{x})$  (such as joint and torque limits).

To solve the DOC problem the trust region optimization method was used [11]. An initial trajectory is formed with quintic splines, constrained at the starting and ending points of  $\mathbf{q}$ ,  $\dot{\mathbf{q}}$  and  $\ddot{\mathbf{q}}$ . Joint values at  $t_{ck}$  are used to initialize  $\mathbf{q}(t_{ck})$ . At each optimization step,  $\mathbf{q}_{ck}$ ,  $\dot{\mathbf{q}}_{ck}$ , and  $\ddot{\mathbf{q}}_{ck}$  are used to create the spline, then features required to calculate  $J_{ct}$  are determined.

### 2.3.3 Inverse Optimal Control

For the IOC problem,  $\mathbf{q}_{ck}$  is known and  $w$  must be estimated, denoted as  $\hat{w}$ . The inverse Karush-Kuhn-Tucker (KKT) [10] optimality criteria are used to find the optimal IOC solution. KKT-based methods are faster than other iterative optimization methods as the IOC cost term weights and reconstructed trajectory are only computed once, however, the gradient must also be modelled explicitly [16].

For a constrained system in the form of Equation 2.20, the KKT conditions state that a given solution  $\mathbf{x}^*$  is optimal if the following conditions are met:

$$\begin{aligned}\nabla_x J(\mathbf{x}^*) &= \sum_{i=0}^{n_f} w_i \nabla_x f_i(\mathbf{x}^*) + \sum_{j=0}^{n_h} \lambda_j \nabla_x h_j(\mathbf{x}^*) + \sum_{k=0}^{n_g} \nu_k \nabla_x g_k(\mathbf{x}^*) = 0 \\ h_j(\mathbf{x}^*) &= 0 \\ g_k(\mathbf{x}^*) &\leq 0 \\ \nu_k g_k(\mathbf{x}^*) &= 0 \\ \nu_k &\geq 0\end{aligned}$$

where  $\nabla_x$  denotes the gradient operator, while  $\lambda$  and  $\nu$  represent the KKT multipliers for the equality  $h$  and inequality  $g$  constraints, respectively.

Given the DOC cost function and constraints in Equation 2.21, the KKT Lagrangian  $L(\mathbf{x} = \mathbf{q}_{\text{ck}}, \dot{\mathbf{q}}_{\text{ck}}, \ddot{\mathbf{q}}_{\text{ck}})$  and its gradient  $\nabla_x L(\mathbf{x})$  are defined as:

$$\begin{aligned}L(\mathbf{x}) &= \sum_{i=0}^{n_{ct}} \hat{w}_i J_{ct,i}(Q_{obs}) + \sum_{j=0}^{n_h} \lambda_j h_j(Q_{obs}) \\ \nabla_x L(\mathbf{x}) &= \sum_{i=0}^{n_{ct}} \hat{w}_i \nabla_x J_{ct,i}(Q_{obs}) + \sum_{j=0}^{n_h} \lambda_j \nabla_x h_j(Q_{obs})\end{aligned}$$

where the partial differential of the gradient  $\nabla_x$  is calculated with respect to the state variables  $\mathbf{q}_{\text{ck}}$ ,  $\dot{\mathbf{q}}_{\text{ck}}$ , and  $\ddot{\mathbf{q}}_{\text{ck}}$ ,  $\lambda$  are the Lagrangian multipliers on  $h(\mathbf{x})$ ,  $Q_{obs}$  is constructed from the spline representation of the trajectory, and  $n_h$  denotes the total number of  $h(\mathbf{x})$  constraints. The optimality condition to be met is defined as:

$$\nabla_x L(Q_{obs}) = 0 \tag{2.22}$$

If the system is assumed to be only approximately optimal [34], then Equation 2.23 is minimized:

$$\min_{\hat{c}, \lambda} \nabla_x L(Q_{obs}) \quad s.t. \quad \hat{c} \geq 0 \tag{2.23}$$

Therefore, the system being optimized achieves a near-optimal state by minimizing the KKT residual error in Equation 2.23. The KKT equations are linear with respect to  $\hat{w}$  and  $\lambda$ , so Equation 2.23 can be solved efficiently as a least squares problem [39].

To prevent trivial solutions, a *pivoting* method is used, where one value of  $\hat{w}$  is set to a non-zero value, and is called the pivot. If no prior knowledge of the nature of the cost terms  $J_{ct}$  is assumed, all cost terms are used as the pivot, defining the best fit by selecting the entry with the smallest KKT residual error. The  $i^{th}$  pivot is constructed by setting  $\hat{w}_i = 1$  and solving for all remaining  $\hat{w}$  relative to  $\hat{w}_i$ .

The IOC process is applied over a sliding window over  $Q_{obs}$  to recover  $\hat{w}$  over the trajectory within that window (see 2.3.4 for details). Some windows of a certain size or location can lead to degenerate solutions for  $\hat{w}$ . In these cases, the residual norm can be used as an indicator of the quality of  $\hat{w}$ . Once the pivot with the lowest residual error has been selected, the trajectory  $\hat{Q}_{obs}$  can be generated for the corresponding window using DOC.

### 2.3.4 Sliding Window Approach

Most existing IOC approaches assume that the optimal cost function of the system is constant over the entire trajectory [16]. This assumption is likely not valid, especially for motions like jumping where there are distinct phases that have different motion objectives (takeoff, flight, landing). To capture time varying motion objectives, a sliding window approach can be used [39]. Rather than performing the IOC analysis over the entire motion trajectory, this approach performs IOC over several overlapping windows. The primary advantage of this approach is that the cost function is not required to be constant, since  $\hat{w}$  can change throughout the trajectory as the motion objectives change.

The sliding window approach consists of solving for  $\hat{w}$  over a small window of the entire trajectory, then sliding the window forward and repeating the process. Once IOC is applied to all trajectory windows, results are aggregated to form the *blended metric*. The blended cost term weights  $\bar{w}_t$  at time  $t$  are calculated by taking the average of all  $\hat{w}$  from all windows that overlap frame  $t$ . This process is shown graphically in Figure 2.1.

The blended  $\bar{Q}_{obs}$  at time  $t$  is calculated similarly, by averaging the reconstructed DOC trajectories of all windows that overlap time  $t$ . The blended root mean squared error (RMSE) is calculated between the input trajectory  $Q_{obs}$  and the blended estimated trajectory  $\bar{Q}_{obs}$ .

At each point in the motion trajectory  $\bar{w}$  is interpreted as the relative optimization priority of each corresponding motor control task at that time in the trajectory. Changes

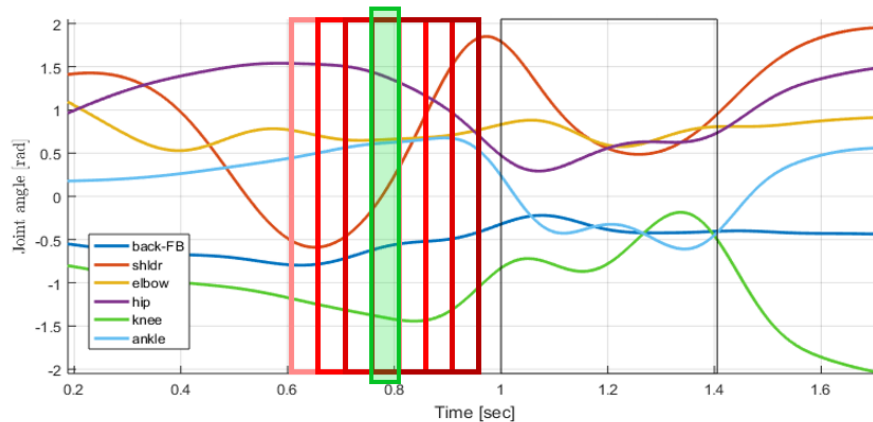


Figure (2.1) Diagram of IOC sliding window approach. Four windows (different shades of red) overlap the frames within the green region of a system trajectory. The recovered  $\hat{w}$  from each red window are averaged to form the final recovered weights for the frames in the green region.

in  $\hat{w}$  identify distinct phases in the performed motion. By comparing multiple motion trajectories and their corresponding  $\hat{w}$ , optimized motor control tasks may be related to certain features of the input trajectory.

## 2.4 Unsupervised Clustering

Clustering is a data analysis technique that groups together sets of objects such that objects within a group are more similar to each other than objects belonging to different groups [32]. Unsupervised clustering methods group objects together without using any category or label information.

One of the most common and general-purpose unsupervised clustering algorithms is the “kmeans” algorithm, where observations are clustered into a set number of groups based on the distance between each observation and each group centroid, iteratively updating centroid locations. An extension to this method is the kmeans++ algorithm [4], which provides a heuristic for finding group centroid seeds, and is purported to improve the runtime and the quality of the clustering solution.

# Chapter 3

## Data Collection and Processing

This chapter first details the design of the jumping experiment and motion capture data recording protocol. Data post processing techniques were then used to transform the raw experimental data into forms suitable for further analysis; an Extended Kalman Filter approach was used for human pose estimation and extraction of joint trajectories, along with subsequent temporal trajectory alignment.

### 3.1 Jumping to a Target Experiment

The experiment consisted of capturing the motion data of human participants completing multiple jumps to a pre-defined target location. All jumping motions in the study were standing broad jumps to a target, starting with both feet on the ground, jumping with both feet leaving the ground at approximately the same time (takeoff), and then landing with both feet contacting the ground at approximately the same time. The phases of jumping to a target are shown in Figure 3.1. At the beginning of each jump the participant stood in a calibration pose for two seconds, and then dropped their arms to their sides and stood in a normal upright position for two more seconds (for data processing and motion segmentation purposes). The participant would then execute the jumping action, and after landing and stabilization the participant entered the calibration pose once more before the recording was stopped.

A participant's maximum standing broad jump distance was used to scale the landing target distances to the physical abilities of the jumper. Participants then completed six jumps to each of three target distances. This protocol was repeated a second time before

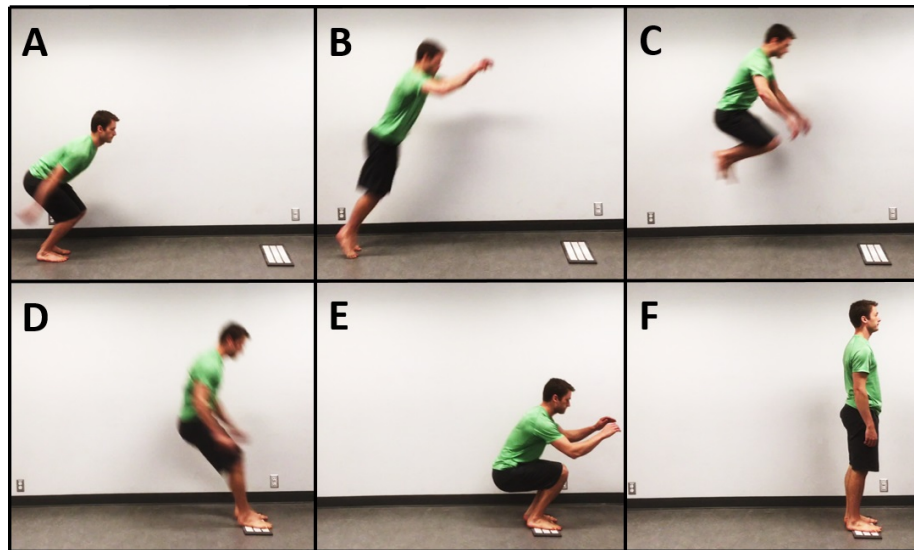


Figure (3.1) Phases of the standing broad jump: (A) start of takeoff phase, (B) takeoff, (C) flight, (D) ground contact at landing, (E) landing, and (F) finish. The white platform at the landing location is the same platform used in the experiment.

the experiment was completed. Figure 3.2 illustrates the main steps of the experiment data collection, which are detailed throughout the rest of this section.

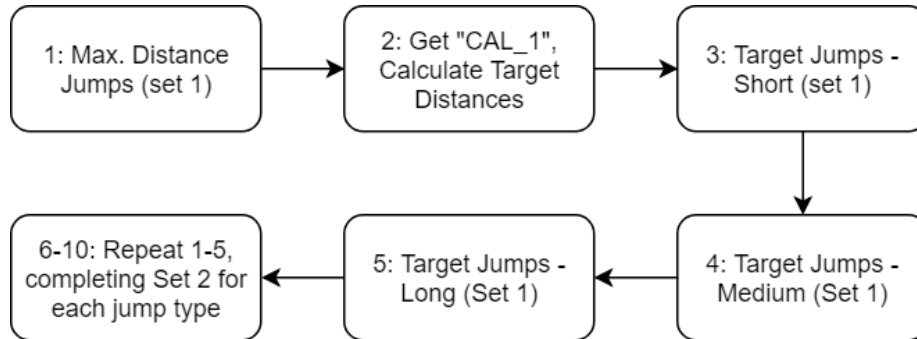


Figure (3.2) Flow chart depicting the primary steps in the jumping experiment protocol. Six jumps are completed in each target jump set.

### 3.1.1 Warm-Up

Each participant began by completing a series of jumping-related warm-up movements, consisting of light jogging, lunges, and vertical and horizontal jumping movements that became progressively harder. The warm-up period took approximately 10 minutes. Several studies have concluded that a warm-up period of easy to moderate exercise prior to vigorous exercise can decrease the risk of injury during exercise and increase performance [19]. Additionally, movement-specific warm-up exercises have been shown to improve performance in the movement task [54].

### 3.1.2 Distance Calibration

Participants then completed a set of three jumps for maximum distance. These jumps were measured from the takeoff line to the heel of the foot farthest back in the landing position, then the average of the three maximum distance jumps formed the participant's first calibration distance, *CAL*-1. This distance was then used to compute the three "target jump" distances.

Next, the target landing platform was anchored to the floor. The landing platform was a 10 mm thick foam flooring mat, 203 mm (8") wide and 610 mm (24") long, with the long dimension placed perpendicular to the jump direction, as shown in Figure 3.1. The size of the landing platform was experimentally chosen as a realistic area that most people (able to complete a standing broad jump) would be able to land on successfully from a relatively short distance, but would be difficult to land on from a longer distance without practice. Three takeoff lines were marked on the floor at distances of 55% (short), 70% (medium),

and 85% (long) of the *CAL\_1* distance, measured from each start line to the centre of the target platform.

### 3.1.3 Jumps to the Target

Participants completed a set of 6 jumps to each target, starting from the shortest (55%) to longest (85%) distance. For each jump, the takeoff line and target platform were recorded with additional motion capture markers. The target distance lengths, relative to percentages of maximum jump distance, were experimentally chosen to provide easy, medium, and difficult jump distances, relative to the size of the landing platform (as discussed above). The target distances were scaled so there were both easy and difficult jumps to perform, making it more likely that the dataset included samples of both successful and unsuccessful jumps.

The protocol described above was then repeated a second time. A second set of three maximum distance jumps were completed and their average distance formed *CAL\_2*. If *CAL\_2* was less than *CAL\_1*, the second set target distances remained scaled based on *CAL\_1*. Otherwise, three new target distances were calculated as 55%, 70%, and 85% of *CAL\_2*, and sets of 6 jumps were completed to each of these new target distances. This protocol resulted in 36 total jumps to the target completed by each participant.

Participants 02, 14, 17 and 20 were able to jump far enough (based on their jumping ability or height) that the capture volume of the motion capture system was not large enough to accurately record the takeoff and landing motions. In these cases the 85% jump distance (third target) was made less than the actual “ $0.85 * CAL_{\#}$ ” value in order to remain within the capture volume of the motion capture system, and maintain accurate marker position data.

### 3.1.4 Jump Evaluation

Each jump was assigned an evaluation grade by the experimenter during the data collection. Landing with the ball of the foot centered over the target landing platform was the most desirable, and a stable and controlled landing was graded more favorably than a landing requiring corrective balance motions with the arms and torso. The participant’s ability to “stick the landing” on the target platform during each jump was classified as one of the grades listed below. This jump evaluation score provides a subjective, expert metric to evaluate each jump’s success.



- B: landed to the back of the target, a portion of the feet touching the floor; unsuccessful jump
- SB: landed slightly back of the middle of the target, may have needed balance corrections to stabilize
- P: landed in the middle of the target with control; successful jump
- P\*: landed in the middle of the target, needed balance corrections to stabilize; successful jump but lacking control at landing
- SF: landed slightly forward of the middle of the target, may have needed balance corrections to stabilize
- F: landed forward of the target, a portion of the feet touching the floor; unsuccessful jump

### 3.1.5 Motion Capture System

The motion capture equipment used in the study was an 8 camera Eagle [Motion Analysis](#) Infrared camera system. Each participant was outfitted with 30 reflective markers at the body locations shown in [3.3](#). Passive infrared reflective markers were placed on key skeletal landmarks to minimize movement of the markers relative to the skeleton. Cartesian global marker positions were recorded at 200Hz. Markers were attached with hypoallergenic tape directly to the skin where possible (where clothing did not cover the markers) or on top of tight-fitting clothing to minimize marker movement.

All markers were labelled based on their attachment point on the body. [Table A.1](#) in [Appendix A](#) lists the marker labels, full names, and detailed attachment points.

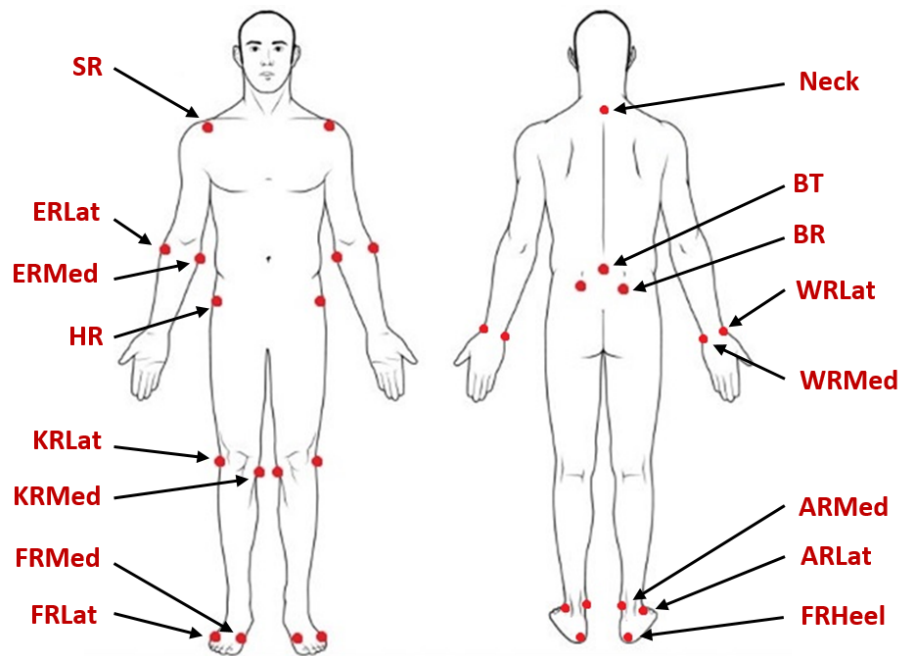


Figure (3.3) Diagram of the locations of 30 motion capture markers on the body, along with their labels.

### 3.1.6 Participant Recruitment

A total of 22 participants were recruited, 9 females and 13 males, between the ages of 19 and 34. The participants were primarily graduate students at the University of Waterloo. Four recruited participants were Certified [MovNat](#) Trainers or other non-certified practitioners of “natural movement” training, and were well practiced with jumping to a target. The remaining 18 participants had not practiced jumping to a target before this study.

Any participants with serious injuries in the previous 6 months were excluded from the study. Each participant filled out a demographic information and eligibility form before the data collection. This experiment was approved by the University of Waterloo Research Ethics Board, and informed consent was obtained from all participants.

## 3.2 Reasoning for Experiment Design

The experiment protocol provides a framework to analyze jumping to a target with respect to key motor control concepts. Three different target distances were used to capture

how motor control patterns would differ between performing short jumps (well within the physical ability of the jumper) or long jumps (close to the limit of the jumper’s ability).

Jumps to each target were separated into two sets to help observe a participant’s jumping improvement (due to motor learning), regardless of jump distance, over the course of the experiment. It was predicted that jumpers would have higher jumping success rates and more consistent motor control during the second set of jumps to each target compared to the first set.

Performing two jumping sets to three different targets results in 6 total sets of jumps. Movement variability analyses were used within each set of jumps to identify changes in kinematic data and motor control between different sets (analyzed further in section 5.2). The total experiment completion time was kept to a maximum of 60 minutes for each jumper (5 minutes for experiment setup, 10 minutes for warm-up, and 45 minutes for data collection). Based on experiment pilot studies it was deemed that a person of average physical ability could comfortably perform one jump per minute for 45 minutes, but more than this may be tiring. Therefore, a total of 36 jumps to a target (6 jumps per set), plus the 6 maximum distance jumps used for calibration (two sets of three jumps), were used for the protocol. Instead of performing the second set to each target immediately after the first, sets to each target distance were separated so that the jumper would perform one jumping set to each target distance before returning to perform the second set at each distance. The purpose of this separation of jumping sets was to more accurately capture motor learning effects at all three target distances, avoiding motor learning effects being seen at certain target distances more than others.

Finally, a second calibration distance was used to recalculate the target distances for the second set of jumps to each target (second half of the data collection) in case the participant had improved so much that the second set of jumps to each target, even the long target distance, were no longer difficult, resulting in very few examples of unsuccessful jumps.

### 3.3 Data Post Processing

A pose estimation method was used to transform the motion capture marker position data into joint trajectories for each jump recording [30]. This section describes the creation of a kinematic full body model, Extended Kalman Filter pose estimation for joint trajectory generation, validation of the pose estimation joint trajectories, and temporal alignment of the trajectories.

Before the pose was estimated, the raw motion capture data were cleaned. This process included manually joining segments of marker position trajectories where the markers were occluded, correcting any swapped or mislabelled markers, and processing all marker trajectories through a 6Hz low-pass filter.

Note that motion capture data from Participant ID 01 contained too many marker occlusions and mislabelling errors, and so only data from participant IDs 2 to 22 were used during post processing and data analysis.

### 3.3.1 Kinematic Model

A kinematic model was developed to approximate the human skeleton for pose estimation [2]. The model is formed with rigid links connected with prismatic and revolute joints, with a total of 15 links and 35 degrees of freedom. Sets of three orthogonal revolute joints represent the shoulders and hips. One prismatic joint was added to each shoulder joint, variable along the frontal axis of the body, to better approximate scapula movement. Figure 3.4 shows a labelled diagram of the links and frame/joint locations of the kinematic model. Table A.2 in Appendix A describes all joints in the kinematic model and their position in Figure 3.4.

In the “zero pose” (shown in Figure 3.4) the spine, upper arm, forearm, thigh and shin links have only a vertical offset component from their origin frame, while the spine2shldr, base2hip, and foot links have 3D offsets. All joints are at zero degrees in the zero pose. Table 3 lists all joints in the kinematic model and where they are located. The positive angle direction of each joint is in the same direction as the joint name (i.e. sagittal plane knee joint is named “knee.jExtension”, so increasing angles mean the leg is straightening and decreasing angles refer to the knee flexing).

The kinematic model link offsets were calculated for each participant based on the motion capture marker positions recorded during the calibration pose. The calibration window used for all kinematic model calculations was over one full second, from frames 251 to 450. This window was optimized to reduce the marker position error over all joint trajectory data. Elbow, wrist, knee and ankle joint centres were assumed to be located directly between markers placed on either side of these joints. The model base frame and hip joint centres were calculated based on [25], using the markers on the front (ASIS) and rear (PSIS) of the pelvis, and the leg length.

The shoulder joint centres of the model (glenohumeral joint) were assumed to be directly under each shoulder marker (under the acromion process) when in the zero pose, by a constant distance  $S2sc$  that was estimated to the nearest 5 mm during data collection.

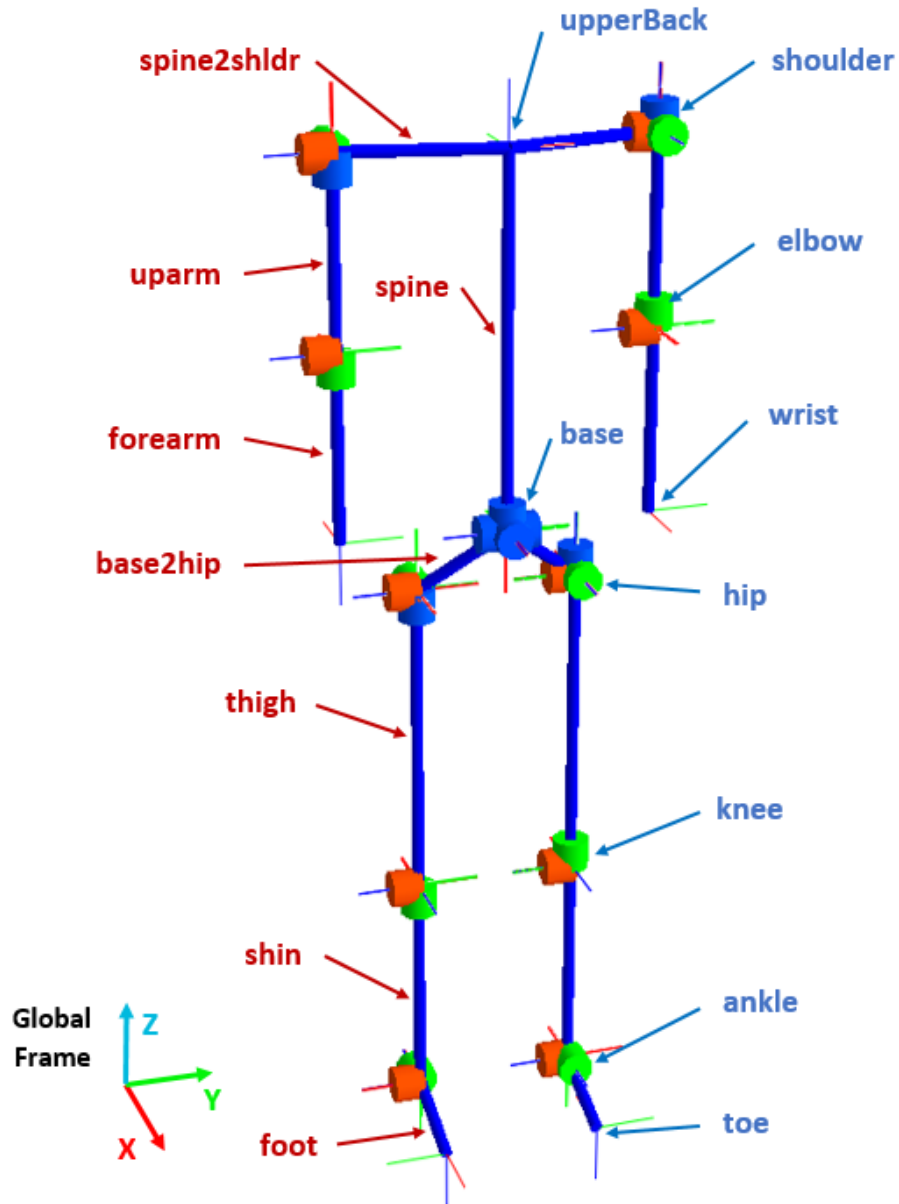


Figure (3.4) Kinematic model in the zero pose. Blue lines show rigid links, cylinders between the links represent revolute joints. Three orthogonal revolute joints model joints at the lower back, shoulders, and hips. The six world-to-base joints (three prismatic, three revolute) and the two prismatic shoulder joints are not shown.

This approximation of the shoulder joint centre resulted in lower marker mean absolute error (MAE) of the upper torso and arms than more complex optimization approaches for calculating the shoulder joint centre (discussed in detail below).

Model link dimensions were first calculated based on the calibration window of each jump recording, and then were averaged to form the final kinematic model used for all jumps performed by the participant.

Markers were then rigidly attached to the model at specific locations. Table A.1 in Appendix A includes the model links to which each marker was attached. Although the same model dimensions were used for all jumps performed by a participant (in order to consistently compare model joint angles from different jumps), the markers were attached to the model based on the calibration pose of each individual jump. This prevented small changes in marker position during data collection (due to clothing movement, sweat, marker reattachment, etc.) from affecting the accuracy of the joint angles calculated from pose estimation.

Two simplified models for the kinematic shoulder joint were compared. The first model consisted of three orthogonal Euler angles, representing the glenohumeral joint, a constant offset distance away from the “upperback” model frame. In the second model, a prismatic joint was added to the shoulder model, moving along the frontal axis of the body, to better approximate the motion of the scapula. To compare the modelling accuracy of the two models, the marker position MAE of the shoulder was calculated (validation of pose estimation results is described in detail in Section 3.4). The average shoulder marker MAE when using the first model was 14.8 mm on average, higher than all other body markers (overall average error of 8.1 mm), especially after the calibration pose when standing straight with arms down (up to 40 mm error). For the second shoulder model with a prismatic joint, the average MAE of the shoulder markers was 11.9 mm on average (improved by 2.9 mm), with peak improvements of up to 20 mm. The neck marker MAE improved by 2.1 mm on average, and the MAE of all other body markers had negligible difference. The improvement of the shoulder and neck marker MAE warranted the inclusion of the prismatic shoulder joint in the kinematic model.

Most previous analyses of human jumping used planar models of the body for simplification [42] [59]. Although the standing broad jump movement takes place predominantly in the sagittal plane, studies have shown that upper body motions generate significant power in directions outside the sagittal plane, predominantly from shoulder adduction/abduction [27]. Therefore, a 3D kinematic model was used.

### 3.3.2 Extended Kalman Filter Pose Estimation

The marker position data was input to an Extended Kalman Filter (EKF) for estimating the pose of the participant at each frame of the jump recording, using the joint angles, velocities and accelerations of the kinematic model as the state [30]. Section 2.2 introduces the Extended Kalman Filter as it relates to this work.

The primary metric of pose estimation accuracy was the mean absolute error (MAE) between the ground truth marker positions (from motion capture) and the estimated positions of the markers rigidly attached to the model (from EKF).<sup>1</sup>

$$MAE = \sum_i^N \sqrt{(x_i - x_{e,i})^2 + (y_i - y_{e,i})^2 + (z_i - z_{e,i})^2} \quad (3.1)$$

Where  $(x, y, z)_i$  is the true marker position (captured by the motion capture) and  $(x_e, y_e, z_e)_i$  is the estimated marker position (attached to the kinematic model) at the  $i_{th}$  index of the summation variable. The position errors can be summed over all frames, all markers, or combinations of both (see Section 3.4 for examples).

A constant acceleration model was used for the state update step. Observation noise was set to 0.01 (average marker MAE at or below 10 mm) and process noise was optimized to a value of 1.05 by minimizing the average MAE from all markers, over all jumps and participants.

The results of the pose estimation consist of the initial “world2base” transform, used to locate and orient the kinematic model in the starting position, and the joint trajectories for moving the kinematic model through the jumping action.

A simplified 14 DoF kinematic model was used for the IOC analysis (see Chapter 5), comprised of all joints in the full model that move the body in the sagittal plane. All inertial parameters between the 3D and planar models were identical. EKF pose estimation was repeated to derive the joint trajectories for the simplified planar model.

---

<sup>1</sup>The standard equation for MAE is the summation of the absolute value of the error between each set of points, while Equation 3.1, uses the Pythagorean theorem to calculate the absolute distance between the estimated and true marker positions in Euclidean space. The commonly-used root mean squared error (RMSE) puts more weight on higher error values (due to squaring the errors before summing them), whereas the MAE weights all errors equally in the summation.

### 3.3.3 EKF Parameter Optimization

The EKF parameters were optimized to result in the lowest average marker MAE over all jump recordings from all participants. First, the EKF update model was considered, with constant velocity and constant acceleration state update models being tested. The EKF pose estimation was run for all data over each of the update models, and the average difference in marker MAE was found to be negligible between these two filters. It was found, however, that during the most dynamic parts of the jumping motion the constant velocity model responded more slowly to the change in position. For this reason the constant acceleration update model was used for all further EKF data processing.

The observation noise of the EKF pose estimation was set to 0.01, since the average marker MAE is approximately 10 mm (see Section 3.4). The process noise was optimized relative to the observation noise by finding the value resulting in the lowest average marker MAE over all jump recordings from all participants. A process noise of 1.05 was found to result in the lowest average marker MAE. This optimization was computed using MATLAB's nonlinear, constrained minimizer function `fmincon`.

Finally, a calibration window was used to calculate the kinematic model link dimensions, and the initial positions of the markers relative to the kinematic model frames. This window is placed within the initial 4 second (800 frames) calibration section at the beginning of each jump recording, averaging over the participant's relatively static pose to get the most accurate and stable measurement. A grid search optimization was performed to find the starting frame and calibration window length that resulted in the lowest overall MAE for all jumps and participants. A window from frames 251 to 450 was found to have the lowest and most consistent marker MAE for all jumps from all participants, so the kinematic model link lengths and marker attachments were calculated using the marker position data within this window.

### 3.3.4 Temporal Data Alignment

After the EKF pose estimation the trajectory data were not temporally aligned, since each participant did not jump at exactly the same time during each jump relative to when the recording started. In order to more easily compare the trajectories, a temporal shifting algorithm was applied to the jump data. Trajectories were shifted relative to one another by integer frame values. The temporal alignment values can be applied to the joint trajectories, and the Cartesian marker position data.

The 12 jumps performed to each target distance were aligned to each other, since the



temporal variation between trajectories to the same target were negligible (even after slight differences in the target distances based on *CAL\_1* and *CAL\_2*, as described in Section 3.1). Jumps to different target distances varied too much to compare their trajectories directly, since flight times were significantly longer for farther jump distances, and jump technique sometimes changed for different target distances. The 12<sup>th</sup> jump (6<sup>th</sup> jump of the second set) to each target was used as the reference trajectory for the alignment algorithm, and the 11 other jumps to each target were shifted to match the reference trajectory.

First, the data frames where the participant left the ground (takeoff) and landed on the target platform were determined. Takeoff frames were identified as the first frame where the average speed of the medial foot markers was greater than 0.2 m/s just before takeoff. Landing frames were identified as the first frame after takeoff when the average medial foot marker speed was less than 0.2 m/s. These velocity thresholds were manually chosen based on the observed data. Then, a rough alignment was performed, directly aligning the landing frames of each group of 12 jumps to each target.

Aligning the landing frames only was not adequate to temporally align the trajectories because the jumper can change their leg position during the flight phase, and therefore choose when their foot contact occurs (see Chapter 4). Consequently, after rough alignment, the jumps were further aligned by minimizing the sum of absolute error between the shifted signals and reference signals for hip flexion, knee extension, and ankle dorsiflexion joints (right and left). The resulting shift values for each of these 6 joints were then averaged to get the final shift value, providing the best integer frame shift value to align the shifted and reference trajectories. Figure 3.5 shows a typical example of the final aligned trajectories.

Only the hip flexion, knee extension and ankle dorsiflexion joints were used to align the joint trajectories because the other joint trajectories were much more variable across several jumps, as seen in Figure 3.5.

Only temporal shifting of the entire trajectory was used to align the jumps. This simple method was found to align the trajectories quite well despite slight variations in flight time and sagittal asymmetries between jumps. The high frame rate of the motion capture data (200 Hz) enabled integer frame shift values to be accurate enough for temporal alignment, and avoided more complex alignment and data trajectory interpolation/warping. Also, more complex methods like dynamic time warping [33] would not preserve the relative kinematic and dynamic properties of the trajectory data.

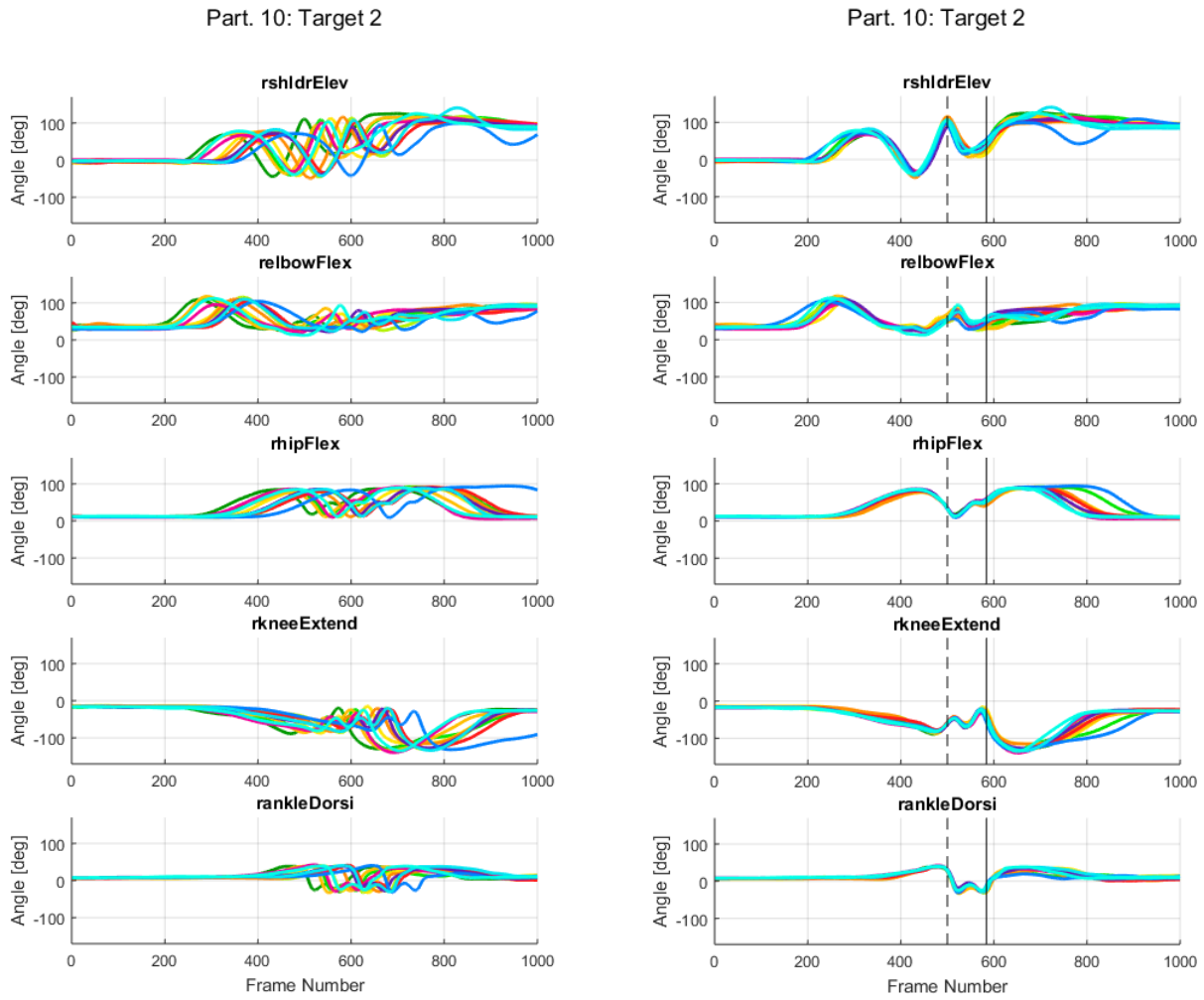


Figure (3.5) Five sample joint trajectories of 12 jumps to the same target distances, shown before (left) and after (right) temporal alignment.

## 3.4 Marker Mean Absolute Error Analysis

The primary metric for validating the pose estimation results was the marker position MAE. The MAE (Equation 3.1) was calculated for each marker, at each frame of a recorded jump, for all performed jumps and for all participants.

### 3.4.1 Full Body MAE for a Jump

Averaging the MAE over all markers gives the average full body marker error over the course of a single jump. Figure 3.6 shows a typical full body marker position MAE. The highest MAE occurs at the most dynamic portions of the jump: the middle of the takeoff phase (high momentum generation) and the moment of ground contact at landing (landing impact).

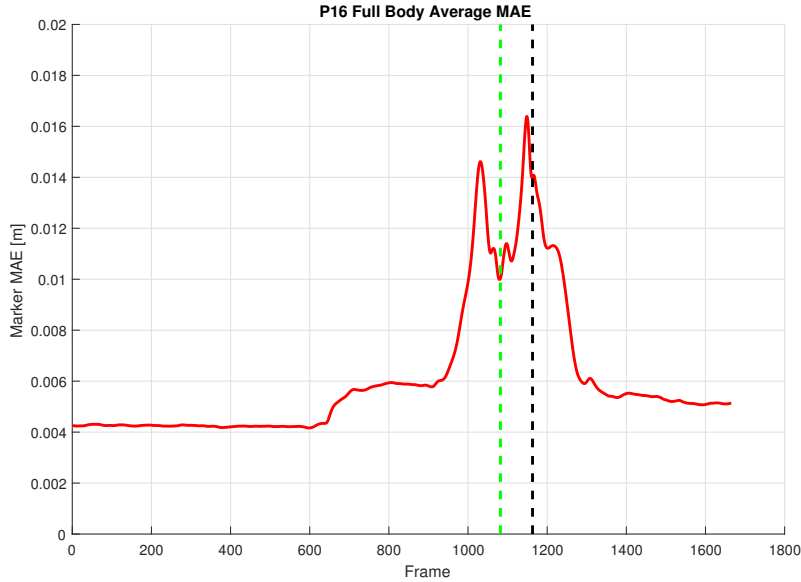


Figure (3.6) Representative example of MAE averaged over all body markers for a single jump. The green and black dashed lines mark the takeoff and landing frames, respectively.

### 3.4.2 Overall Average MAE for each Participant

For this analysis, the marker MAE values were averaged over all frames and all of a participant’s jumps, resulting in average MAE values for each marker (30 total) from each participant. Table A.3 in Appendix A shows these results, as well as the average MAE for all markers in the last column, and average MAE for each participant in the last row. Different participants have slightly different total average error, usually due to differences in technique or marker attachment conditions. The most notable difference occurred in the data of participant ID 09, since they circled their arms during flight phase

The lower body markers have the lowest average MAE, possibly due to a better approximation of the lower body kinematics with the model (mostly sagittal plane movement). The less accurate kinematic shoulder model results in higher average MAE in the shoulder and elbow markers. The fact that the hip and back markers were attached to the participant’s clothing rather than skin likely contributes to higher MAE for these markers, especially when participants flex their hips before takeoff.

### 3.4.3 Average Peak MAE for each Participant

For this analysis, the peak marker MAE values were found for each single jump, then these peak values were averaged over all jumps from one participant. Table A.4 in Appendix A contains the “average peak” MAE values. It is clear that the lower back markers often show the highest peak errors during a jump, likely due to the approximated hip joint centre model.

This chapter explained the design, execution, and reasoning for the experiment to collect kinematic data for jumping to a target. Pose estimation filtering was used to transform the experimental data into joint trajectories based on a full body kinematic model. The pose estimation results were tested based on the error between the simulated marker positions on the kinematic model and the ground truth motion capture experiment data.

The next chapter illustrates the analysis of the joint trajectory data and calculated features to determine how these data are related to the success of a jump to a target.

# Chapter 4

## Kinematic Trajectory Analysis

This chapter describes the kinematic analysis of the motion capture data and pose estimation trajectories discussed in the previous chapter. The purpose of this analysis was to identify trends in the trajectory data and calculated features that correlate to a successful jump, as well as other jump performance features and motor control concepts.

First, high-level observations of the participant jumping behavior during the experiment were noted. Then, the data were analyzed to identify correlations between the joint trajectories and jump success based on: individual joint trajectories, center of mass (CoM) position and velocity trajectories (based on a dynamic model specified by anthropometric data), and the timing of the jump phases.

The two features in the trajectory data that were found to be most influential to the success of the jump were CoM takeoff velocity and the pose of the body (and CoM position) when the feet contact the ground at landing. These influential features, as well as the full CoM trajectory, were analyzed with respect to movement variability, novice vs. expert technique, and motor learning.

### 4.1 Human Jumping Experiment Observations

In general, all participants could perform the jumping to a target task successfully at least some of the time. Table 4.1 shows that the majority of jumps were graded perfect, and relatively few jumps were not on target. As expected, relatively high jump success rates were observed for the short and medium target distances, while success rates for the longest target distance were much more variable among participants.

Table (4.1) Number of jumps in dataset in each jump grade category, for all participants.

Back (B)	Slightly Back (SB)	Perfect (P)	Perfect, with balance corrections (P*)	Slightly Forward (SF)	Forward (F)
16	64	461	135	48	32

Variations in technique were observed between participants, such as how low participants bent their legs during the takeoff phase, how low the legs collapsed upon landing, various methods of using the arms to generate momentum and regain balance through the jump, and the height of the torso and feet during the flight phase.

Participants with different levels of jumping experience were included in the study, and generally more motor learning and improvement in jump success was observed in those with less previous experience. On average participants performed better (higher jump success, higher control/stability during the motion, more consistent technique) during the second set of jumps at each target distance. Table A.5 in Appendix A lists the number of perfect jumps from each participant in each jumping set. The total number of jumps graded perfect from all participants was greater in the second set of jumps to each target.

## 4.2 Joint Trajectories

The individual joint trajectories of the kinematic model were compared between the jump sets performed by the same participant, and between sets from different participants. The joints that provide limb movement within the sagittal plane, and contribute most to generating forward and vertical momentum during the jump [42], were usually the most consistent trajectories. The primary joints contributing to this motion were: the lower back front-back joint, hip flexion, knee extension, ankle dorsiflexion, shoulder elevation, and elbow flexion. The trajectories of the hips, knees and ankles were less variable than the joints of the shoulders and elbows in both inter- and intra-participant comparisons. Figure 4.1 show example trajectories of these primary joints with both inter-participant (12 jump trajectories in each single graph) and intra-participant (between graphs) comparisons. Appendix B contains additional joint trajectory examples.

The kinematic data in the jumping trajectory figures in this chapter will be colour-coded based on the corresponding jump grading given to the jump during the experiment. This colour-coding makes correlations between jump trajectories/features and jump success easier to identify. The jump grades (as listed in Section 3.1) of back (B), slightly back (SB), perfect (P), perfect with balance corrections (P\*), slightly forward (SF), and forward

(F), have the colour-coding of blue, purple, green, green dashed, yellow, and red lines respectively. See Figure 4.2 for the colour coding legend.

Although the joint trajectories corresponding to off-target jumps sometimes show deviations from the normal trajectories due to mis-steps or lost balance, these off-target trajectories are usually within the range covered by all on-target jump trajectories. Repeatable correlations to the success of the jump were not found within these high-dimensional joint trajectory data.



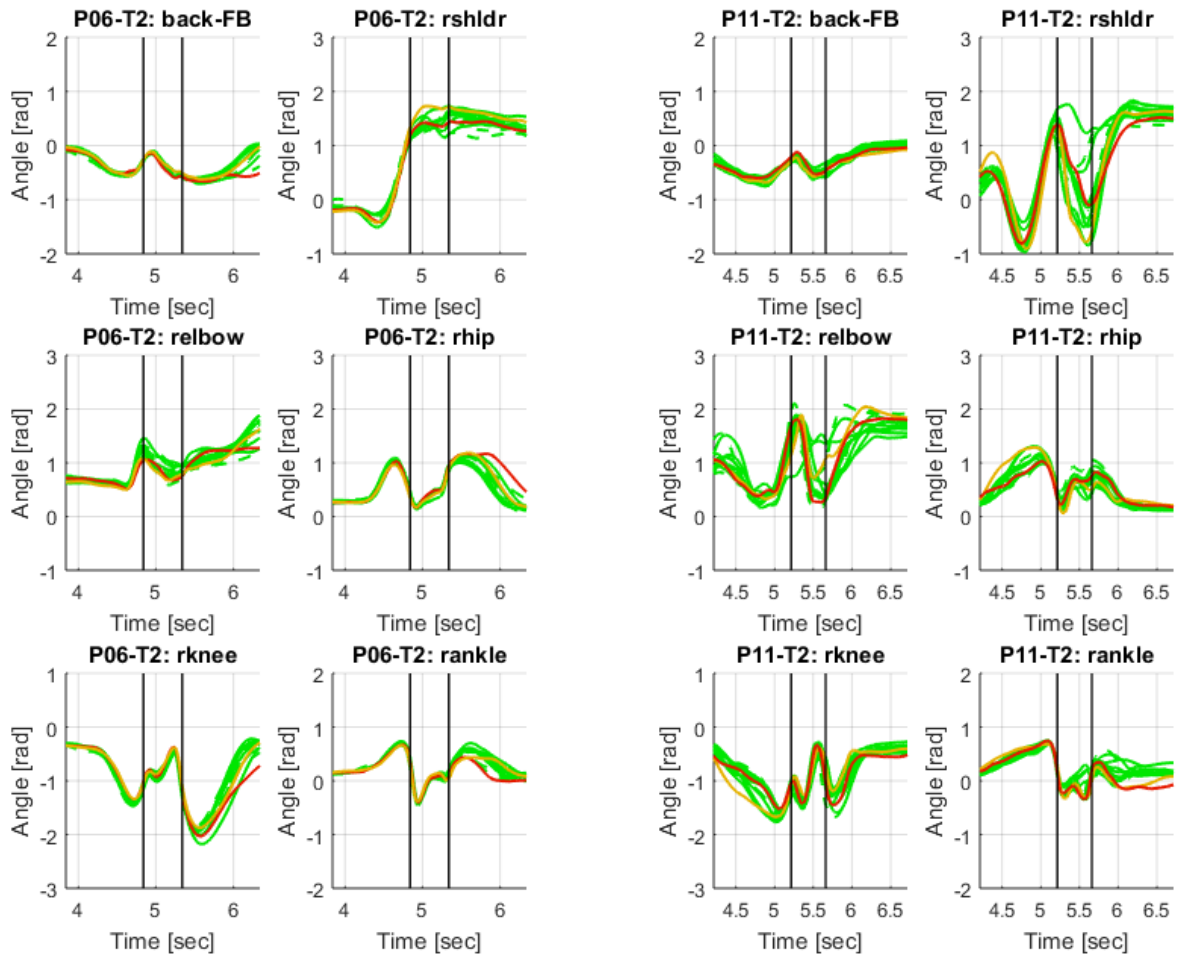


Figure (4.1) Examples of 12 jumps to a target from two participants (left and right), showing 6 joint trajectories. Jump grade colour-coding applies.






	<b>Back</b>	<b>(B)</b>
	<b>Slightly Back</b>	<b>(SB)</b>
	<b>Perfect</b>	<b>(P)</b>
	<b>Perfect, balance corrections</b>	<b>(P*)</b>
	<b>Slightly Forward</b>	<b>(SF)</b>
	<b>Forward</b>	<b>(F)</b>

Figure (4.2) Jump colour coding legend. All jumping data trajectory plots in this thesis use this colour coding.

### 4.3 Center of Mass Trajectories

Next, CoM position and velocity trajectories were calculated using the model joint angle trajectories and anthropometric inertial parameters [15]. The CoM was investigated because it is of prime importance when considering any airborne movements. From general projectile physics [20], only gravity acts on the centroidal momenta of a projectile during flight (assuming air resistance is negligible). This means that a jumper trying to land on a specified target must adjust their takeoff velocity appropriately before leaving the ground in order to intersect the desired target.

Figure 4.3 illustrates the computed CoM trajectories in the sagittal (global X-Z) plane for one set of 6 jumps. Jump grade colour-coding applies to the trajectories. The on-target (green) trajectories are most similar to each other, and the lowest part of the trajectories after landing are centered approximately at 0.4 meters in the global frame. The yellow trajectory (slightly forward) takes a longer path and lands farther forward than the perfect jump trajectories, while the purple trajectory (slightly back) shows a shorter path to the target.

For a jump to a desired target to be successful, the jumper must generate the appropriate forward and vertical linear momentum during the takeoff phase for their body to travel the correct distance to the target [50] [59]. For this reason the CoM takeoff velocity angle and magnitude must be synchronized to generate a ballistic trajectory to reach the desired landing location (detailed in section 4.3.1). The arms and legs have opposite angular momentum during the linear momentum generation of the body during takeoff, and these individual angular momenta counter each other so that the full body angular momentum during the flight phase is negligible and the jumper can land in the correct orientation [5].

During the flight phase the jumper cannot alter their linear momentum (CoM projectile trajectory) since they are not in contact with the environment and no external force can act on the body. The jumper can, however, adjust their body orientation during the flight phase with their arms, using them in a “reaction wheel” behavior in order to orient their legs between their CoM and the target prior to the landing, in preparation for absorbing their body’s linear momentum.

When the feet contact the ground at landing, the CoM must be positioned relative to the feet so the jumper can reduce their forward and downward linear momentum. Once the jumper comes to a static landing position, their CoM must be balanced over the support polygon provided by their feet [43]. If the foot is too far in front of the CoM during landing the jumper will fall backwards. Alternatively, if the feet are not placed forward enough, the jumper will not be able to fully stop their forward momentum and will fall forward.

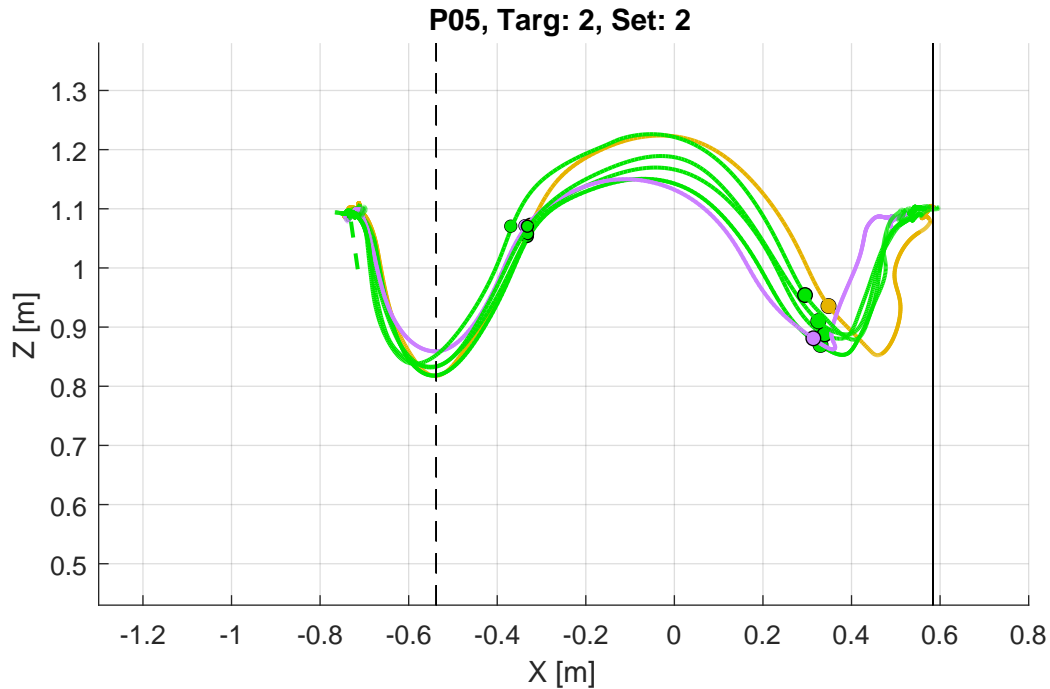


Figure (4.3) Example CoM trajectories for one set of 6 jumps. Vertical dashed and solid lines mark the position of the start line and landing targets, respectively. Jump grade is colour coded as shown in Figure 4.2.

The timing of when the foot contacts the ground, relative to the CoM location (detailed in Section 4.3.2), must be controlled for the jumper to successfully stick the landing of the jump.

### 4.3.1 CoM Takeoff Velocity

Takeoff velocity is defined as the velocity of the body's CoM at the moment the feet break contact with the ground at the end of the takeoff phase of a jump. Note that the term takeoff velocity will be used to describe the complete velocity vector of the CoM at takeoff, composed of both angle and magnitude.

To generate a CoM flight phase trajectory for reaching the target, there are an infinite number of possible CoM takeoff velocity angle and magnitude combinations. Figure 4.4 shows example ballistic trajectories to demonstrate this concept (assuming air negligible resistance).

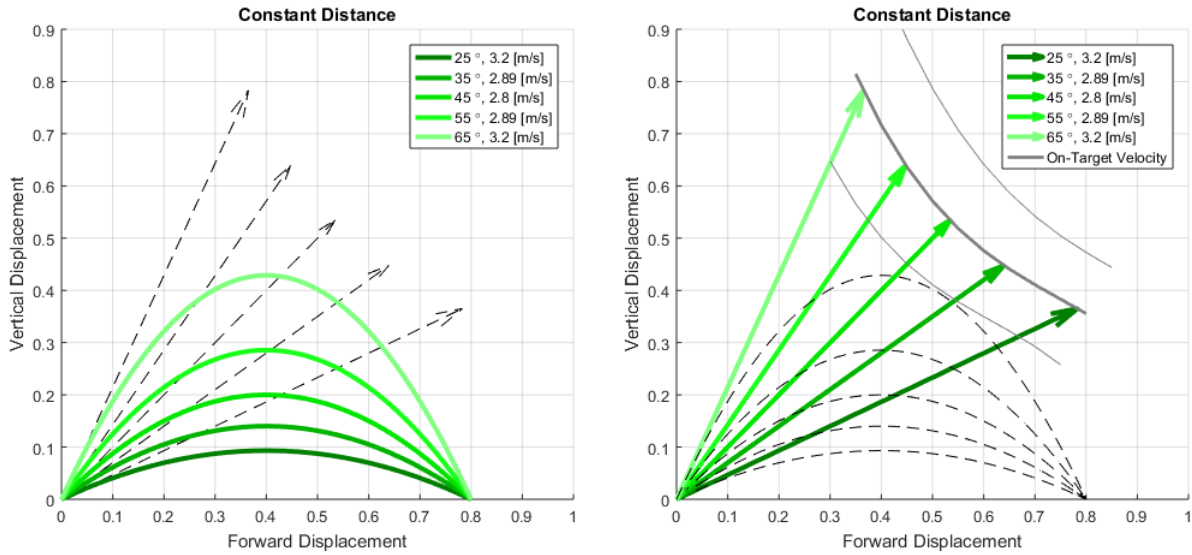


Figure (4.4) Projectile motion examples showing different takeoff velocity angle-magnitude combinations that land at the same location. Parabolic paths show the position trajectory of the projectile, while arrow vectors show the (scaled) takeoff velocity of each trajectory. The thick grey line identifies the velocity (relative to takeoff angle) required to reach the desired target distance of 0.8 meters. Thin grey lines show an on-target region corresponding to an example target area, within which any takeoff velocity vector will result in a trajectory that lands in the target area.

Based on the relationship between takeoff velocity angle and magnitude, an on-target zone (shown as grey lines in Figure 4.4) can be defined as the region in which the takeoff velocity vector must be located if the object is to land at a particular target location. The location of this on-target zone is placed relative to the distance the projectile must travel, and the width of the zone is relative to the width of the landing target in the forward direction.

Figure 4.5 shows an example set of velocity vectors with the on-target zone approximated based on the data. The jump grade colour-coding shows that the purple takeoff velocity resulted in a jump that landed slightly behind the desired target. The yellow takeoff velocity resulted in a jump landing slightly forward of the target. The remaining four jumps in the set were on-target, and were more closely clustered within the identified on-target zone.

This behavior is seen in the majority of the jumping experiment data; on-target jumps

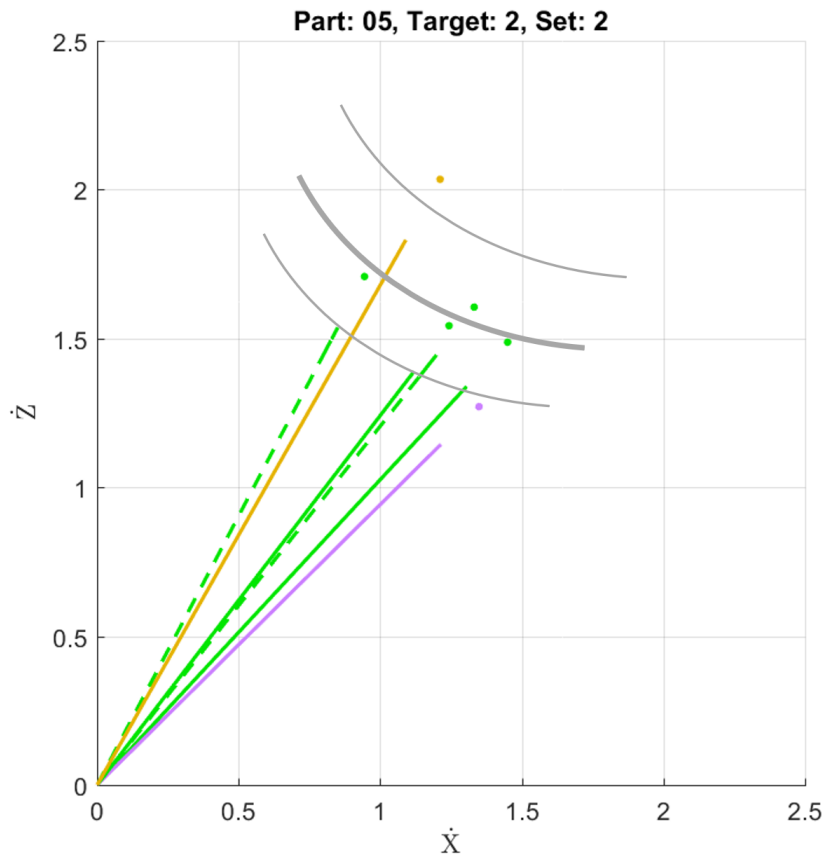


Figure (4.5) Example CoM takeoff velocity vectors for a set of 6 jumps. Solid grey lines mark the approximate on-target region, as described in the caption of Figure 4.4. Jump grade colour-coding applies.

generally have takeoff velocities clustered around a curved zone, and jumps that were behind, or farther than, the target have takeoff velocities shorter, or longer, than those in the on-target zone.

When this takeoff velocity trend did not hold in the data (either a jump was successful with a takeoff velocity outside the on-target zone, or a takeoff velocity inside the zone still resulted in an unsuccessful jump), it was usually due to the jumper's (in)appropriate control of their foot placement and leg stiffness during the landing phase, as discussed in the next sub-section.

### 4.3.2 Foot Placement Pose and Leg Stiffness

Foot placement pose is defined as the pose of the body (especially the extension of the legs) when the feet contact the ground upon landing. The body pose affects the position of the CoM. Leg stiffness is used to describe how much a jumper collapses their legs after the feet contact the ground upon landing. A jumper can control their foot placement pose, timing and leg stiffness just prior to and during the landing phase to result in higher success in jumping to a target.

Once foot contact is made upon landing the jumper must slow down the forward momentum of their body and come to a static position with the CoM balanced over the feet. The jumper aims to place their feet on the pre-determined target location, and cannot reposition their feet after contact is made with the ground. Therefore, the jumper must control when they place their feet by changing the pose of the body prior to contacting the ground, and control their leg stiffness while absorbing their impact, in order to appropriately slow down the body's forward momentum.

A jumper can change their leg extension before contacting the ground, landing with fully extended legs or partially collapsed legs (hips and knees flexed). Landing with extended legs will result in earlier ground contact and less distance travelled during the flight phase, while landing with collapsed legs will result in a later ground contact and further distance travelled. As shown in Figure 4.6, adjusting foot placement pose with leg extension prior to contacting the ground can be related to changing the elevation of the landing of a projectile, and consequently the distance travelled by the projectile.

#### Foot Placement Pose

When jumping to a target, the landing position of the feet is determined prior to the jump (i.e. on the desired target). If the jumper's takeoff velocity results in a trajectory that will not appropriately intersect the desired target, they can change their foot placement to recover from the inaccuracy of their initial takeoff velocity and still land on the target. If the trajectory is slightly short of the target, the jumper can collapse their legs while in the flight phase and use a later foot placement in order to travel the extra distance required to make it to the target. Alternatively, if the jumper's trajectory will send them over the target, they can try to extend their legs and contact the ground sooner to prevent their CoM travelling too far over the target and stop their forward momentum in time.

Figure 4.7 shows example CoM trajectories and their corresponding takeoff velocity vectors of four sets (six jumps each) performed by four different participants. The circles

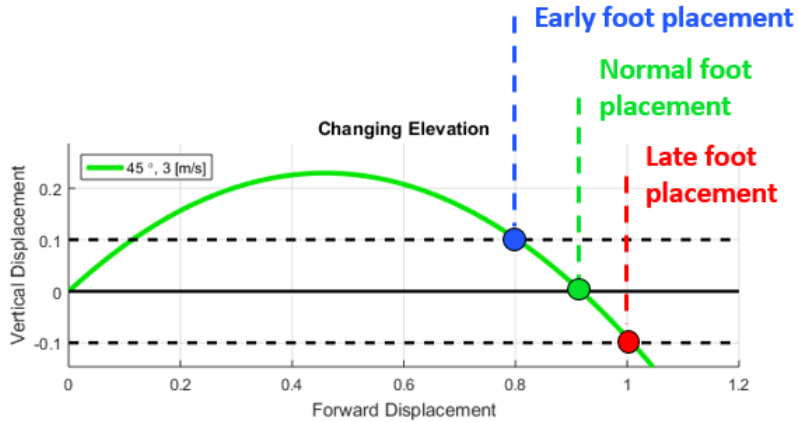


Figure (4.6) Projectile motion trajectory demonstrating the change in horizontal distance travelled relative to when the projectile contacts the ground. This change in elevation can be related to changing when a jumper contacts the ground at landing, controlled by their leg extension prior to landing.

intersecting the trajectory on the right side of the figure mark the position of the CoM in each trajectory when the feet touch the ground at landing. For all trajectories shown, the vertical position of the CoM at landing is quite variable. On the other hand, the horizontal distance between the CoM and landing target is clustered for all successful jumps, indicating an ideal horizontal position that the CoM should be located when the jumper makes contact with the ground. This ideal horizontal CoM position will be called  $X_{fp}$ , and is defined as the average horizontal CoM position of all successful jumps in a set.

The second set in the figure shows a trajectory that was slightly behind the target, and the foot placement occurred before the CoM reached  $X_{fp}$ , while the third set shows a trajectory landing slightly in front of the target, where foot placement occurred after the CoM passed  $X_{fp}$ . This clustering pattern of the foot placement horizontal location is observed in approximately 80% of CoM trajectories in the dataset.

Changes in foot placement pose can affect the distance travelled by the CoM enough that a jumper with a high degree of foot placement control is able to counter inaccuracies in their takeoff velocity in order to still land accurately on the target. This technique can provide more robust jumping control in different jumping environmental contexts, such as a change in desired landing position during the flight phase (due to landing conditions unseen at the start of the jump). Alternatively, poorly controlled foot placement can be the cause of failing a jump to a target. If a jumper's takeoff velocity is appropriate for



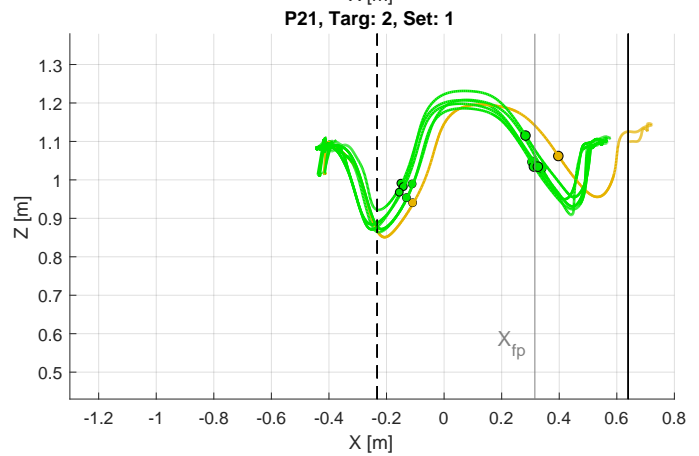
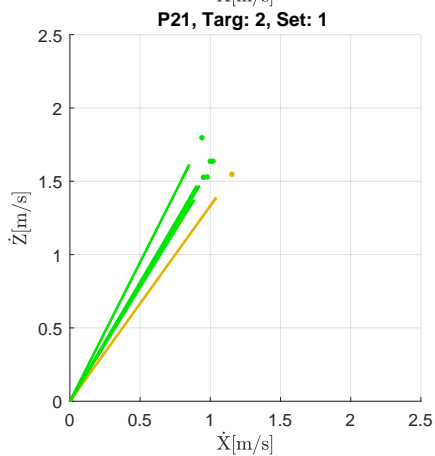
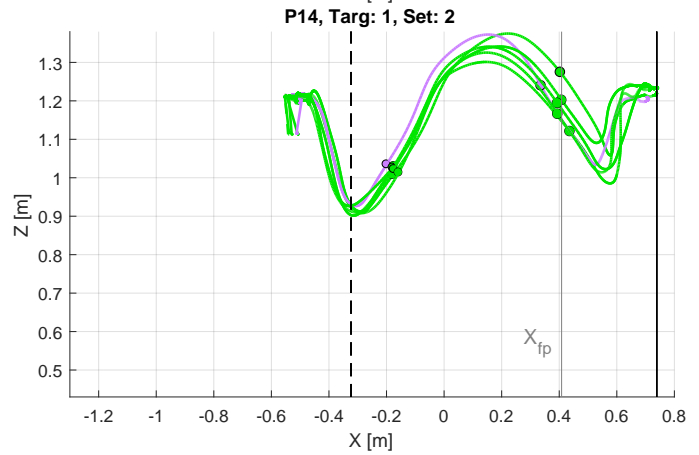
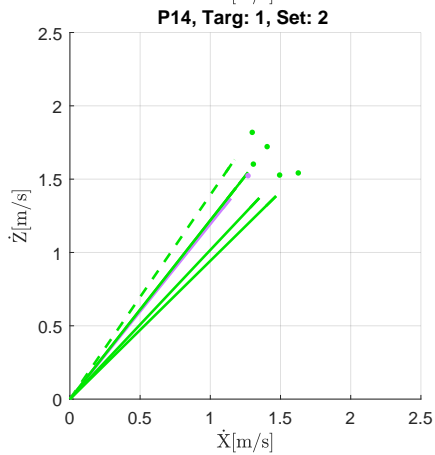
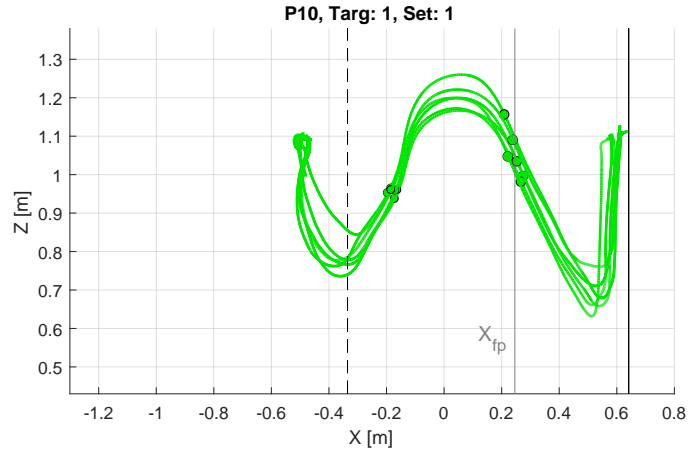
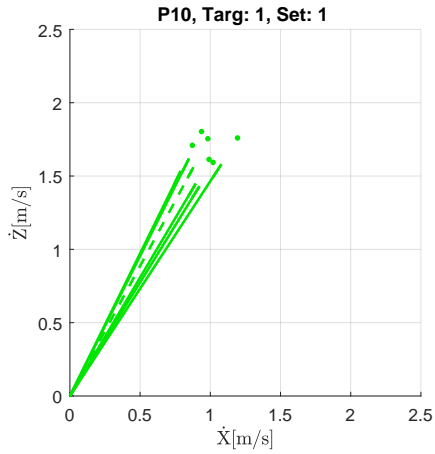
making an on-target jump, but their CoM position is not at  $X_{fp}$  when the feet contact the ground, a jumper's poor foot placement would result in jump failure. The last row of plots in Figure 4.7 shows two CoM trajectories (red and yellow) with foot placement occurring well after the average foot placement of the on-target trajectories (in green). Since the corresponding takeoff velocities of these two jumps (lower left plot) are within the range of the on-target jump velocities, the jumper's poor foot placement was likely the cause of overshooting the target.

### Leg Stiffness

Even after placing their feet on the ground, a jumper can affect how far forward their CoM travels by controlling their leg stiffness. Note that in this context, leg stiffness refers to the co-contraction of muscles around the hip, knee and ankle joints, which can control the mechanical impedance of the leg as well as the force produced by the foot on the ground [26]. Keeping the legs extended and stiff after foot contact causes a higher and faster impact, and quickly stops the forward momentum of the body. Alternatively, if the legs are allowed to collapse during landing, flexing at the hips and knees more, momentum absorption will occur over a longer period of time, and the CoM will travel farther forward during the landing phase.

If a jumper's foot placement pose is not ideal at the moment of ground contact, the CoM can still be guided to a static position over the jumper's support polygon at landing by controlling their leg stiffness after the feet touch the ground. Figure 4.8 shows an example jumping set by one of the expert jumpers, who demonstrated a large variability of leg stiffness, typically collapsing their legs much more than other participants.

As with foot placement, improper control of leg stiffness can also be the cause of an inaccurate jump. In the figure above, the purple CoM trajectory is very similar to the lowest green trajectory, and the foot placement is clustered with all other successful jumps. However, after foot contact was made the jumper's leg stiffness was high and slowed down their CoM forward velocity quicker than the similar green jump trajectory, and ended slightly short of the target.



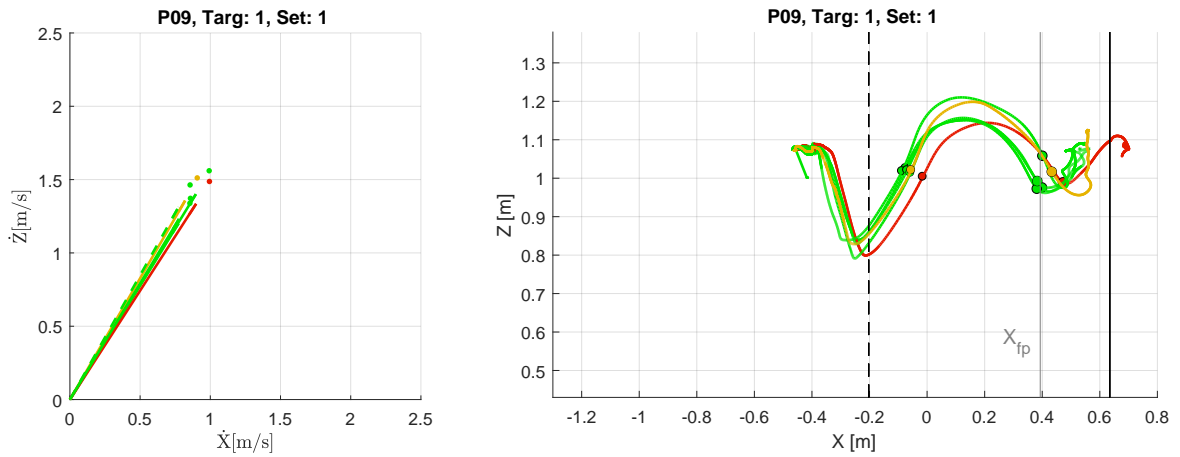


Figure (4.7) Four sets (6 jumps each) of takeoff velocities and corresponding CoM position trajectories. CoM trajectories behind, or forward of, the target distance exhibit early (legs extended), or late (legs partially collapsed), foot placement relative to on-target jumps. Average CoM forward position at landing is marked by the grey line at  $X_{fp}$ . Some trajectories (as shown in the last row) show poor foot placement timing that is likely the cause of failing a jump. Jump grade colour-coding applies.

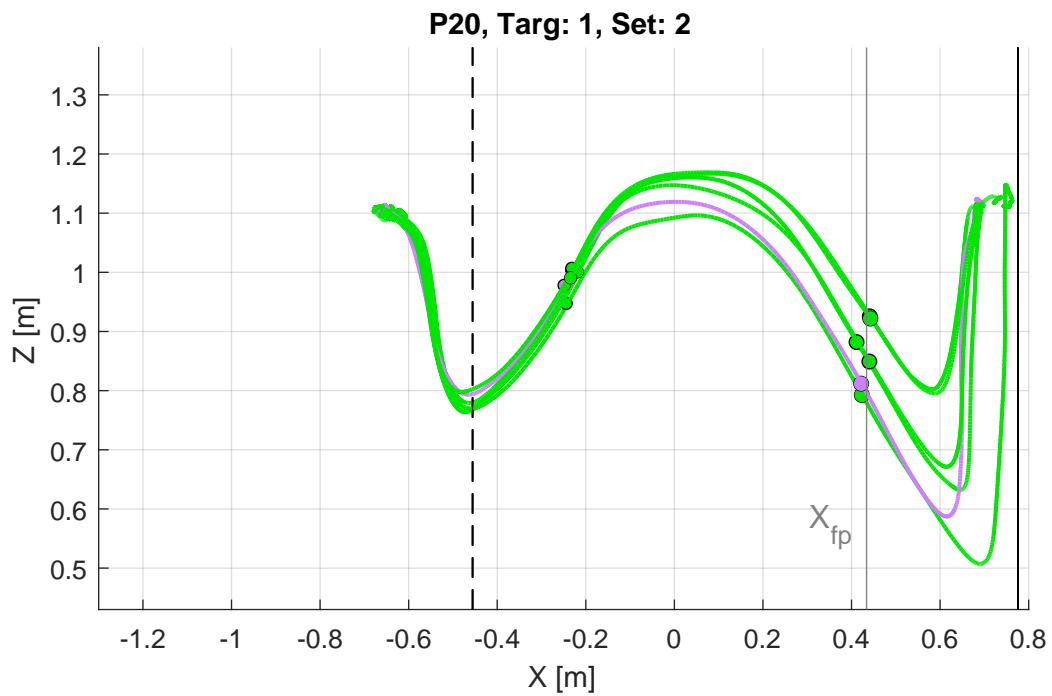


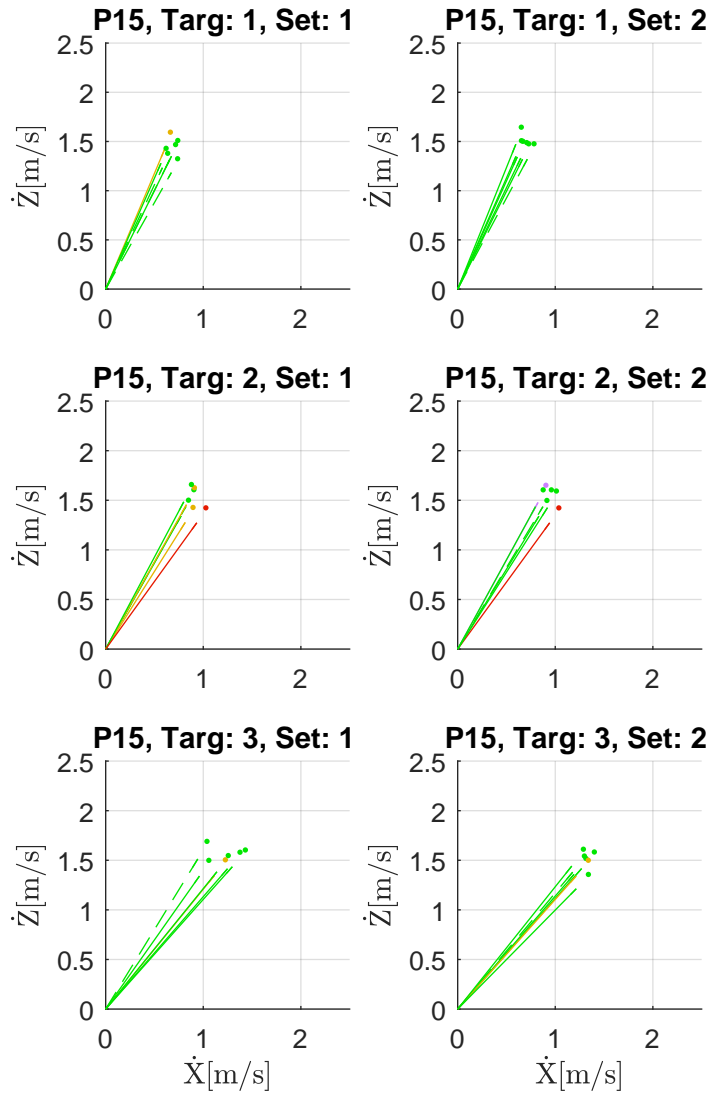
Figure (4.8) CoM trajectories of one jumping set exhibiting varying degrees of leg stiffness. Foot placement pose is tightly clustered, but CoM travels much lower to the ground on certain jumps. The purple trajectory shows foot placement close to other on-target jumps, but leg stiffness was higher than optimal and the CoM was stopped too soon and did not travel far forward enough to balance fully over the target. Jump grade colour-coding applies.

## 4.4 Motor Learning

By comparing the jump trajectory data between the first and second sets of jumps to each target, motor learning effects of the participant can be observed. Figure 4.8 shows all jumps from a sample participant during the experiment. Generally, participants had higher jumping success rates (landed on the target more often) in the second set of their jumps as compared to the first set.

Takeoff velocity was generally more consistent (in both angle and magnitude) in participants' second sets of jumps to each target, suggesting improved control for jumping a particular distance after multiple repetitions of the movement.

Changes in foot placement pose between the first and second sets of jumps were less consistent. Some participants had noticeably tighter clustering of their foot placement in their second jump set, as seen in Figure 4.9, suggesting these participants started controlling their foot placement more accurately the more they jumped. Most participants did not have a noticeable difference in foot placement clustering between their jump sets.



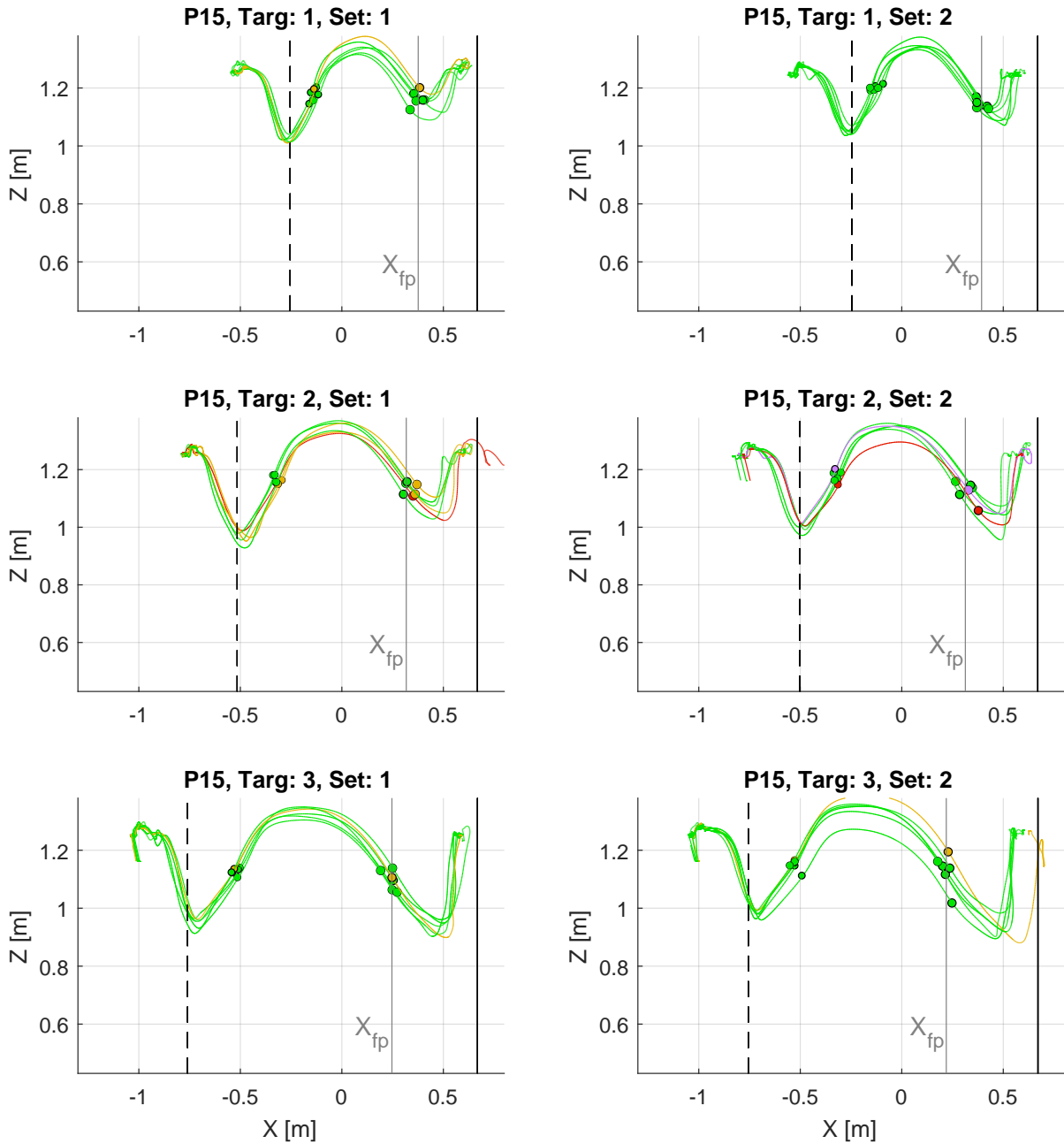


Figure (4.8) Example of all takeoff velocities (top) and CoM trajectories (bottom) performed by one participant for each set. In each graph, rows one, two and three correspond to jumps to the short, medium, and long target distances. The left column shows the first set of jumps to each target, and the right column shows the second set. Jump grade colour-coding applies.

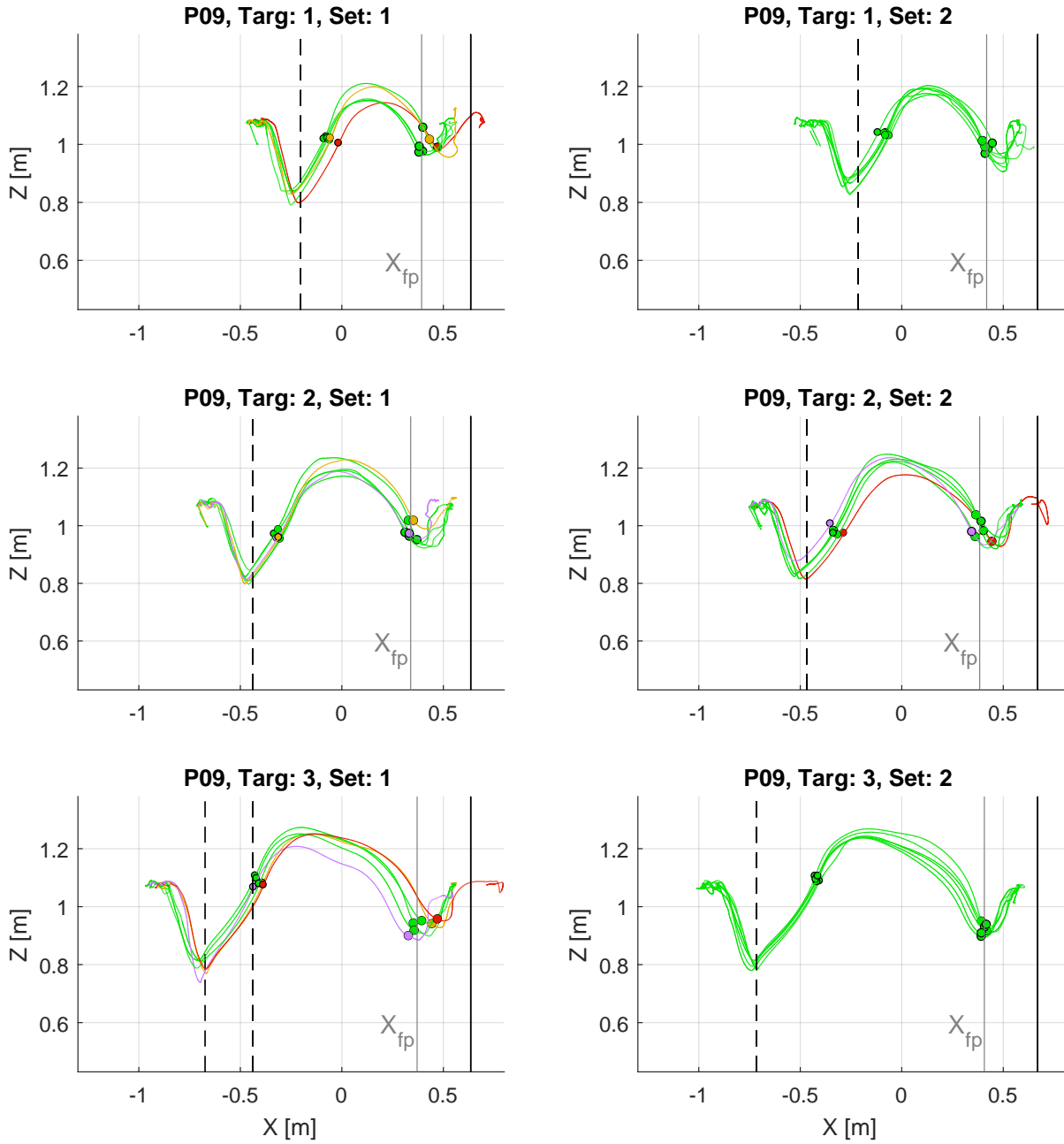


Figure (4.9) CoM trajectories from all jumps performed by an example participant. Foot placement pose clustering (circles on the right side of each plot, marking CoM position at landing) is seen to improve in the second set of jumps (right column) to each target, especially for the short and long targets (top and bottom rows, respectively).



## 4.5 Novice versus Expert Technique

The jumpers with the highest jump success rates during the experiment were considered experts. Specifically, jumpers with no more than one jump graded ‘B’ or ‘F’, and with no more than five jumps graded ‘SB’ or ‘SF’, thresholds chosen based on the jumping motion expertise of the experimenter. 8 of the total 21 participants in the experiment were labeled expert using these criteria. Two participants were labeled experts with exceptions to the criteria at the discretion of the experimenter: participant 2 had seven ‘SB’ and ‘SF’ jumps (greater than five), but had no ‘B’ or ‘F’ jumps and was the second farthest jumper, making for added difficulty Participant 12 had two ‘B’ jumps (greater than one), but all other jumps were perfect, resulting in one of the highest jump success rates.

The three jumpers who had previous experience in jumping to a target were all included in the experts category based on the experimental data (identified by ! in Table 4.2). The mean number of successful jumps from all expert participants was 27.4/36 (76%), while the novice participants had a mean of 17.8/36 (49%) successful jumps.

Expert jumpers generally controlled their foot placement pose and leg stiffness more effectively than novices. Even when some experts had less consistent takeoff velocities than novices, their overall jump success rate was higher because of their high level of foot placement control. This control allows expert jumpers to properly adapt their landing motions to counter inaccuracies in their takeoff velocity. Expert jumpers are more adaptable to varying jump conditions, hence their jumping success is more robust.

Expert jumpers were observed to have less motor learning effects than novice jumpers. Rather than improving their jump success throughout the study, experts started with a high success rate and maintained it throughout the experiment.

Participant Number	Number of Jumps for Each Grade						(N)ovice or (E)xpert	Jump Style	Exercise [hrs/week]
	B	SB	P	P*	SF	F			
2	0	2	22	7	5	0	E	C	2
3	0	4	10	12	5	5	N	-	3
4	0	2	16	7	3	8	N	C	6
5	0	4	14	12	5	1	N	B	0
6	0	0	20	9	5	2	N	B	4
7	0	4	29	3	0	0	E	D	1
8	0	3	22	11	0	0	E	A	3
9	0	3	19	8	3	3	N	D	6
10 !	1	0	32	3	0	0	E	A	8
11	1	2	18	5	4	6	N	A	6
12	2	0	32	2	0	0	E	D	9
13	2	8	19	5	0	2	N	-	2
14	1	6	15	10	4	0	N	A	5
15	0	1	20	8	5	2	N	D	0
16	1	3	26	3	3	0	N	B	7
17 !	1	4	29	2	0	0	E	C	15
18	1	1	21	8	4	1	N	D	0
19	1	7	21	6	0	1	N	-	6
20 !	0	2	30	4	0	0	E	C	20
21	4	6	21	3	1	1	N	B	7
22	1	2	25	7	1	0	E	A	3
Total	16	64	461	135	48	32			
Mean Expert	0.7	2.2	27.4	4.7	1.0	0.0			
Mean Novice	0.8	3.7	17.8	7.8	3.3	2.7			

Table (4.2) Participant statistics from jumping experiment. Green rows identify expert jumpers, as classified by their experimental jump success. Participants marked with a ! had self-proclaimed previous experience with jumping to a target.

## 4.6 Kinematic Trajectory Analysis Conclusion

This chapter analyzed the kinematic jumping trajectories found in Chapter 3. The take-off velocity of the CoM and foot placement pose at landing were identified as the most important features in the kinematic jumping data relative to jump success. The findings suggest that the goal of the human central nervous system is to guide the CoM into an acceptable ballistic trajectory range during the jumping motion, controlled by adjusting the CoM takeoff velocity. At landing, the feet must be placed on the target and the legs controlled to slow down the body's momentum and stabilize the CoM over the feet.

Expert jumpers were observed to have more consistent CoM takeoff velocity and better foot placement control. Novice jumpers did not start with a high degree of jumping movement control, but were observed to improve their takeoff velocity consistency for a given target distance after only a few jumps. Accurate and adaptable foot placement control appears to take more time and experience to develop. The next chapter describes how an inverse optimal control approach was used to extract the motor control tasks that are prioritized throughout the jumping trajectory.

# Chapter 5

## Inverse Optimal Control Analysis

In this chapter, an inverse optimal control (IOC) approach was used to determine the motor control tasks that jumpers prioritized throughout the jumping motion, based on the joint trajectories calculated from the pose estimation data processing. The motor control patterns of each jump were then compared to jump grading, target distance, jumper success rate and motor learning trends. These findings were then compared to those of the previous chapter.

IOC provides a powerful tool for human motion analysis; recovered optimal control tasks from several repeated motions can be used to identify a general motor control pattern for a given motion. For a given motion, control strategies used by different people can be compared to relate changes in the control tasks to specific changes in the performed motion. Human motor control objectives recovered via IOC can subsequently be applied for controlling humanoid robots to perform realistic motions by, identifying the optimality criteria for natural human motion, and then using these criteria to re-create motions on a new, non-biological system [45].

Section 2.3 provides a review of IOC concepts related to this research. Given an IOC cost function in the form of Equation 2.18, the first challenge is to identify the cost terms. These terms are formed by hypothesizing different motor control objectives that the central nervous system may be optimizing to perform a given human motion [8] [16]. This thesis uses a sliding window IOC solver (described in Section 2.3, using code developed by Lin *et al.* in [39]) to recover the relative weights of the individual cost terms in the IOC cost function. Those terms with the highest weights in each input trajectory window are assumed to correspond with the motor control tasks the human is optimizing during that window.

## 5.1 IOC Parameter Selection

The set of cost terms in the IOC cost function, the sliding window length and shift, the cost term normalization method, and optimization solver tolerances were first configured and tested on a representative subset of the jumping dataset. Table 5.1 lists the relevant parameters and their final values. The remainder of this section details the process used for choosing these values. The IOC parameter testing dataset was composed of 5% of the jumps in the full dataset, which were chosen to include a distribution of jump grades from both expert and novice participants that closely matched the distribution of the entire dataset.

Table (5.1) Full list of all parameters that were tuned for the IOC problem, and their final values.

Parameter Name	Value / Setting
Trajectory knot spacing	Every 5 frames
Sliding window length	41 frames
Sliding window shift	10 frames
Cost term normalization	Normalize over flight phase
IOC tolerance	10e-12
DOC tolerance	10e-4
Cost Term Set	See Table 5.2

Tuning the IOC parameters consisted of two stages. First, an initial set of parameters was used with the IOC solver to recover the cost term weight trajectories and record the residual norm error trajectory (see Background section 2.3 for details). The residual norm was only compared between multiple IOC solutions of the same input trajectory, and was affected by the set of cost terms, sliding window settings, and cost term normalization method. The set of parameters that resulted in the lowest residual norm was selected.

Second, the full cost function with recovered weight trajectories was used with direct optimal control (DOC) to generate a trajectory. DOC was used to validate the IOC solution by calculating the root mean squared error (RMSE) between the original input joint trajectories and generated DOC joint trajectories. The accuracy of the DOC reconstructed trajectories is affected by the IOC and DOC solver tolerance parameters, as well as the cost term set used. The tolerances and cost term set resulting in the lowest RMSE were considered the best parameters for the DOC validation, as detailed below.

### 5.1.1 IOC Cost Function Design

Human motor control tasks were hypothesized to form the cost terms in the IOC cost function (see Section 2.3). First, control tasks specific to the jumping motion were hypothesized, including task space position, velocity and acceleration of the CoM and toe positions of the body, relative to the global frame (with the origin located at the target position) and each other (Ex: velocity of CoM relative to velocity of the toes). The CoM and toe trajectories, and their relative positions to the target, were selected as the jumping-specific cost terms based on the findings of the kinematic trajectory analysis detailed in Section 4.

Second, control tasks that have been previously identified as relevant for human motion [8] were hypothesized, including the acceleration and jerk of the joints, joint torques and their derivatives, and kinetic energy and power of the system.

Finally, the functions for joint acceleration and jerk, joint torques and their derivatives, and joint power were split into separate cost terms for the arms (shoulders and elbows), legs (hips, knees and ankles), and torso (pelvis and lower back rotation). These sections of the body move with different velocities and have different roles in the jumping motion: the arms move fast, contribute moderate momentum generation and help landing stability; the legs move with moderate speed and are the primary contributor to momentum generation and landing impact absorption; and the torso moves slowly and is the anchor for the arms and legs [42]. The differing velocities and contributions of body limbs throughout the jump phases warrant separate cost functions [18]. Kinetic energy was not separated since this value includes the energy the entire body has when travelling through the air during the flight phase.

The cost terms in the IOC cost function must be independent to prevent singularities during the inverse KKT solver matrix calculations [39]. All jumping-specific cost terms in the task space were divided into forward horizontal (global X axis) and vertical (global Z axis) directions to avoid dependency between different cost terms. The separation of cost terms into single dimensions also provides more detailed insight into what the jumper is optimizing for (i.e. controlling vertical position but not horizontal position of the toe at a certain time in the jump trajectory).

In total, 40 different cost terms were hypothesized, seen in Table A.6 in Appendix A. Various cost term sets were used for performing IOC on the testing dataset. Terms with a recovered weight trajectory of approximately zero for the entire jump (across all windows) are assumed to have negligible relevance for that particular jump trajectory. Terms with zero weight do not have any effect on the relative recovered weights of the non-zero cost terms, but their inclusion drastically slows down IOC computation time, and were therefore removed from the final set of cost terms.

The set of cost terms was chosen first to minimize the KKT residual norm (highest priority), and then the RMSE between the input and DOC reconstructed trajectories (secondary priority) of the testing dataset. The final cost function included 17 cost terms, listed in Table 5.2. Cost term weight symbols will be used through the remainder of this chapter to refer to the IOC results.

Note that cost term 6 listed in Table 5.2 is the difference in forward velocity between the CoM and the toe. This term provided a lower KKT residual error than CoM forward velocity alone (relative to the global frame).

Table (5.2) The final set of IOC cost terms, summed over  $n_a$  DoFs or  $n_b$  bodies, and  $T$  time (where  $T$  is the length of each window for which IOC is performed).  $M$  denotes the inertia matrix,  $m$  denotes the mass of a single link in the kinematic model,  $c$  denotes the Cartesian position of the CoM. Sections of the body encompass the following joints: arms (shoulders, elbows), legs (hips, knees, ankles), and torso (lower back, pelvis).

	Cost Weight Symbol	Cost Term Equation	Description
1	$w_{KE}$	$J_{KE} = \sum_a^{n_a} \sum_t^T \dot{q}_{a,t}^T M(q) \dot{q}_{a,t}$	kinetic energy of model
2	$w_{CoM-Z}$	$J_{CoM-Z} = \sum_b^{n_b} \sum_t^T m_b c_{Z,b,t}$	CoM height
3	$w_{CoM-dZ}$	$J_{CoM-dZ} = \sum_b^{n_b} \sum_t^T (m_b \dot{c}_{Z,b,t})^2$	CoM vertical velocity
4	$w_{Toe-dZ}$	$J_{Toe-dZ} = \sum_t^T \dot{x}_{Toes-Z,t}^2$	Toe vertical velocity
5	$w_{Toe-dX}$	$J_{Toe-dX} = \sum_t^T \dot{x}_{Toes-X,t}^2$	Toe forward velocity
6	$w_{CoMToe-dX}$	$J_{CoMToe-dX} = \sum_b^{n_b} \sum_t^T (m_b \dot{c}_{X,b,t})^2 - J_{Toe-dX}$	CoM forward velocity relative to Toe
7	$w_{ddq-tor}$	$J_{ddq-tor} = \sum_a^{n_{a,tor}} \sum_t^T \ddot{q}_{a,t}^2$	torso: joint acceleration
8	$w_{dddq-tor}$	$J_{dddq-tor} = \sum_a^{n_{a,tor}} \sum_t^T \dddot{q}_{a,t}^2$	torso: joint jerk
9	$w_{\tau-tor}$	$J_{\tau-tor} = \sum_a^{n_{a,tor}} \sum_t^T \tau_{a,t}^2$	torso: joint torque
10	$w_{dq\tau-tor}$	$J_{dq\tau-tor} = \sum_a^{n_{a,tor}} \sum_t^T (\dot{q}_{a,t} \tau_{a,t})^2$	torso: joint angular power
11	$w_{ddq-arm}$	$J_{ddq-arm} = \sum_a^{n_{a,arm}} \sum_t^T \ddot{q}_{a,t}^2$	arms: joint acceleration
12	$w_{dddq-arm}$	$J_{dddq-arm} = \sum_a^{n_{a,arm}} \sum_t^T \dddot{q}_{a,t}^2$	arms: joint jerk



	Cost Weight Symbol	Cost Term Equation	Description
13	$w_{\tau-arm}$	$J_{\tau-arm} = \sum_a^{n_{a,arm}} \sum_t^T \tau_{a,t}^2$	arms: joint torque
14	$w_{dq\tau-arm}$	$J_{dq\tau-arm} = \sum_a^{n_{a,arm}} \sum_t^T (\dot{q}_{a,t} \tau_{a,t})^2$	arms: joint angular power
15	$w_{ddq-leg}$	$J_{ddq-leg} = \sum_a^{n_{a,leg}} \sum_t^T \ddot{q}_{a,t}^2$	legs: joint acceleration
16	$w_{dddq-leg}$	$J_{dddq-leg} = \sum_a^{n_{a,leg}} \sum_t^T \dddot{q}_{a,t}^2$	legs: joint jerk
17	$w_{\tau-leg}$	$J_{\tau-leg} = \sum_a^{n_{a,leg}} \sum_t^T \tau_{a,t}^2$	legs: joint torque

### 5.1.2 Trajectory Knot Setting

The next tuned parameter was the frequency of adjustable knots constraining the splines that formed the reconstructed joint angle trajectories. The IOC/DOC framework uses discrete differentiation to calculate the velocity and acceleration of the input and reconstructed trajectories. A minimum of three consecutive frames is required to compute acceleration. A knot spacing of five frames was chosen (rather than three) for smoother trajectory differentiation and spline fitting of the reconstructed trajectories. For the 200Hz motion capture data, this corresponds to 40 knots per second of motion.

### 5.1.3 Sliding Window Settings

Parameters for the sliding window IOC approach included the length of the window and the number of frames by which the window shifts. Each window was aligned for consistent spacing around the trajectory knots, so that the start, middle, and end frames of the window corresponded to knot positions which were constrained to the input trajectory. At least one knot was needed between each set of constraining knots to enable the DOC solver to adjust the reconstructed spline trajectory. Therefore, the window length must be equal to  $2kN_{KnotSpacing} + 1$ , with  $k$  being an integer greater than 1. Using a knot spacing of 5, the window length can be 21, 31, 41, ... frames long.

The window shift was set as a multiple of the knot spacing so that the constrained points

of each subsequent window (first, middle, last) would remain aligned with the constraining knots of the trajectory. This window shift also ensured that each frame would have the same number of overlapping windows after IOC was completed over the entire trajectory.

As window length is increased, more trajectory data is used to recover the cost term weights over the window, and the reconstructed trajectory of the window is more reflective of the full trajectory. However, if the window length is too long it may overlap different phases of the movement trajectory, violating the assumption of constant cost term weights. Therefore, the window length must be large enough to contain adequate kinematic and dynamic movement data to accurately recover the weights within the window, but still small enough to recognize distinct phases of the movement as optimized control tasks change. The flight phase of jumps to the short target distance had a minimum time of 0.31 seconds, or 62 frames. A window length of 41 frames (just over 0.2 seconds and containing 9 knots) provided enough movement data to have a smooth trajectory (not erratic changes) and short enough to be contained within the shortest flight phase of a jump.

The window shift value affects how many windows overlap each trajectory frame. A high window shift results in fewer recovered weights to average at each frame (allowing more drastic shifts in the averaged weight trajectory), while a lower window shift provides more overlapping windows and a smoother average weight trajectory. Additionally, a lower window shift means more windows are required to cover the entire input trajectory, and more computation time is required. A window shift of 10 frames (every two knots) provided enough resolution to visually distinguish when the weights changed, and a smooth averaged weight trajectory. A window shift of 10 frames with a window 41 frames long also guarantees that a minimum of two adjacent windows will be fully contained within the flight phase of each jump (minimum 62 frames).

#### 5.1.4 Normalization of Cost Terms

Most of the cost terms have differing units and scales of magnitude (i.e. position [m], velocity [m/s], angle [rad], angular velocity [rad/s], torque [N\*m]). The cost term magnitudes must be scaled before comparing their relative importance through the recovered cost term weights.

The cost term values were calculated over a portion of the entire input trajectory before performing IOC, and then their magnitudes were compared to compute relative scaling values for each cost term. Different portions of the input trajectory were used to compare the results. It was found that calculating the cost term scaling factors over the

flight phase of the jump best differentiates between the relative contributions of the cost terms throughout the entire jumping motion.

Normalizing over the entire trajectory, the takeoff phase only, or the landing phase only was also investigated. In these cases the recovered IOC weight trajectories were typically dominated by a single cost term, with most or all other terms providing a negligible contribution. This result suggests that normalization over the initial calibration motions and/or ground contact phases do not provide appropriate trajectory data to recover the weights during the flight phase, the most dynamic portion of the jump.

### 5.1.5 IOC and DOC Tolerances

The final parameters were the IOC and DOC solver optimization tolerance values. Both the IOC and DOC calculations were performed using iterative optimization solvers computing numerical gradients. The tolerance parameters governed the minimum threshold of the numerical gradient that the solver must attain to terminate and arrive at the final solution. Smaller tolerances resulted in reconstructed DOC trajectories with lower RMSE compared to the input trajectory, however, required a longer computation time for the optimizer to reach the required tolerance. Tolerances were adjusted by orders of magnitude, since adjustments finer than this did not have a great effect on the optimization results.

The recovered IOC weights settled to different solutions for tolerances between  $10e-3$  and  $10e-6$ , which affected the corresponding DOC reconstruction accuracy. Recovered weights were observed to be constant at all tolerances smaller than  $10e-6$ . The difference in computation time between various IOC tolerances was negligible compared to the DOC computation time, so a very small IOC tolerance of  $10e-12$  was used.

DOC tolerance adjustment has a much larger influence on computation time than does IOC tolerance. The reconstructed DOC trajectories became more accurate for tolerances between  $10e-3$  and  $10e-6$ , and tolerances smaller than  $10e-6$  resulted in approximately the same RMSE. Table 5.3 lists the approximate computation time required for a single sample jumping trajectory using the computing resources available for the project, including an i7-7700 CPU at 3.6 GHz with 32 GB of RAM. A DOC tolerance of  $10e-4$  was selected.

Using the 14 DoF kinematic model (as described in Section 3.3.2), the IOC solver took approximately 45 minutes to process a single jump trajectory of 500 frames. For the same trajectory, the DOC reconstruction code took approximately 18 hours for with a tolerance of  $10e-4$ .

Multiple DOC solver executions were performed for each of the jumps in the data subset used for parameter tuning. Once the final solver parameters were chosen the IOC weight

Table (5.3) Example computation times for an input trajectory 500 frames long, using the 14 DoF jumping model. Accumulated computation time for IOC was approximately 0.75 hours, while DOC took the remainder of the listed time.

IOC Tolerance	DOC Tolerance	Computation Time [hours]
10e-12	10e-3	12
10e-12	10e-4	20
10e-12	10e-5	36
10e-12	10e-6	72+

trajectories in the testing dataset were validated using the DOC reconstructed trajectory. Only IOC was run on the full dataset.

## 5.2 IOC Cost Term Weight Trajectory

Once the parameters were finalized, all jump trajectories in the dataset were run through the sliding window IOC solver. Approximately half of each original jump recording consisted of calibration motions, which were cropped out of the joint trajectories before completing the IOC analysis. Based on preliminary IOC testing, recordings were cropped from 60 frames before takeoff to 120 frames after takeoff. An example cost weight trajectory is shown in Figure 5.1.

The cost term weight trajectories of all jumps contained common patterns, with the plot in Figure 5.1 being a representative example. The most common patterns are: higher  $w_{CoM-Z}$  and  $w_{CoMToe-dX}$  during takeoff; mostly  $w_{Toe-dX}$  during flight with  $w_{Toe-dZ}$  and/or  $w_{KE}$  just prior to landing; high  $w_{CoM-Z}$ , and sometimes a  $w_{KE}$  peak, after landing.

These weight trajectory patterns suggest an underlying motor control structure for jumping to a target used by all participants and all target distances observed in the experiment. To investigate these patterns further, the weight trajectory mean and standard deviation of multiple sets of jumping motion data were calculated and compared. First, the mean and standard deviation of all jumps was computed to see the average motor control structure for jumping to a target, seen in Figure 5.2. This is the only time in this thesis where jump trajectories to different target distances are averaged together.

The overall mean weight trajectories are consistent with the observed patterns seen in weight trajectory plots of individual jumps.  $w_{CoM-Z}$  and  $w_{CoMToe-dX}$  are most influential during takeoff,  $w_{Toe-dX}$  dominates during the flight phase,  $w_{Toe-dZ}$  and/or  $w_{KE}$  are larger just before and at landing, and  $w_{CoM-Z}$  again rises throughout the landing phase. Note

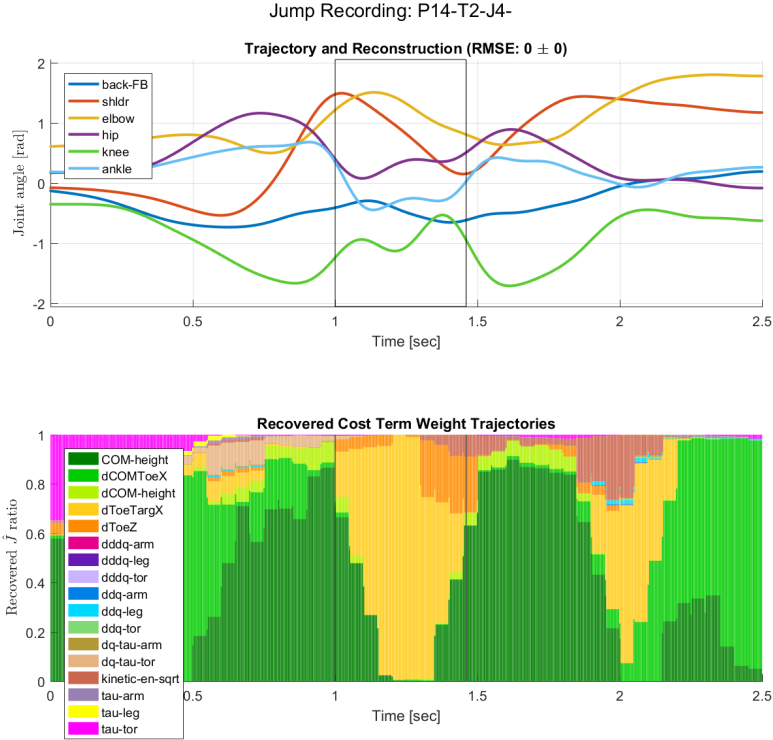


Figure (5.1) Top: Example joint trajectories for a jump to a target. Only six of the total 14 DoFs are shown. Bottom: Corresponding recovered IOC weight trajectories for the jump. Each frame consists of normalized recovered cost term weights, identifying the prioritized motor control tasks of the jumper throughout the movement. Takeoff and landing frames are marked with vertical black lines at 1.0 and 1.45 seconds, respectively.

that in all mean weight trajectory plots shown in this text, only the cost terms with a peak in their mean trajectory greater than 5% are shown.

Comparing the mean and standard deviation of weight trajectories between specific sets of jumps provides insight into the motor control differences due to changes in jumping parameters and characteristics. Figure 5.3 compares the mean weight trajectories between the three target distances, for all jumps performed by all participants.

The most obvious difference between the mean trajectories is a shift of the landing weights further in time, due to the increased flight time required for longer target distances. There is also an observed trade-off between  $w_{CoM-Z}$  and  $w_{CoMToe-dX}$ : for the shortest

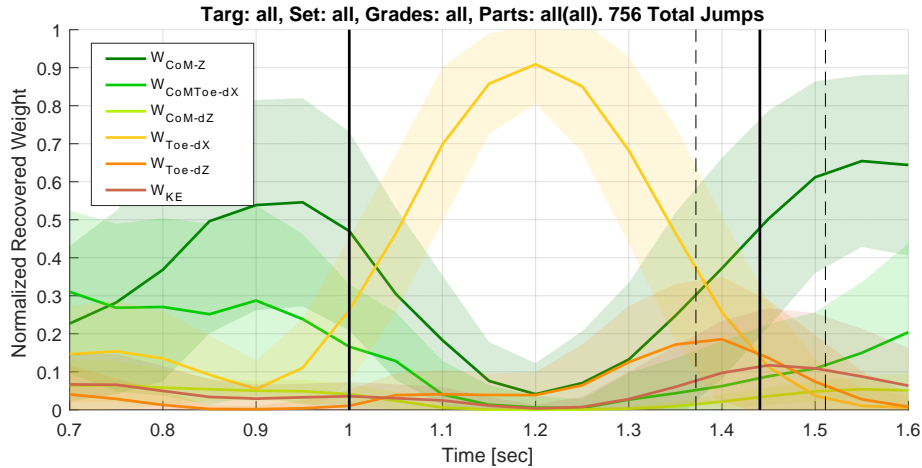


Figure (5.2) Mean and standard deviation of all cost term weight trajectories in the dataset. Trajectories are temporally aligned to the takeoff frame (solid black line, left). Average landing frame (solid black line, right) with 90% confidence intervals (dashed black lines) are shown for the landing frames of all jumps.

target,  $w_{CoM-Z}$  is higher before takeoff, and as the target distance is increased  $w_{CoMToe-dX}$  becomes greater during the takeoff phase. Finally,  $w_{KE}$  is higher for longer jumps, probably the result of generating more CoM momentum to reach the longer distance target, and consequently having to absorb more impact at landing.

The tradeoff between  $w_{CoM-Z}$  and  $w_{CoMToe-dX}$  suggests that jumpers use a higher arcing trajectory for shorter jump distances, and a trajectory lower to the ground for longer jump distances. This behavior is seen in the majority of the CoM takeoff velocity vectors computed in the kinematic trajectory analysis. A jumper's takeoff velocities for jumps to the short target distance typically have higher takeoff angles, while longer distance jumps show takeoff velocities with lower angles and higher magnitudes. This trend can be seen in Figure 4.8 in Chapter 4.

Next, the mean weight trajectories were compared based on jump grading. Since the distance to the target affects the length of the flight phase, comparing jumps to different targets reduces the temporal alignment accuracy between the trajectories, and makes direct comparison of the weight trajectories more difficult (especially during the landing phase). Therefore, mean weight trajectories were compared between jump grades for each target separately. Figure 5.4 shows mean weight trajectories for all medium target distance jumps, between jumps short of the target (graded B or SB), jumps on-target (P or P\*), and jumps exceeding the target distance (SF or F). The primary weight trajectory differences relative

to jump grade are observed in  $w_{CoM-Z}$  and  $w_{Toe-dZ}$ . Jumps short of the landing target have a larger  $w_{CoM-Z}$  before takeoff and a lower  $w_{Toe-dZ}$  prior to landing, while jumps that overshoot the target distance contain opposite trends, slightly smaller  $w_{CoM-Z}$  before takeoff and higher  $w_{Toe-dZ}$  before landing. Mean trajectories of all on-target jumps have  $w_{CoM-Z}$  and  $w_{Toe-dZ}$  trajectories between the aforementioned extrema. This suggests a gradient in the weight trajectory changes between too short and too far over the target distance, with a middle range of motor control trajectory behavior that results in an on-target jump. These observations are made based on motor control patterns for jumps to the medium distance target, but similar observations are seen for the short and long target distances.

Similar gradient behavior was observed in Chapter 4, based on the CoM trajectory data. CoM takeoff velocity vectors needed to be within the “on-target zone” to appropriately launch the body towards the target (see Section 4.3.1); the change in  $w_{CoM-Z}$  discussed above could be a result of this change in takeoff velocity. Also, foot placement needed to occur when the CoM was at a specific horizontal distance behind the target (see Section 4.3.2), which may relate to the peak height of  $w_{Toe-dZ}$  prior to landing.

Each participant in the experiment was designated a “novice” or an “expert” based on their overall jump success rate. The mean weight trajectories for all novice and all expert jumpers are compared in Figure 5.5. The expert jumpers are seen to have lower  $w_{CoM-Z}$  and higher  $w_{CoMToe-dX}$  during the takeoff phase, while novice jumpers have higher  $w_{CoM-Z}$  at takeoff. Kinetic energy has a slightly higher peak for expert jumpers at landing, which is likely due to the fact that expert jumpers were typically able to jump farther than novice jumpers, and so had to absorb more impact at landing.

The same tradeoff between  $w_{CoM-Z}$  and  $w_{CoMToe-dX}$  that was first seen in Figure 5.3 (looking at jumps to different target distances) is also seen here, suggesting that expert jumpers tend to generate their takeoff velocity with a lower angle than novices.

As with the comparison of expert and novice jumpers, the primary difference between the mean weight trajectory plots is a trade-off between  $w_{CoM-Z}$  and  $w_{CoMToe-dX}$ . The second set of jumps shows lower  $w_{CoM-Z}$  and higher  $w_{CoMToe-dX}$  during the takeoff phase compared to the first set of jumps. This trend suggests that the motor control patterns of novice jumpers change to resemble the average pattern seen in expert jumpers as novices practice more jumps. Expert jumpers by definition had higher jump success rates than novice jumpers, and the success rates of almost all participants were higher in their second jump set as compared to their first. Similar trends are seen for the short and long target distances.

Combining the observations from the novice/expert and motor learning weight tra-

jectory comparisons indicates that a motor control pattern that puts more priority to  $w_{CoM-dX}$ , relative to  $w_{CoM-Z}$ , results in a higher average jump success rate.

In general,  $w_{CoM-Z}$  and  $w_{CoMToe-dX}$  during the takeoff phase, and  $w_{Toe-dZ}$  and  $w_{KE}$  near or at landing, are the cost weights that vary the most relative to jump grading, target distance, jumper performance and motor learning.  $w_{CoMToe-dX}$  and  $w_{Toe-dX}$  are necessary motor control tasks for jumping to a target, but do not noticeably change with respect to the jump features investigated.



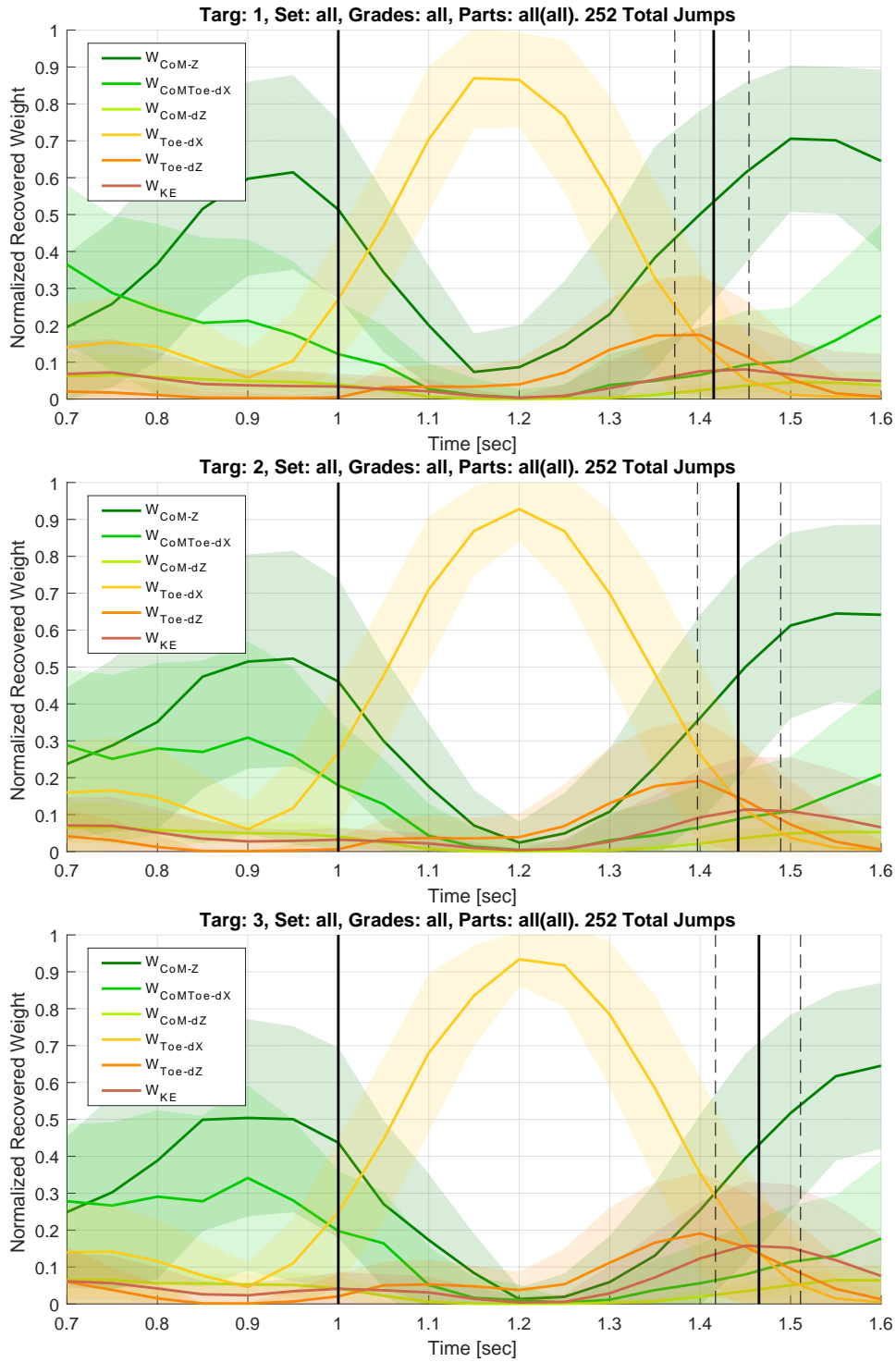


Figure (5.3) Comparison of mean weight trajectories for short (top), medium (middle), and long (bottom) target distances. Differences are seen in the  $w_{CoM-Z}$ ,  $w_{CoMToe-dX}$  and  $w_{KE}$  trajectories.

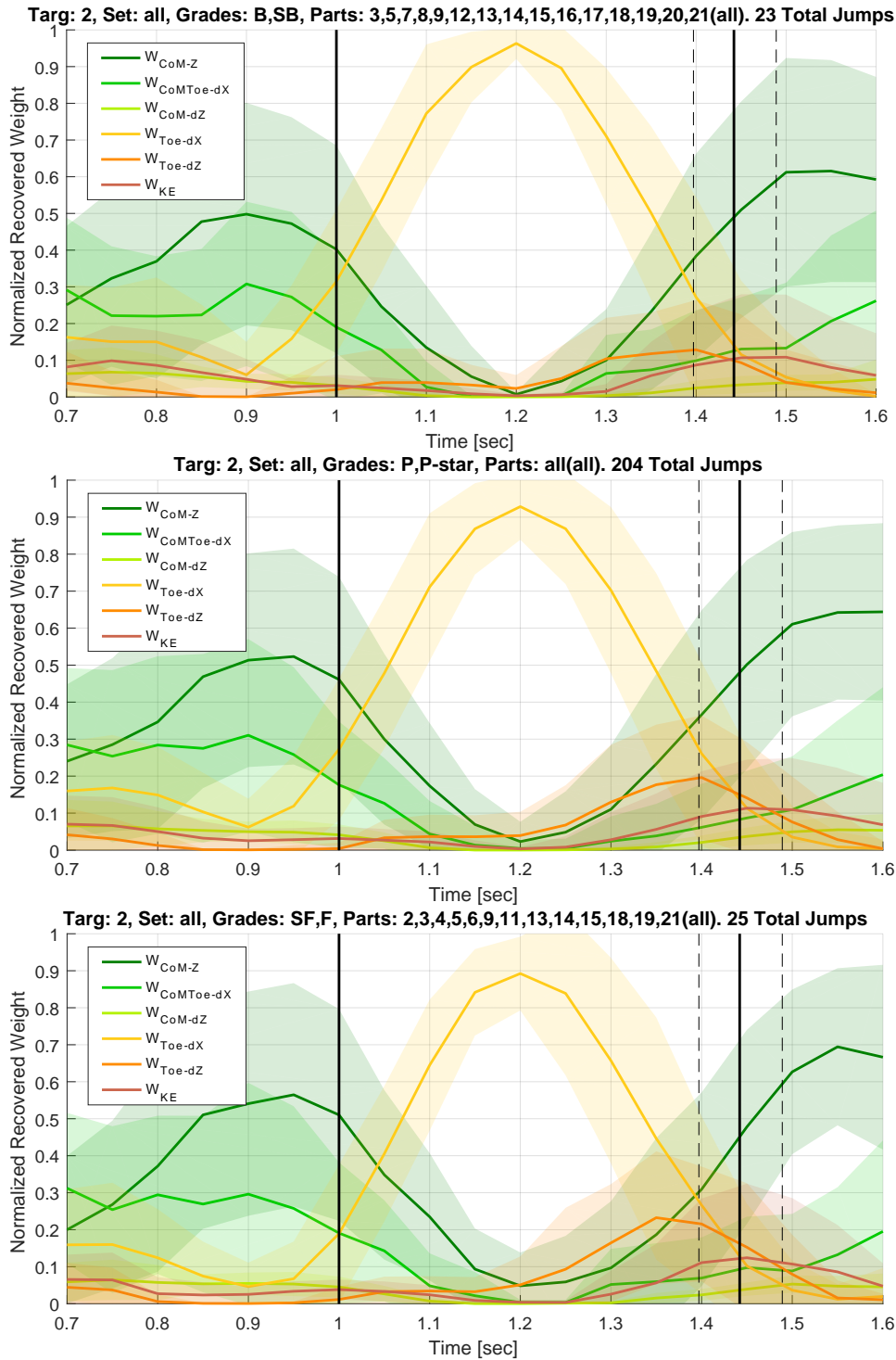


Figure (5.4) Mean weight trajectories for jumps to the medium distance target, comparing jumps graded as short of the target (top), on-target (middle), and overshooting the target (bottom). Differences are seen in the  $w_{CoM-Z}$  and  $w_{Toe-dZ}$  trajectories.

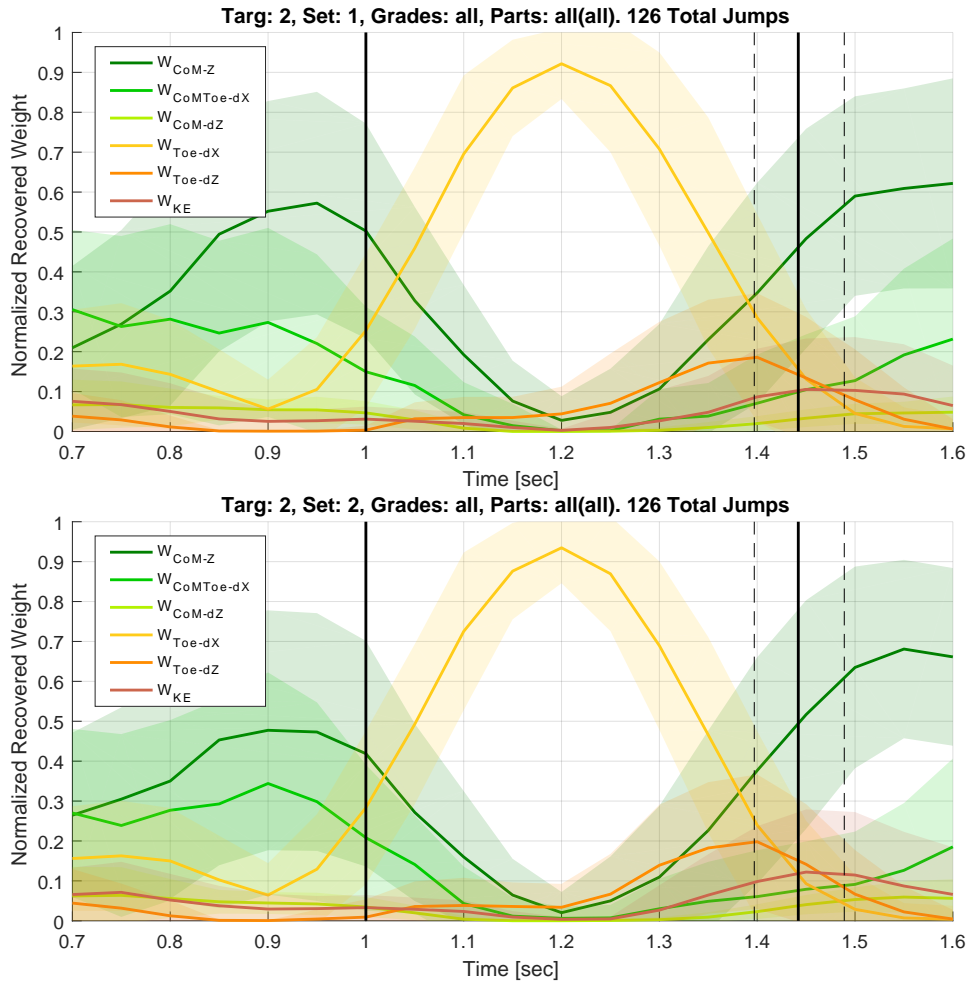


Figure (5.5) Comparison of mean weight trajectories for expert (top) and novice (bottom) participants. Differences are seen in the  $w_{CoM-Z}$  and  $w_{CoMToe-dX}$  trajectories.

## 5.3 IOC Weight Trajectory Clustering

The mean weight trajectory comparisons in the previous section were made by manually separating the jumping data into specific groups designed to identify motor control differences related to specific jump features. To determine if the recovered weights can be used to automatically group together similar motor control patterns, unsupervised clustering was performed on the IOC weight trajectory data for each jump. Section 2.4 contains a brief introduction to unsupervised clustering as it relates to this thesis.

### 5.3.1 Jump Style Analysis

The kmeans++ algorithm [4] was used to cluster the recovered cost term weight trajectories, where weight trajectories from one jump formed one observation. To preserve temporal alignment of trajectories, jumps to each target distance were clustered separately (as for the mean weight trajectory comparisons from the previous section). Clustering data for jumps to the middle distance target are presented in this section, and similar results were found for the short and long distance target jumps.

Cluster indices were compiled using between 2 and 20 clustering groups, and then the cluster results were compared. Clustering was performed multiple times for each number of groups to see how repeatable the classification of the observations was, since the kmeans++ algorithm is based on randomly initialized centroids [4]. The elbow method was used to determine the number of clusters to use [24], resulting in four clusters.

Jumps performed by a single jumper tended to be clustered in the same group. When comparing the jumpers in each group to their respective motion capture and trajectory data, the cluster groups seem to be indicative of “jumping style”, the coordination technique a jumper uses to perform the jump, and are not directly related to target distance, jump success rate (i.e. novice or expert designation), or motor learning.

Based on the video and kinematic visualization of the data clustered in each cluster, the four jumping styles were characterised as: (A) controlled takeoff and landing, (B) stiff legged landing, (C) explosive takeoff, and (D) hesitant landing. Three of the participants (ID 3, 13, and 19) were not included into a single group because their jumps were categorized into 3 or all 4 of the jump style groups, whereas most of the jumps from other participants were sorted into one predominant group.

To compare the motor control strategies of each group, the mean and standard deviation of the IOC weight trajectories of all participants in each group were plotted and

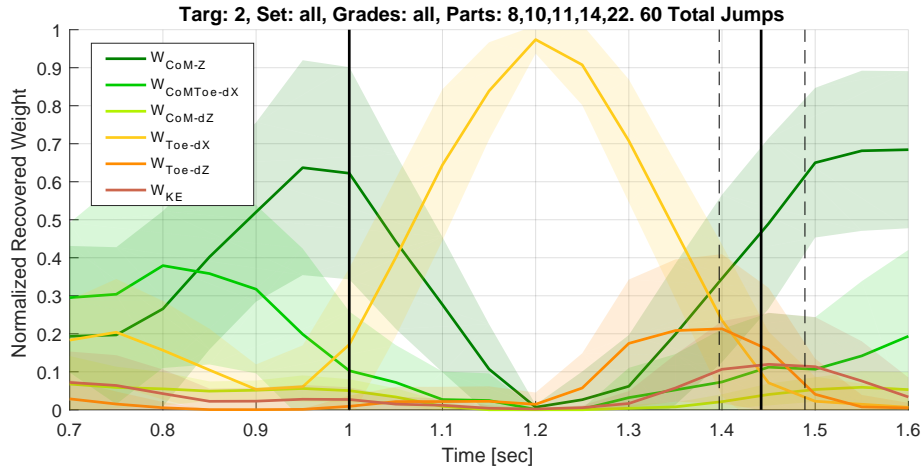


Figure (5.6) Mean weight trajectories for jumping style group A, controlled takeoff and landing.

compared. The mean weight trajectories of group A, controlled takeoff and landing, are shown in Figure 5.6, for the middle distance target. Jumpers in this group had cost weight trajectories with lower standard deviation than other groups, especially during the flight phase, and typically had a stable landing (little balance corrections required). Group A is characterized by a very high  $w_{CoM-Z}$  just prior to takeoff, as well as high  $w_{Toe-dZ}$  before landing. Additionally, the middle of the flight phase exhibits almost 100% weight from  $w_{Toe-dX}$ , more than any other group. The kinematic trajectory data of jumpers in this group exhibit higher takeoff velocity angles, which may explain the high  $w_{CoM-Z}$  just prior to takeoff.

The mean weight trajectories of group B, stiff legged landing, are shown in Figure 5.7. These jumpers typically left the ground with less vertical momentum, moved through the flight phase with extended legs, and kept their legs stiff and extended during the landing phase (rather than collapse their legs and lower their CoM, as jumpers in other groups did). Group B is characterized by a lower  $w_{CoM-Z}$  and higher  $w_{CoMToe-dX}$  trajectory than all other groups during takeoff. Also, at landing the average  $w_{KE}$  is higher than normal.

Jumpers in this group have CoM position trajectories that remain higher above the ground after landing compared to other groups. This observation matches the “stiff leg” behavior seen in the video and kinematic visualizations, and also related to the high kinetic energy absorbed at landing.

The mean weight trajectories of group C, explosive takeoff, are shown in Figure 5.8. As can be inferred from the group name, jumpers of this style generated more momentum,

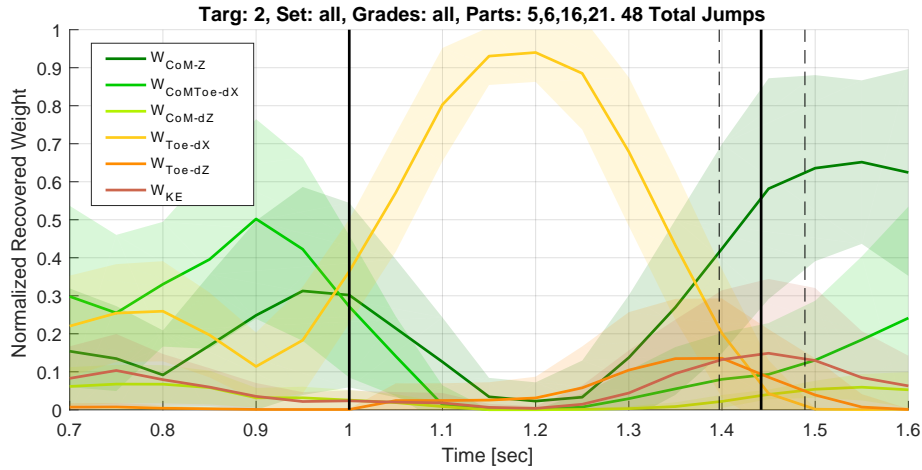


Figure (5.7) Mean weight trajectories for jumping style group B, stiff legged landing.

jumped to farther target distances than those in other groups (based on their maximum distance calibration jumps), and brought their CoM low to the ground during the landing phase by collapsing their legs more than average. Group C is characterized by a high  $w_{CoM-Z}$  and a very low  $w_{CoMToe-dX}$  during takeoff. This is the only group with a peak in their  $w_{Toe-dZ}$  trajectory just after takeoff, and with the highest  $w_{Toe-dZ}$  peak at landing of any group. These jumpers also have a high  $w_{KE}$  peak that is quite late after landing, whereas the average jumper has a peak  $w_{KE}$  at or just after landing.

Kinematic trajectory data of jumpers in Group C show larger takeoff velocity magnitudes than other groups that could be responsible for the large recovered COM-height weight throughout the takeoff phase. Jumpers also exhibit much lower CoM position after landing, collapsing their legs to slowly absorb their large CoM momentum (contrary to the stiff-leg landing of Group B), aligning with the high  $w_{KE}$  peak observed well after landing.

The mean weight trajectories of group D, hesitant landing, are shown in Figure 5.9. Group D is characterized by a pre-landing peak in  $w_{Toe-dZ}$  earlier than usual. These jumpers also had the highest standard deviation in their jump trajectories of any group, meaning they were the least consistent in their motor control behavior. Jumpers in this group had lower average takeoff velocity magnitudes than other groups, but no other features were found to distinguish this group’s kinematic trajectory data from those of other groups.

It is important to note that all jump style groups show weight trajectories with smaller standard deviations than the previous “manually grouped” sets of jumps (with respect to target distance, jump grade, jumper success rate and motor learning), even when compared

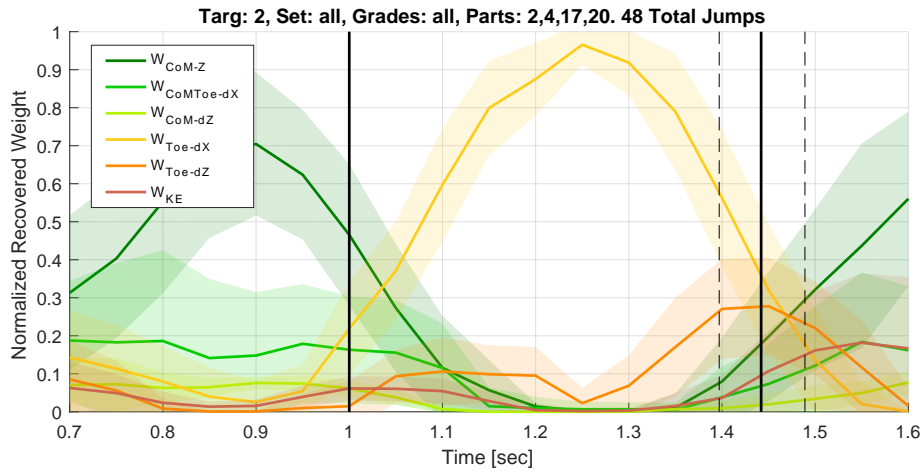


Figure (5.8) Mean weight trajectories for jumping style group C, explosive takeoff.

to the higher standard deviation of group D. The smaller standard deviation within these groups is expected, since the purpose of unsupervised clustering is to group together data points that are most similar to each other. The clustering comparisons also show that there are several possible variants to the general motor control pattern that people use when jumping to a target.

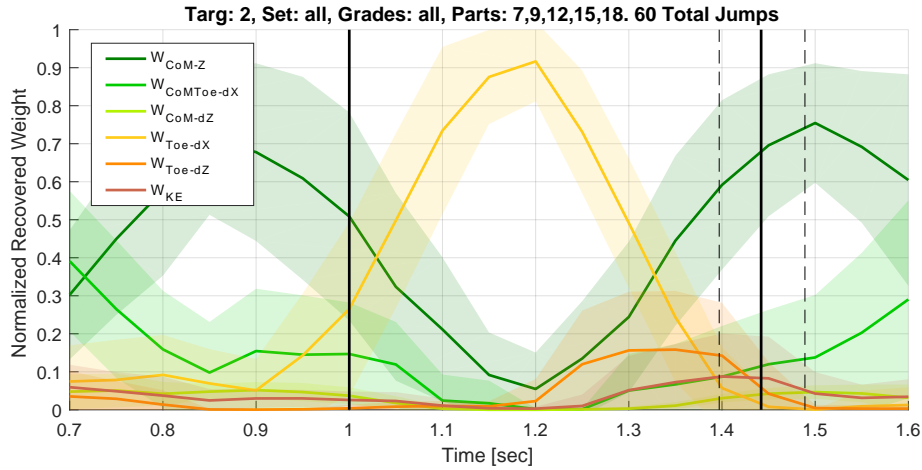


Figure (5.9) Mean weight trajectories for jumping style group D, hesitant landing.

### 5.3.2 PCA Clustering Visualization

Principal component analysis (PCA) was performed to visualize the separation of IOC weight trajectory data as related to unsupervised clustering groups, jump success, and motor learning. The first three principal components of the weight trajectory data used with the unsupervised clustering algorithm were plotted on the three axes of a 3D scatter plot. Points were plotted for each jump observation (252 jumps to each target), and color coded based on various features.

The principal components were categorized based on the unsupervised clustering indices formed by the k-means++ algorithm. The four different clusters that each jump was categorized into were plotted with four different colours. Figure 5.10 displays two different views of the same 3D scatter plot, and shows good distinction between the groups.

Next, the jumps performed by each participant were highlighted in the plot. Four plots are shown in Figure 5.11, each one highlighting the 12 jumps to the middle distance target performed by a certain jumper. Note that the jumps from a particular jumper are typically clustered together within the space of the first three principal components, and most belong to the same cluster group (i.e. the jump style they were categorized into).

On average, expert jumpers had tighter jump clustering than novice jumpers in the PCA visualization, suggesting that expert jumpers were more consistent in their general motor control strategy for jumping. For the three participants that could not be categorized into a single jump style cluster, their sets of jumps were not as tightly clustered and belong to three, or sometimes all four, of the cluster groups.



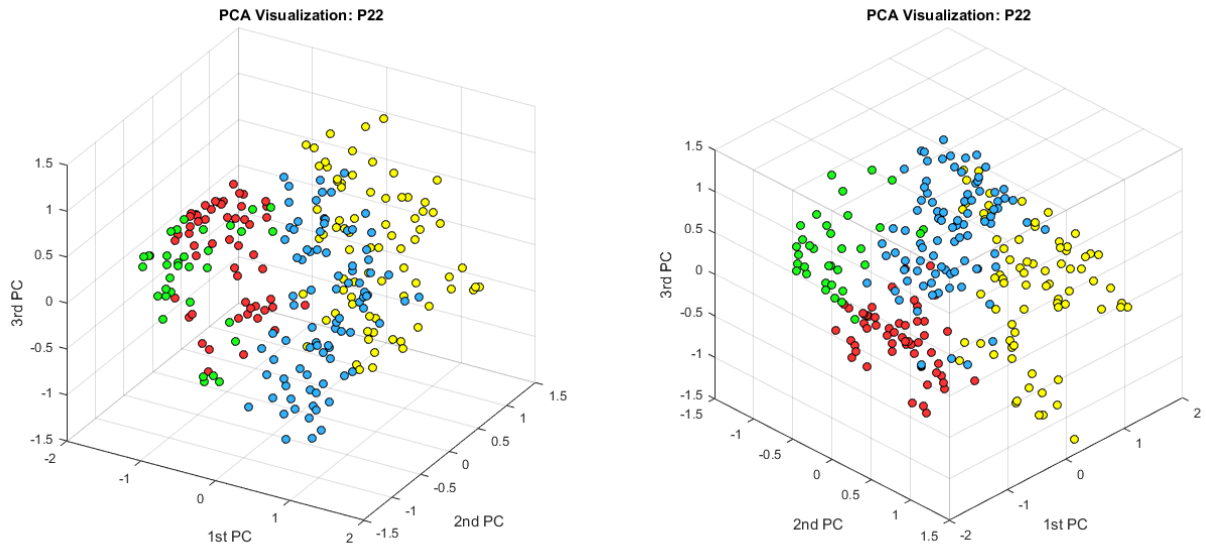


Figure (5.10) Visual representation of the first three principal components of all IOC weight trajectories. Observations (jumps) are colour-coded based on their kmeans cluster group. Two different views are shown of the same 3D plot.

The PCA scatter plot data were also visually categorized based on jump grade and jump set number (to detect changes relative to motor learning), but these categories did not show any significant trends based on the first three principal components of the IOC weight trajectories.

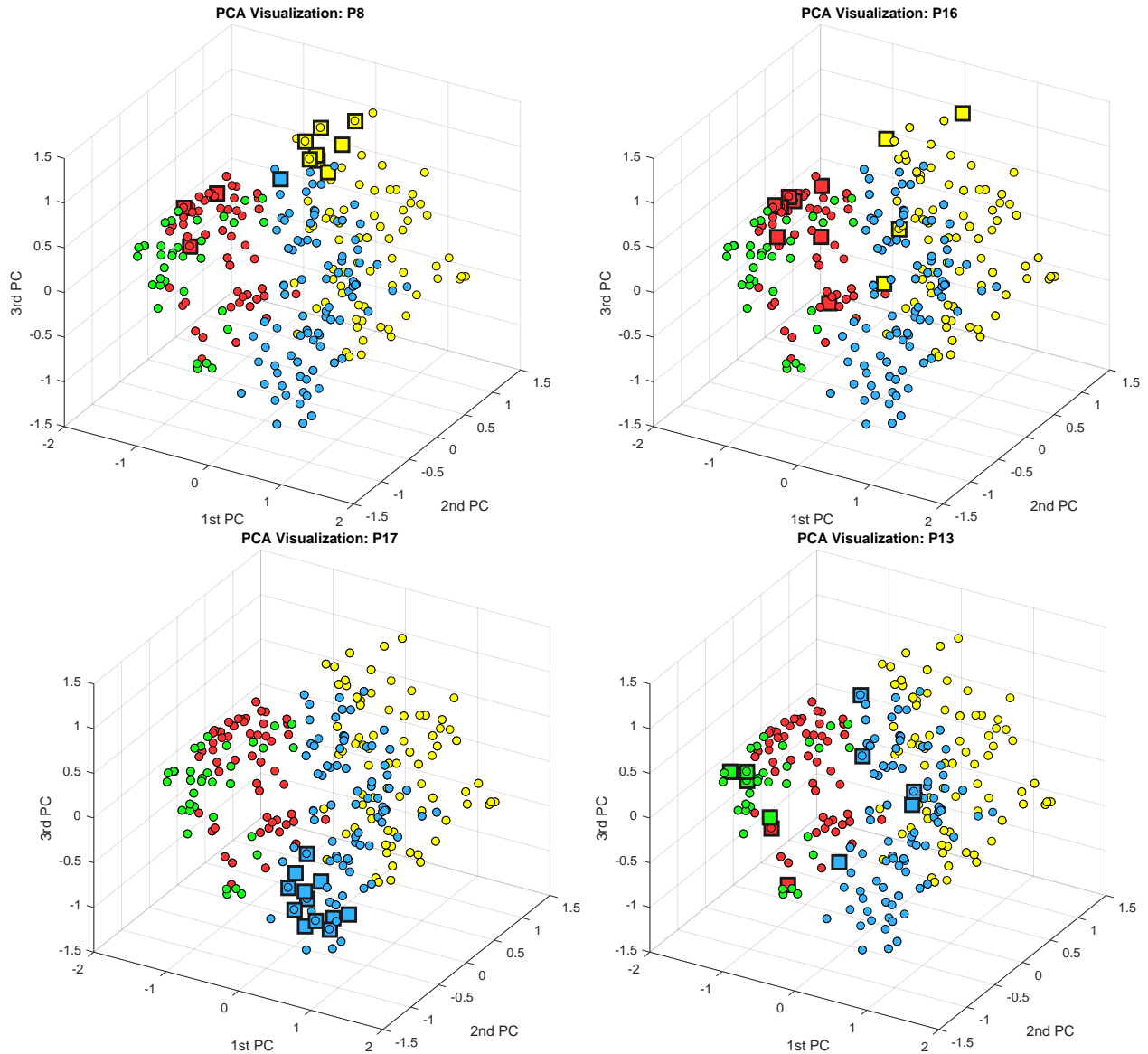


Figure (5.11) Visual representation of the first three principal components of all IOC weight trajectories, with jumps from a single jumper highlighted with a thicker edge line in each plot. Observations (jumps) are colour-coded based on their kmeans cluster group. Jump sets from four jumpers are shown, with novice (top left and right), expert (bottom left), and uncategorized (bottom right) examples.

## 5.4 IOC Conclusion

The recovered weight trajectories identified with the IOC approach reveal a general pattern of optimized motor control task for all jumps in the dataset. Clear changes in the optimized control tasks were observed relative to different target distances, jump grade, and average jumping success rate. Unsupervised clustering was used to identify motor control patterns corresponding to four distinct jumping styles observed in experiment participants, demonstrating that multiple control strategies can be used to successfully jump to a target.

# Chapter 6

## Conclusion

### 6.1 Conclusions

Investigating optimal human movement and associated motor control is crucial to fields such as human rehabilitation, sports training, humanoid robot control and human-robot interaction. In this thesis, the jumping to a target movement was investigated to develop and test a framework for the analysis of general dynamic human motions. This framework focuses on movement for task optimization, where a metric of task success can be clearly defined.

An experiment was designed to record motion capture kinematic data of jumping movements performed by 22 participants. Each jump was graded in terms of movement success, where success meant landing in the middle of the pre-determined landing target. Joint trajectories were derived from the motion capture marker trajectories using pose estimation and temporally aligned.

These kinematic trajectories were analyzed to find trends between trajectory features and jump success. The two trends most influential to jump success were the CoM takeoff velocity, which guided the body along an appropriate ballistic trajectory to the desired target, and the foot placement pose at landing, which controlled the absorption of the CoM momentum and corrected for inaccuracies in CoM takeoff velocity. These jump features were also compared with respect to jumper performance and motor learning. Novice jumpers were found to improve their CoM takeoff velocity consistency the more they jumped, while experts were seen to have greater control over their foot placement pose.

An IOC sliding window approach was used to examine motor control behavior of the experimental jumping data. Motor control tasks were hypothesized based on jumping-specific motions and tasks previously identified as relevant for general human motion. An IOC solver was used to extract the relative contributions of motor control tasks throughout each jump trajectory. These control task trajectories were compared with respect to jump success, jumper performance and motor learning. The control tasks which varied most relative to these jump characteristics were  $w_{CoM-Z}$  and  $w_{CoM-dX}$  during the takeoff phase, and  $w_{Toe-dZ}$  and  $w_{KE}$  at and after landing. As novice jumpers gained more practice, their motor control behavior was observed to approach that of expert jumpers. Unsupervised clustering techniques applied to the control task trajectories classified experiment participants into four jump styles, independent of overall jumper performance and motor learning.

The contributions of this thesis are:

### 6.1.1 Human Jumping to a Target Dataset

Previous research into human jumping focused on maximum height or maximum distance jumping, or the required dynamics to perform a jump of any kind. This thesis provides the first dataset of the standing broad jump to a target movement, where the task is to land as close to a pre-determined landing location as possible.

An experiment was designed and executed to capture the data required for investigating jumping to a target with respect to motor control concepts. Extended Kalman filter pose estimation was used to extract joint trajectories from the experimental movement data based on a full body kinematic model.

### 6.1.2 Kinematic Analysis of Human Jumping to a Target

The kinematic data was analyzed to identify kinematic correlates to jump success. Two trends were identified in the jump trajectories that influenced jump success. First, the takeoff velocity must be within an appropriate range for the jumper to travel an adequate distance to reach the target. If the landing target is larger, there is a larger range of acceptable takeoff velocities to complete the jump. Next, foot placement pose can be controlled to correct for inaccurate takeoff velocity. The jumper can extend their legs to land sooner, or collapse their legs to land later, which results in a shorter or longer distance travelled, respectively

Novice jumpers were generally observed to improve their jump success rate more than experts during the experiment. Novice jumpers usually improved their takeoff velocity consistency in subsequent jump sets, but improvement in foot placement control was observed less often. Expert participants had better foot placement control than novices, and could properly adapt their foot placement in the presence of takeoff velocity inaccuracies.

### 6.1.3 Sliding Window Inverse Optimal Control for Human Movement Motor Control

An IOC approach was used to extract the optimized motor control tasks of jumping to a target. Cost terms were hypothesized based on jumping-specific control tasks and criteria relevant to general human motion. A sliding window approach was used to detect how the relative weighting of the cost terms changes throughout the jumping trajectory, removing a common IOC assumption of constant recovered cost term weights. While this approach has previously been used for human motion segmentation, using it for identifying motor control tasks is a novel application of the sliding window method.

The recovered IOC cost term weights were averaged over different sets of jump features. Changes in average cost term weights were observed relative to jump grade, target distance, and jump performance. Experts were observed to optimize  $w_{CoM-dX}$  before takeoff more than novice jumpers, who optimized  $w_{CoM-Z}$  more. As novice jumpers improved their success rate during the experiment, their motor control behavior more closely resembled that of experts.

Parallels were also drawn between the kinematic trajectory results and IOC motor control task results. Optimized CoM velocity ( $w_{CoM-dX}$ ) before takeoff and toe velocity ( $w_{Toe-dZ}$ ) prior to landing can be related to controlling takeoff velocity and foot placement pose respectively, as observed in the kinematic analysis.

Finally, the IOC sliding window approach was used alongside unsupervised clustering techniques to identify four jumping styles that the experiment participants could be categorized into. All style groups included novice and expert jumpers, and were independent of jump success or motor learning, suggesting there are multiple general motor control patterns that can be used for successfully jumping to a target.

## 6.2 Future Work

This project contributes toward a greater understanding of jumping motions, and helps develop a framework for general human motion analysis. This section discusses future directions to expand on the results presented in this thesis.

### 6.2.1 Different Jumping Conditions

The great majority of jumps completed during the experiment were on-target. Additional experimental variations could provide more challenging jump conditions to provide additional data for unsuccessful jumps. A narrower landing target would require more precise motor control from the jumper to complete a successful jump. The smaller landing target would result in a smaller “on-target zone” for a jumper’s takeoff velocity, and require more accurate control over their foot placement pose to correct for takeoff velocity inaccuracies. Although a lower percentage of perfect jumps would be captured in a dataset using a smaller target, it is predicted that clearer trends between kinematic trajectory features and jump success would be observed.

The jumping experiment was narrowly focused on the standing broad jump on level ground, with a high-friction landing platform that is perpendicular to the direction of the jump. However, jumping motions can be performed in many different environments, and would likely require different motor control patterns. To develop a more complete understanding of human jumping motor control, jumping in different environments and landing conditions should be investigated. Some jumping environment variables to investigate further are: target size; target orientation (parallel, perpendicular or diagonal to jump direction, angled to the horizontal); height and depth jumps; multi-step or running jumps; jumping sideways; landing on one leg; friction parameters of the ground during takeoff and landing.

### 6.2.2 Data Collection and Analysis

While motion capture measurement is the industry standard for capturing human kinematic motion, additional sensors could better record other dynamic and timing data associated with jumping to a target. Using force plates under the landing target would give impact force measurements, with which more accurate joint torque data and other dynamic model parameters could be computed. Pressure plate sensors and/or close-up image

data could provide more accurate and objective jump grading results for comparison with trajectory data.

The IOC analysis was carried out on a simplified planar model. Repeating the IOC analysis using the full 3D kinematic model could reveal additional motor control features that contribute to jumping success [27].

Foot placement timing could potentially be estimated using a three-dimensional foot placement estimator (3DFPE) model, as proposed by Millard *et al.* [43] and typically used for human gait analysis or humanoid motion control. Despite the fact that jumping motions violate most of the assumptions made in FPE models (such as flat feet on the ground, constant leg length, short impact, and constant system inertia and energy), Millard *et al.* suggested that jumpers adjust their foot placement to accommodate the violations to these assumptions that occur during landing. The distance  $X_{fp}$  described in Section 4.3.2 is related to the calculated FPE and capture point (CAP) positions described in Millard's work

The research into depth jump landing by Maldonado *et al.* [41] proposed the uncontrolled manifold approach (UCM) to analyze dynamic human movement. The UCM approach identifies an index of motor task control (ITC) to gauge the control priority of several hypothesized motor control tasks. The UCM approach could be applied to the dataset created for this project to see if the ITC results of jumping to a target agree with the IOC motor control pattern results discussed in this thesis. Additionally, this would test the dynamic extension of UCM on a richer dataset than in Maldonado *et al.* (containing both successful and failed attempts, experts and novices, and motor learning effects).



# References

- [1] Jack A Adams. A closed-loop theory of motor learning. *Journal of motor behavior*, 3(2):111–150, 1971.
- [2] Jake K Aggarwal and Quin Cai. Human motion analysis: A review. *Computer vision and image understanding*, 73(3):428–440, 1999.
- [3] Kamiar Aminian and Bijan Najafi. Capturing human motion using body-fixed sensors: outdoor measurement and clinical applications. *Computer animation and virtual worlds*, 15(2):79–94, 2004.
- [4] David Arthur and Sergei Vassilvitskii. k-means++: The advantages of careful seeding. In *Proceedings of the eighteenth annual ACM-SIAM symposium on Discrete algorithms*, pages 1027–1035. Society for Industrial and Applied Mathematics, 2007.
- [5] Blake M Ashby and Jean H Heegaard. Role of arm motion in the standing long jump. *Journal of biomechanics*, 35(12):1631–1637, 2002.
- [6] Roger Bartlett, Jon Wheat, and Matthew Robins. Is movement variability important for sports biomechanists? *Sports biomechanics*, 6(2):224–243, 2007.
- [7] Andrea Bauer, Dirk Wollherr, and Martin Buss. Human–robot collaboration: a survey. *International Journal of Humanoid Robotics*, 5(01):47–66, 2008.
- [8] Bastien Berret, Enrico Chiovetto, Francesco Nori, and Thierry Pozzo. Evidence for composite cost functions in arm movement planning: an inverse optimal control approach. *PLoS computational biology*, 7(10):e1002183, 2011.
- [9] C Bosco, A Ito, PV Komi, P Luhtanen, P Rahkila, H Rusko, and JT Viitasalo. Neuromuscular function and mechanical efficiency of human leg extensor muscles during jumping exercises. *Acta Physiologica Scandinavica*, 114(4):543–550, 1982.

- [10] Stephen Boyd and Lieven Vandenberghe. *Convex optimization*. Cambridge university press, 2004.
- [11] Richard H Byrd, Jean Charles Gilbert, and Jorge Nocedal. A trust region method based on interior point techniques for nonlinear programming. *Mathematical Programming*, 89(1):149–185, 2000.
- [12] Kuangyou B Cheng, Chih-Hung Wang, Hui-Chuan Chen, Chin-Dai Wu, and Hung-Ta Chiu. The mechanisms that enable arm motion to enhance vertical jump performancea simulation study. *Journal of biomechanics*, 41(9):1847–1854, 2008.
- [13] Mark M Churchland, Afsheen Afshar, and Krishna V Shenoy. A central source of movement variability. *Neuron*, 52(6):1085–1096, 2006.
- [14] Debora Clever and Katja D Mombaur. An inverse optimal control approach for the transfer of human walking motions in constrained environment to humanoid robots. In *Robotics: Science and systems*, 2016.
- [15] Raphael Dumas, Laurence Cheze, and J-P Verriest. Adjustments to mcconville et al. and young et al. body segment inertial parameters. *Journal of biomechanics*, 40(3):543–553, 2007.
- [16] Peter Englert and Marc Toussaint. Inverse kkt–learning cost functions of manipulation tasks from demonstrations. In *Robotics Research*, pages 57–72. Springer, 2018.
- [17] Saeed Davoudabadi Farahani, Michael Skipper Andersen, Mark de Zee, and John Rasmussen. Optimization-based dynamic prediction of kinematic and kinetic patterns for a human vertical jump from a squatting position. *Multibody system dynamics*, 36(1):37–65, 2016.
- [18] Martin L Felis, Katja Mombaur, and Alain Berthoz. An optimal control approach to reconstruct human gait dynamics from kinematic data. In *2015 IEEE-RAS 15th International Conference on Humanoid Robots (Humanoids)*, pages 1044–1051. IEEE, 2015.
- [19] Andrea J Fradkin, Tsharni R Zazryn, and James M Smoliga. Effects of warming-up on physical performance: a systematic review with meta-analysis. *The Journal of Strength & Conditioning Research*, 24(1):140–148, 2010.
- [20] Douglas C Giancoli. *Physics: Principles with applications*. Pearson Higher Ed, 2013.

- [21] Mohinder S Grewal. Kalman filtering. In *International Encyclopedia of Statistical Science*, pages 705–708. Springer, 2011.
- [22] Marina Guihard and Philippe Gorce. Simulation of a dynamic vertical jump. *Robotica*, 19(1):87–91, 2001.
- [23] Kensuke Harada, Shuuji Kajita, Kenji Kaneko, and Hirohisa Hirukawa. An analytical method for real-time gait planning for humanoid robots. *International Journal of Humanoid Robotics*, 3(01):1–19, 2006.
- [24] André Hardy. An examination of procedures for determining the number of clusters in a data set. In *New approaches in classification and data analysis*, pages 178–185. Springer, 1994.
- [25] ME Harrington, AB Zavatsky, SEM Lawson, Z Yuan, and TN Theologis. Prediction of the hip joint centre in adults, children, and patients with cerebral palsy based on magnetic resonance imaging. *Journal of biomechanics*, 40(3):595–602, 2007.
- [26] Stewart Heitmann, Michael Breakspear, and Norm Ferns. Muscle co-contraction modulates damping and joint stability in a three-link biomechanical limb. *Frontiers in neurorobotics*, 5:5, 2012.
- [27] Lauren J Hickox, Blake M Ashby, and Gordon J Alderink. Exploration of the validity of the two-dimensional sagittal plane assumption in modeling the standing long jump. *Journal of biomechanics*, 49(7):1085–1093, 2016.
- [28] Neville Hogan. Skeletal muscle impedance in the control of motor actions. *Journal of mechanics in medicine and biology*, 2(03n04):359–373, 2002.
- [29] Yuri P Ivanenko, Richard E Poppele, and Francesco Lacquaniti. Motor control programs and walking. *The Neuroscientist*, 12(4):339–348, 2006.
- [30] Vlad Joukov, Rollen DSouza, and Dana Kulić. Human pose estimation from imperfect sensor data via the extended kalman filter. In *International Symposium on Experimental Robotics*, pages 789–798. Springer, 2016.
- [31] Takayuki Kanda and Hiroshi Ishiguro. *Human-robot interaction in social robotics*. CRC Press, 2016.
- [32] Leonard Kaufman and Peter J Rousseeuw. *Finding groups in data: an introduction to cluster analysis*, volume 344. John Wiley & Sons, 2009.

- [33] Eamonn Keogh and Chotirat Ann Ratanamahatana. Exact indexing of dynamic time warping. *Knowledge and information systems*, 7(3):358–386, 2005.
- [34] Arezou Keshavarz, Yang Wang, and Stephen Boyd. Imputing a convex objective function. In *Intelligent Control (ISIC), 2011 IEEE International Symposium on*, pages 613–619. IEEE, 2011.
- [35] RL Kirby, NA Price, and DA MacLeod. The influence of foot position on standing balance. *Journal of biomechanics*, 20(4):423–427, 1987.
- [36] Donald E Kirk. *Optimal control theory: an introduction*. Courier Corporation, 2012.
- [37] Anna Lena Kleesattel, Debora Clever, Johannes Funken, Wolfgang Potthast, and Katja Mombaur. Modeling and optimal control of able-bodied and unilateral amputee running. *ISBS Proceedings Archive*, 35(1):20, 2017.
- [38] Mark L Latash, John P Scholz, and Gregor Schöner. Motor control strategies revealed in the structure of motor variability. *Exercise and sport sciences reviews*, 30(1):26–31, 2002.
- [39] Jonathan Feng-Shun Lin, Vincent Bonnet, Adina M Panchea, Nacim Ramdani, Gentiane Venture, and Dana Kulić. Human motion segmentation using cost weights recovered from inverse optimal control. In *Humanoid Robots (Humanoids), 2016 IEEE-RAS 16th International Conference on*, pages 1107–1113. IEEE, 2016.
- [40] Jim Mainprice, Rafi Hayne, and Dmitry Berenson. Predicting human reaching motion in collaborative tasks using inverse optimal control and iterative re-planning. In *2015 IEEE International Conference on Robotics and Automation (ICRA)*, pages 885–892. IEEE, 2015.
- [41] Galo Maldonado, François Bailly, Philippe Souères, and Bruno Watier. On the coordination of highly dynamic human movements: an extension of the uncontrolled manifold approach applied to precision jump in parkour. *Scientific reports*, 8(1):12219, 2018.
- [42] A Meghdari and M Aryanpour. Dynamical modeling and analysis of the human jumping process. In *ASME 2002 International Mechanical Engineering Congress and Exposition*, pages 453–461. American Society of Mechanical Engineers, 2002.
- [43] Matthew Millard, John McPhee, and Eric Kubica. Foot placement and balance in 3d. *Journal of Computational and Nonlinear Dynamics*, 7(2):021015, 2012.

- [44] Djordje Mitrovic, Stefan Klanke, Rieko Osu, Mitsuo Kawato, and Sethu Vijayakumar. A computational model of limb impedance control based on principles of internal model uncertainty. *PloS one*, 5(10):e13601, 2010.
- [45] Katja Mombaur, Anh Truong, and Jean-Paul Laumond. From human to humanoid locomotion an inverse optimal control approach. *Autonomous robots*, 28(3):369–383, 2010.
- [46] Rieko Osu and Hiroaki Gomi. Multijoint muscle regulation mechanisms examined by measured human arm stiffness and emg signals. *Journal of neurophysiology*, 81(4):1458–1468, 1999.
- [47] H Nevzat Özgüven and Necip Berme. An experimental and analytical study of impact forces during human jumping. *Journal of Biomechanics*, 21(12):1061–1066, 1988.
- [48] Marcus G Pandy, Felix E Zajac, Eunsup Sim, and William S Levine. An optimal control model for maximum-height human jumping. *Journal of biomechanics*, 23(12):1185–1198, 1990.
- [49] Anne-Sophie Puydupin-Jamin, Miles Johnson, and Timothy Bretl. A convex approach to inverse optimal control and its application to modeling human locomotion. In *2012 IEEE International Conference on Robotics and Automation*, pages 531–536. IEEE, 2012.
- [50] DG Robertson and D Fleming. Kinetics of standing broad and vertical jumping. *Can J Sport Sci*, 12(1):19–23, 1987.
- [51] David A Rosenbaum. *Human motor control*. Academic press, 2009.
- [52] Richard A Schmidt and Craig A Wrisberg. *Motor learning and performance: A situation-based learning approach*. Human kinetics, 2008.
- [53] Thomas Seel, Jörg Raisch, and Thomas Schauer. Imu-based joint angle measurement for gait analysis. *Sensors*, 14(4):6891–6909, 2014.
- [54] Frank G Shellock and William E Prentice. Warming-up and stretching for improved physical performance and prevention of sports-related injuries. *Sports Medicine*, 2(4):267–278, 1985.
- [55] Masahiro Shiomi, Francesco Zanlungo, Kotaro Hayashi, and Takayuki Kanda. Towards a socially acceptable collision avoidance for a mobile robot navigating among

- pedestrians using a pedestrian model. *International Journal of Social Robotics*, 6(3):443–455, 2014.
- [56] Mark W Spong, Seth Hutchinson, Mathukumalli Vidyasagar, et al. *Robot modeling and control*. 2006.
- [57] Emanuel Todorov and Michael I Jordan. Motor control strategies revealed in the structure of motor variability. *Nature neuroscience*, 5(11):1226, 2002.
- [58] Daniela Virgínia Vaz. Motor synergies research in physical therapy: advantages of the uncontrolled manifold approach. *Fisioterapia e Pesquisa*, 24(1):2–8, 2017.
- [59] Masaki Wakai and Nicholas P Linthorne. Optimum take-off angle in the standing long jump. *Human movement science*, 24(1):81–96, 2005.
- [60] David A Winter. Human balance and posture control during standing and walking. *Gait & posture*, 3(4):193–214, 1995.
- [61] QiDi Wu, ChengJu Liu, JiaQi Zhang, and QiJun Chen. Survey of locomotion control of legged robots inspired by biological concept. *Science in China Series F: Information Sciences*, 52(10):1715–1729, 2009.
- [62] Gabriele Wulf. Self-controlled practice enhances motor learning: implications for physiotherapy. *Physiotherapy*, 93(2):96–101, 2007.
- [63] Huiyu Zhou and Huosheng Hu. Human motion tracking for rehabilitationa survey. *Biomedical Signal Processing and Control*, 3(1):1–18, 2008.

# APPENDIX

# Appendix A

## Additional Tables



Marker Number	Marker Label	Full Name	Marker	Body Placement Description	Kinematic Link/Frame Attachment	Model Attachment
1	Neck	Neck		Back of neck at C7	spine @ upperBack	
2	SL	Shoulder Left		Acromion process	spine2shldr_L @ shoulder_L	
3	SR	Shoulder Right		Acromion process	spine2shldr_R @ shoulder_R	
4	HL	Hip Left		Anterior superior iliac spine (ASIS)	base (after world2base)	
5	HR	Hip Right		ASIS	base (after world2base)	
6	BT	Back Top		Back of waistband, approximately L5	base (after world2base)	
7	BL	Back Left		Posterior superior iliac spine (PSIS)	base (after world2base)	
8	BR	Back Right		PSIS	base (after world2base)	
9	ELLat	Elbow Left, Lateral		Humerus lateral epicondyle	uparm_L @ elbow_L	
10	ELMed	Elbow Left, Medial		Humerus medial epicondyle	uparm_L @ elbow_L	
11	WLLat	Wrist Left, Lateral		Styloid process, ulna	forearm_L @ wrist_L	
12	WLMed	Wrist Left, Medial		Styloid process, radius	forearm_L @ wrist_L	
13	ERLat	Elbow Right, Lateral		Humerus lateral epicondyle	uparm_R @ elbow_R	
14	ERMed	Elbow Right, Medial		Humerus medial epicondyle	uparm_R @ elbow_R	
15	WRLat	Wrist Right, Lateral		Styloid process, ulna	forearm_R @ wrist_R	
16	WRMed	Wrist Right, Medial		Styloid process, radius	forearm_R @ wrist_R	
17	KLLat	Knee Left, Lateral		Femur lateral epicondyle	thigh_L @ knee_L	
18	KLMed	Knee Left, Medial		Femur medial epicondyle	thigh_L @ knee_L	
19	ALLat	Ankle Left, Lateral		Fibula apex of lateral malleolus	shin_L @ ankle_L	
20	ALMed	Ankle Left, Medial		Tibia apex of medial malleolus	shin_L @ ankle_L	
21	FLLat	Foot Left, Lateral		5th metatarsus head (base of 5th toe)	foot_L @ toe_L	
22	FLMed	Foot Left, Medial		1st metatarsus head (base of big toe)	foot_L @ toe_L	
23	FLHeel	Foot Left, Heel		Posterior Surface of Calcaneus	foot_L @ toe_L	
24	KRLat	Knee Right, Lateral		Femur lateral epicondyle	thigh_R @ knee_R	
25	KRMed	Knee Right, Medial		Femur medial epicondyle	thigh_R @ knee_R	
26	ARLat	Ankle Right, Lateral		Fibula apex of lateral malleolus	shin_R @ ankle_R	
27	ARMed	Ankle Right, Medial		Tibia apex of medial malleolus	shin_R @ ankle_R	
28	FRLat	Foot Right, Lateral		5th metatarsus head (base of 5th toe)	foot_R @ toe_R	
29	FRMed	Foot Right, Medial		1st metatarsus head (base of big toe)	foot_R @ toe_R	
30	FRHeel	Foot Right, Heel		Posterior Surface of Calcaneus	foot_R @ toe_R	

Table (A.1) Motion capture marker labelling, placement and attachment location.

Joint Number	Joint Name	Located At	Joint Colour in Figure 3.4
1 2 3 4 5 6	pjoint0 pjoint1 pjoint2 rjoint0 rjoint1 rjoint2	world2base	N/A
7 8 9	back_jFB back_jAxial back_jLateral	base	blue blue blue
10 11 12 13 14 15	rshoulder_jprism rshoulder_jElevation rshoulder_jAbduction rshoulder_jExtRotation relbow_jFlexion relbow_jSupination	between upperback and rshoulder  shoulder_R  elbow_R	N/A orange green blue orange green
16 17 18 19 20 21	lshoulder_jprism lshoulder_jElevation lshoulder_jAbduction lshoulder_jExtRotation lelbow_jFlexion lelbow_jSupination	between upperback and lshoulder  shoulder_L  elbow_L	N/A orange green blue orange green
22 23 24 25 26 27 28	rhip_jFlexion rhip_jAbduction rhip_jExtRotation rknee_jExtension rknee_jExtRotation rankle_jDorsiflexion rankle_jPronation	hip_R   knee_R  ankle_R	orange green blue orange green orange green
29 30 31 32 33 34 35	lhip_jFlexion lhip_jAbduction lhip_jExtRotation lknee_jExtension lknee_jExtRotation lankle_jDorsiflexion lankle_jPronation	hip_L   knee_L  ankle_L	orange green blue orange green orange green

Table (A.2) Kinematic model joint names and locations.

Section	Markers		Participant ID Number																		MAE per Marker		
	Number	Label	2	3	4	5	6	7	8	9	10	11	12	13	14	15	16	17	18	19	20	21	22
Upper Back	1	Neck	<b>18.1</b>	11.3	8.8	11.4	8.6	7.5	8.9	15.0	9.9	11.6	5.9	9.3	11.2	6.4	7.9	10.5	8.9	8.3	11.9	14.6	9.2
	2	SL	14.8	12.0	7.4	16.0	8.9	8.7	<b>12.6</b>	19.4	<b>11.5</b>	<b>12.9</b>	7.7	14.1	11.6	8.6	<b>11.0</b>	10.7	7.5	<b>11.3</b>	<b>19.2</b>	11.7	11.7
	3	SR	<b>15.0</b>	12.4	8.9	<b>20.8</b>	10.3	9.3	9.9	16.9	10.0	11.8	6.4	<b>14.9</b>	12.1	8.2	8.4	11.3	8.2	9.5	<b>16.6</b>	<b>14.2</b>	11.8
Pelvis	4	HL	9.4	11.3	7.1	<b>16.3</b>	11.0	7.7	9.6	20.5	6.6	9.8	6.4	<b>16.7</b>	<b>12.6</b>	13.4	<b>9.3</b>	<b>15.2</b>	6.5	8.0	14.6	12.1	11.3
	5	HR	11.5	9.3	7.5	12.6	9.1	8.4	9.1	<b>30.0</b>	6.4	8.6	5.8	14.4	9.9	11.2	<b>11.4</b>	<b>14.2</b>	6.8	9.9	<b>20.0</b>	<b>13.0</b>	10.0
	6	BT	9.1	<b>14.8</b>	<b>12.7</b>	10.0	10.0	7.3	7.8	<b>22.8</b>	8.0	11.3	7.1	7.4	9.2	8.8	7.9	10.9	4.7	9.2	14.0	10.0	8.3
	7	BL	8.5	<b>16.9</b>	11.7	11.6	10.7	8.3	9.8	19.7	6.2	10.9	7.3	9.4	10.7	9.9	8.5	<b>11.7</b>	4.9	9.6	11.9	9.8	10.3
8	BR	9.5	<b>14.9</b>	11.7	12.0	10.1	8.5	10.2	<b>24.3</b>	6.3	12.2	6.4	9.6	9.4	9.1	8.9	11.2	5.3	9.9	13.2	11.7	9.0	
Left Arm	9	ELLat	14.9	10.1	7.2	10.3	13.4	7.3	11.2	20.1	<b>16.1</b>	6.5	<b>9.9</b>	9.9	7.6	16.4	8.5	10.2	<b>10.1</b>	10.4	11.0	<b>12.4</b>	8.3
	10	ELMed	<b>15.2</b>	8.9	7.6	10.5	<b>15.0</b>	6.7	10.0	20.5	<b>14.3</b>	7.5	8.0	13.3	10.9	<b>16.9</b>	6.8	9.4	8.9	<b>12.6</b>	13.4	11.1	7.4
	11	WLLat	5.9	2.9	4.3	5.2	5.6	3.5	3.2	4.7	3.9	2.6	3.1	6.0	3.8	3.4	2.6	5.2	6.4	4.6	5.5	3.7	2.3
	12	WLMed	6.0	3.9	4.7	4.1	3.1	4.3	3.9	8.1	5.6	4.8	3.8	5.8	3.6	5.9	4.8	3.7	5.7	7.5	7.7	5.2	5.8
Right Arm	13	ERLat	6.4	11.0	<b>13.5</b>	<b>16.9</b>	<b>14.0</b>	8.9	6.9	17.5	10.7	12.4	<b>14.9</b>	<b>17.9</b>	<b>15.5</b>	9.5	5.3	10.0	9.3	9.6	12.9	<b>12.8</b>	<b>12.2</b>
	14	ERMEd	7.2	10.4	12.2	14.4	<b>13.8</b>	<b>9.8</b>	9.9	17.0	10.4	<b>12.6</b>	<b>14.0</b>	<b>17.3</b>	<b>16.5</b>	11.6	5.5	9.7	9.7	<b>12.4</b>	<b>10.3</b>	10.9	11.0
	15	WRLat	4.1	3.8	3.6	3.2	3.8	2.5	3.3	5.9	4.8	3.4	4.0	6.7	5.3	3.2	2.2	5.8	3.3	3.9	6.5	3.6	3.7
	16	WRMed	4.9	3.8	4.0	5.8	2.9	4.7	2.7	6.4	5.3	4.9	3.9	5.4	4.6	7.4	3.8	4.0	3.0	5.0	6.3	6.1	6.0
Left Leg	17	KLLat	14.2	11.1	10.0	8.8	11.4	9.6	<b>12.4</b>	19.9	7.5	8.9	6.0	8.2	7.0	9.4	5.5	8.2	<b>10.8</b>	7.8	9.7	6.8	5.6
	18	KLMed	9.7	10.4	8.8	7.6	8.8	<b>12.3</b>	<b>12.7</b>	12.0	6.7	8.1	5.8	5.8	6.8	9.1	4.7	7.0	<b>13.3</b>	9.8	7.5	8.1	5.6
	19	ALLat	6.5	5.1	4.7	5.7	4.4	4.7	5.9	11.9	5.1	4.7	4.2	4.7	4.6	6.9	6.4	5.6	5.0	5.3	6.8	6.4	4.3
	20	ALMed	5.2	5.6	3.9	6.9	4.9	4.2	5.8	8.7	4.1	4.4	3.6	7.3	5.7	5.9	4.7	6.4	4.4	4.8	7.9	8.3	5.3
	21	FLLat	3.2	6.6	2.5	7.7	4.5	2.6	4.7	9.0	2.2	4.6	2.7	9.8	6.1	4.7	5.6	7.7	4.0	4.0	9.2	6.5	6.1
	22	FLMed	3.8	3.6	2.6	4.7	3.0	2.2	4.3	10.6	2.2	2.8	2.7	5.4	4.2	3.4	5.3	4.6	3.3	3.5	6.5	6.7	3.5
	23	FLHeel	7.1	5.9	5.7	6.8	5.9	4.3	5.2	11.7	4.2	5.2	4.8	6.9	5.4	6.2	5.3	6.2	4.1	5.5	8.4	6.8	5.3
Right Leg	24	KRLat	10.9	11.8	<b>14.8</b>	9.0	8.7	8.2	10.9	21.3	7.4	<b>12.5</b>	5.6	5.8	8.1	<b>17.9</b>	4.8	8.6	7.9	7.3	6.3	6.2	5.9
	25	KRMEd	8.8	9.2	11.5	10.1	6.9	<b>10.0</b>	10.7	14.4	8.1	10.0	4.7	4.3	8.3	<b>19.5</b>	5.6	6.4	9.1	9.9	6.4	9.6	5.4
	26	ARLat	5.2	6.6	5.5	5.9	5.5	4.3	5.5	9.3	4.6	5.4	3.4	6.5	5.2	7.6	5.3	7.1	4.0	5.1	6.2	4.8	5.8
	27	ARMEd	5.5	6.0	4.2	6.6	4.4	3.9	5.4	8.4	3.9	4.5	2.8	7.9	6.0	7.3	4.5	6.5	3.5	3.7	8.5	6.1	4.5
	28	FRLat	4.9	4.8	3.4	7.9	3.6	2.1	3.8	11.5	2.3	3.7	2.5	8.7	5.7	5.0	5.8	5.8	3.5	3.1	10.1	6.2	5.0
	29	FRMed	3.8	4.5	3.2	5.2	3.2	1.9	3.4	9.6	2.3	3.7	2.4	5.8	4.2	5.1	4.7	5.9	2.8	2.4	6.3	4.8	4.3
30	FRHeel	6.4	6.3	5.2	6.2	5.8	4.5	6.4	9.2	4.4	6.6	3.9	7.8	6.1	4.7	5.7	5.5	4.5	4.7	6.9	7.1	5.8	
MAE per Participant			8.5	8.5	7.3	9.3	7.7	6.3	7.5	14.6	6.7	7.6	5.7	9.1	7.9	8.8	6.2	8.2	6.3	7.3	10.1	8.5	7.1

Table (A.3) MAE for each marker [in mm], averaged over all jumps from each participant. The three highest marker MAEs for each participant are highlighted and bolded.

Section	Markers		Participant ID Number																		MAE per Marker		
	Number	Label	2	3	4	5	6	7	8	9	10	11	12	13	14	15	16	17	18	19	20	21	22
Upper Back	1	Neck	<b>56.5</b>	28.8	26.7	32.6	28.9	22.4	28.4	47.4	<b>36.6</b>	42.1	17.1	30.5	<b>37.4</b>	26.4	24.1	34.1	<b>29.5</b>	28.4	37.3	<b>50.6</b>	36.8
	2	SL	32.1	31.6	29.7	40.5	24.7	23.9	<b>52.0</b>	64.8	<b>37.6</b>	26.6	20.9	<b>30.9</b>	<b>39.3</b>	27.0	31.2	31.4	29.3	37.5	<b>53.8</b>	21.3	26.9
	3	SR	33.6	30.6	28.6	<b>56.0</b>	23.5	30.4	39.7	55.2	<b>38.9</b>	28.0	27.7	<b>31.3</b>	<b>33.4</b>	34.7	18.9	44.2	27.6	23.2	34.7	21.4	39.5
Pelvis	4	HL	26.2	28.2	28.8	<b>45.2</b>	32.3	27.9	28.6	38.9	27.3	31.8	35.6	<b>33.0</b>	31.5	46.8	17.9	31.4	25.0	25.8	26.0	24.6	32.9
	5	HR	29.7	21.9	33.3	27.5	28.6	29.1	27.7	58.9	24.9	26.6	30.4	22.9	23.5	32.8	27.7	25.4	27.7	31.4	<b>43.2</b>	32.1	24.4
	6	BT	<b>35.4</b>	<b>42.1</b>	<b>47.9</b>	39.6	<b>39.8</b>	<b>37.9</b>	<b>37.1</b>	<b>68.6</b>	31.4	<b>48.6</b>	<b>46.7</b>	26.3	34.6	<b>48.7</b>	<b>32.7</b>	<b>45.6</b>	<b>28.9</b>	<b>39.4</b>	<b>42.5</b>	<b>44.0</b>	<b>42.2</b>
	7	BL	34.9	<b>46.3</b>	<b>45.8</b>	<b>42.5</b>	<b>43.5</b>	<b>41.6</b>	<b>43.5</b>	<b>65.2</b>	28.7	<b>47.5</b>	<b>47.6</b>	28.4	<b>39.8</b>	<b>41.5</b>	<b>34.9</b>	<b>45.8</b>	<b>30.0</b>	<b>43.1</b>	36.6	<b>44.3</b>	<b>42.3</b>
	8	BR	<b>37.1</b>	<b>41.5</b>	<b>46.9</b>	<b>42.0</b>	<b>37.3</b>	<b>43.8</b>	<b>43.6</b>	<b>66.8</b>	31.9	<b>54.3</b>	<b>43.5</b>	25.2	34.5	<b>48.7</b>	<b>35.9</b>	<b>45.2</b>	<b>31.9</b>	<b>42.2</b>	38.0	<b>46.4</b>	<b>40.6</b>
Left Arm	9	ELLat	21.8	25.8	15.0	15.9	17.9	16.0	29.9	35.5	21.7	15.9	16.0	17.5	19.7	21.7	19.2	23.2	20.0	17.9	28.3	19.4	16.4
	10	ELMed	21.1	24.0	16.7	17.0	24.7	15.3	29.4	42.3	22.5	19.4	15.6	22.8	21.3	24.9	19.4	22.6	21.0	24.5	31.3	17.1	16.6
	11	WLLat	11.0	15.6	7.5	11.5	11.8	8.7	9.5	19.3	9.6	15.5	6.6	17.5	11.6	8.1	8.2	20.4	12.3	8.9	11.7	7.3	9.1
Right Arm	12	WLMed	14.2	14.7	11.8	10.7	7.1	13.8	18.8	24.5	11.7	16.9	10.8	14.2	12.6	14.0	19.4	16.9	12.1	15.5	20.2	13.8	19.4
	13	ERLat	14.7	19.4	19.8	28.7	21.1	15.1	18.8	30.3	19.3	19.1	18.6	23.3	25.8	20.7	10.3	29.6	16.8	19.1	24.9	21.2	21.5
	14	ERMEd	16.4	21.4	20.2	23.7	19.4	18.2	31.4	29.7	19.7	21.1	17.1	26.8	26.3	27.2	11.6	25.7	19.1	23.2	23.3	15.8	20.9
Left Leg	15	WRLat	11.0	14.2	8.5	8.3	10.2	6.9	11.2	16.8	7.5	9.3	5.9	12.3	13.1	7.5	6.9	17.4	11.7	8.1	20.3	7.4	12.6
	16	WRMed	10.9	15.0	9.8	17.4	6.8	20.6	8.4	18.0	12.2	16.6	7.1	10.4	13.6	20.6	11.1	13.1	9.2	8.9	18.0	15.0	22.7
	17	KLLat	34.9	29.7	32.7	24.8	29.2	18.4	19.3	58.7	23.8	28.7	33.4	22.0	23.0	34.3	25.3	30.1	17.6	31.1	34.4	30.8	21.1
	18	KLMed	33.6	39.4	27.1	21.7	30.3	28.3	22.2	40.5	34.8	26.9	25.8	14.1	27.2	28.7	20.1	34.3	27.0	24.1	32.6	28.3	20.9
	19	ALLat	17.2	16.9	19.8	20.7	16.9	16.2	15.2	29.3	13.8	22.8	18.7	14.5	15.0	19.0	20.4	15.8	13.9	17.5	18.8	14.2	13.8
	20	ALMed	17.4	17.0	10.7	17.7	17.6	14.2	15.7	20.2	18.5	14.7	11.4	12.1	14.8	18.1	11.9	16.9	13.6	17.7	16.0	11.5	15.3
	21	FLLat	15.4	11.9	10.7	11.9	11.6	8.6	22.2	17.7	11.5	9.6	17.1	12.6	15.9	14.1	14.1	14.1	17.8	12.8	22.6	20.2	11.0
	22	FLMed	10.8	10.7	9.8	9.8	10.5	9.3	14.3	14.3	9.7	10.0	16.6	15.0	13.3	13.5	13.2	13.1	9.8	10.7	12.8	13.1	10.1
	23	FLHeel	21.4	21.5	25.4	24.0	26.5	20.0	17.8	34.7	13.4	22.8	28.5	20.4	20.2	23.6	23.3	19.1	18.7	23.0	20.3	22.3	22.7
	Right Leg	24	KRLat	30.2	34.6	35.0	31.7	29.3	20.4	26.2	45.6	20.0	32.1	32.9	21.5	21.8	40.1	19.5	30.0	16.4	17.9	24.8	16.1
25		KRMEd	20.2	34.2	33.9	24.2	27.9	25.6	27.3	39.6	34.3	30.8	17.8	15.8	23.8	31.7	20.5	28.7	24.5	27.0	23.2	30.1	22.4
26		ARLat	14.5	21.7	20.8	21.7	15.2	19.3	14.1	21.4	16.3	23.0	16.5	13.3	12.6	17.9	16.0	14.6	12.6	14.0	15.1	13.4	17.5
27		ARMEd	14.3	17.6	12.9	13.1	13.4	12.8	16.4	22.2	22.3	10.4	10.3	10.0	12.5	15.1	12.1	13.7	12.5	10.1	20.9	13.7	9.8
28		FRLat	11.5	13.9	13.4	19.2	12.2	8.6	18.7	17.8	14.0	14.9	18.4	19.8	19.4	21.3	11.3	22.4	18.7	8.0	14.0	11.9	15.6
29		FRMed	10.9	12.2	13.0	12.4	10.8	9.7	17.4	18.3	14.9	14.5	13.2	13.5	12.7	16.3	9.3	10.6	14.1	8.2	11.4	14.1	11.7
30	FRHeel	18.3	22.3	27.0	22.9	21.7	20.7	19.0	35.6	17.2	24.1	24.4	14.7	13.9	21.7	21.5	16.1	18.1	19.1	16.7	22.1	21.3	
MAE per Participant			22.6	24.2	23.0	24.5	21.7	20.1	24.1	36.6	21.5	24.1	21.7	19.8	22.2	26.1	18.9	25.0	19.6	21.1	25.8	22.3	21.9

Table (A.4) Maximum MAE for each marker per jump [in mm], averaged over all jumps from each participant. The three highest marker MAE peaks for each participant are highlighted and bolded.

Participant Number	Target 1		Target 2		Target 3	
	Set 1	Set 2	Set 1	Set 2	Set 1	Set 2
<b>2</b>	4	3	4	5	2	4
<b>3</b>	2	4	3	1	0	0
<b>4</b>	4	5	3	3	0	1
<b>5</b>	1	3	4	2	2	2
<b>6</b>	4	4	4	2	4	2
<b>7</b>	4	6	5	6	4	4
<b>8</b>	2	4	2	6	4	4
<b>9</b>	3	4	2	4	2	4
<b>10</b>	5	6	6	5	5	5
<b>11</b>	2	5	4	4	1	2
<b>12</b>	5	6	4	6	6	5
<b>13</b>	4	4	3	5	1	2
<b>14</b>	2	4	2	4	1	2
<b>15</b>	2	5	2	3	4	4
<b>16</b>	2	3	4	6	5	6
<b>17</b>	4	6	5	4	5	5
<b>18</b>	4	4	3	3	4	3
<b>19</b>	4	3	2	5	3	4
<b>20</b>	5	5	3	6	5	6
<b>21</b>	4	4	5	2	3	3
<b>22</b>	4	4	5	5	3	4
<b>Total</b>	71	92	75	87	64	72

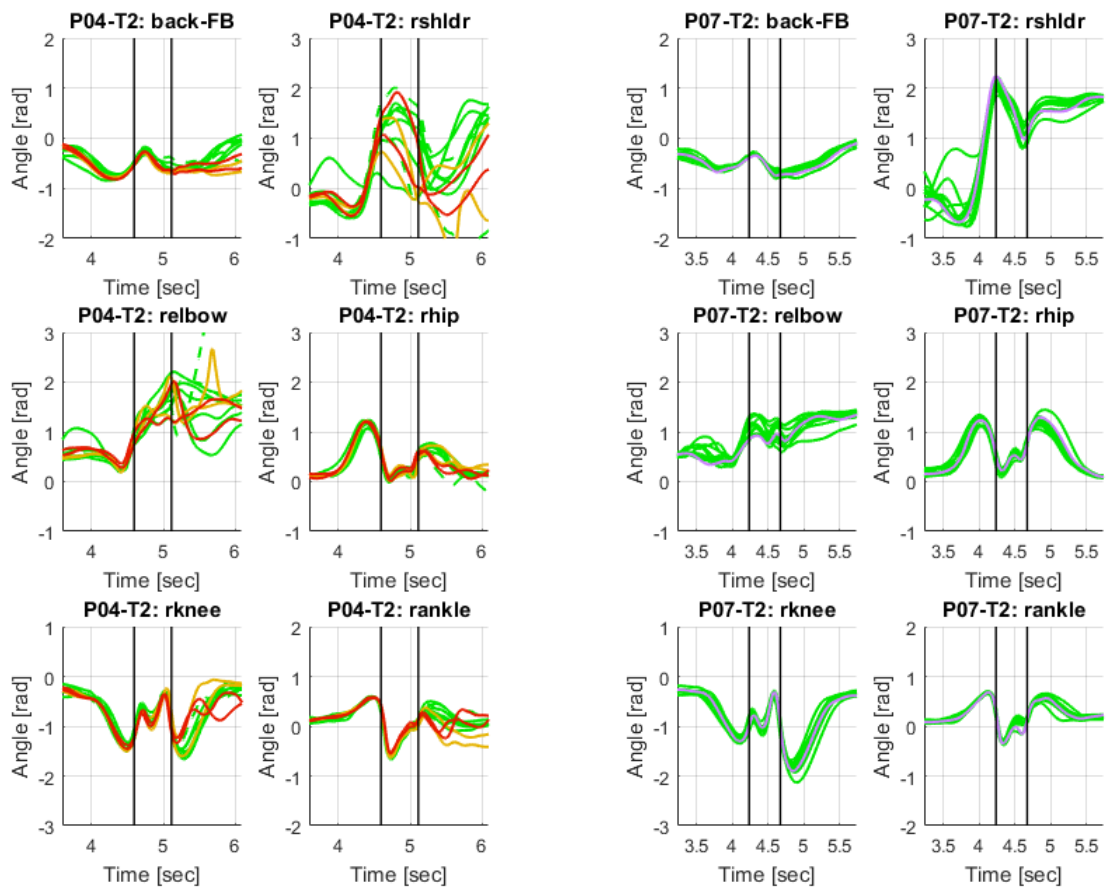
Table (A.5) Number of jumps graded "perfect" in each jumping set performed by each participant during the experiment. Each set had a total of six jumps.

Number	Weight Symbol	Description
1	W_ddq	joint acceleration
2	W_dddq	joint jerk
3	W_ddx	acceleration of toes
4	W_dddX	jerk of toes
5	W_	joint torque
6	W_d	joint torque change
7	W_dd	joint torque effort
<b>8</b>	<b>W_KE</b>	<b>kinetic energy of model</b>
9	W_dq	joint power (joint velocity * force)
10	W_dCoM	CoM velocity magnitude
11	W_ddCoM	CoM acceleration magnitude
12	W_dddCoM	CoM jerk magnitude
<b>13</b>	<b>W_CoM-Z</b>	<b>CoM height</b>
<b>14</b>	<b>W_CoM-dZ</b>	<b>CoM vertical velocity</b>
15	W_CoM-ddZ	CoM vertical acceleration
16	W_CoM-dddZ	CoM vertical jerk
17	W_Toe-Z	toe height
<b>18</b>	<b>W_Toe-dZ</b>	<b>toe vertical velocity</b>
19	W_Toe-ddZ	toe vertical acceleration
20	W_Toe-X	forward distance between toes and target
<b>21</b>	<b>W_Toe-dX</b>	<b>toe forward velocity</b>
22	W_CoMToe-X	forward distance between CoM and toes
<b>23</b>	<b>W_CoMToe-dX</b>	<b>relative forward velocity of CoM to toes</b>
24	W_CoM-X	CoM forward position
25	W_CoM-dX	CoM forward velocity
<b>26</b>	<b>W_ddq-tor</b>	<b>torso: joint acceleration</b>
<b>27</b>	<b>W_dddq-tor</b>	<b>torso: joint jerk</b>
<b>28</b>	<b>W_-tor</b>	<b>torso: joint torque</b>
<b>29</b>	<b>W_dq-tor</b>	<b>torso: joint angular power</b>
<b>30</b>	<b>W_ddq-arm</b>	<b>arms: joint acceleration</b>
<b>31</b>	<b>W_dddq-arm</b>	<b>arms: joint jerk</b>
<b>32</b>	<b>W_-arm</b>	<b>arms: joint torque</b>
<b>33</b>	<b>W_dq-arm</b>	<b>arms: joint angular power</b>
<b>34</b>	<b>W_ddq-leg</b>	<b>legs: joint acceleration</b>
<b>35</b>	<b>W_dddq-leg</b>	<b>legs: joint jerk</b>
<b>36</b>	<b>W_-leg</b>	<b>legs: joint torque</b>
37	W_dq-leg	legs: joint angular power
38	W_L	angular momentum of model
39	W_dL	angular momentum first derivative
40	W_ddL	angular momentum second derivative

Table (A.6) The full set of hypothesized IOC cost terms. Unless otherwise stated, cost terms are summed over all joints in the kinematic model. Bolded terms identify the final set of cost terms used in the IOC analysis

# Appendix B

## Additional Figures





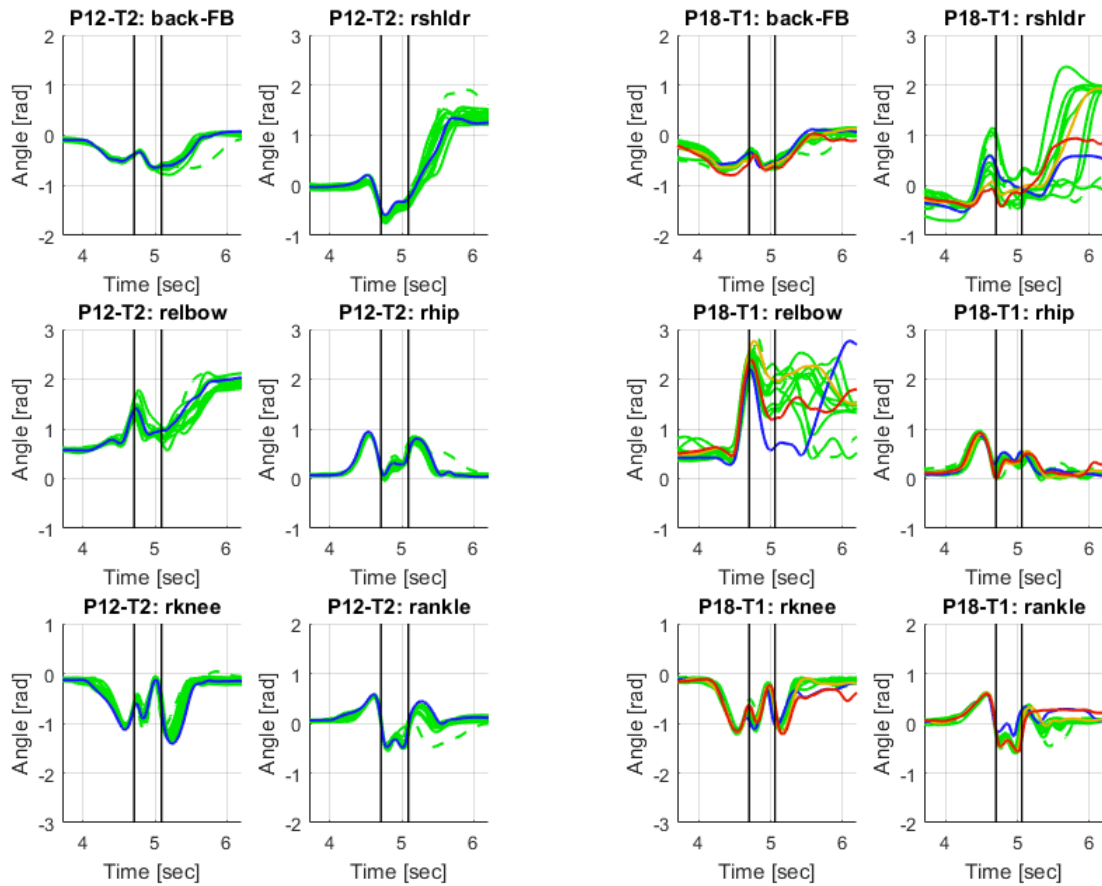


Figure (B.1) Examples of 12 jumps to a target from four participants, showing 6 joint trajectories. Jump grade colour-coding applies.